Mesoscale structural modification for anode-supported solid oxide fuel cell:

Effects of corrugated structures fabricated through microextrusion printing

Haewon Seo

2021

Contents

Acknowledgments

I would like to express my sincere gratitude to a number of people who supported me throughout the research work and my campus life at Kyoto University.

First and foremost, I would like to appreciate my supervisor, Professor Hideo Yoshida, who offered the best research environment to Thermal Engineering Laboratory. Despite his busy schedule, Professor Yoshida not only took his time for my personal matters but also encouraged me to be able to do great campus life in Japan. In addition, I would like to acknowledge and extend my gratitude to Professor Hiroshi Iwai, who suggested this theme to me. Without his continuous advice, enthusiasm, and encouragement, this study would hardly have been conducted. I would like to thank Assistant professor Motohiro Saito for his warm encouragement and assistance. I also owe a great debt of gratitude to Dr. Masashi Kishimoto. I received immense help from Dr. Kishimoto, who provided me with meticulous comments, suggestions, and generous guidance on my academic work, as well as made me adapt well to laboratory life. I would like to show my greatest appreciation to Mr. Masaya Sasaki and Mr. Taishi Nakagawa, former students in Thermal Engineering Laboratory of Kyoto University, who helped me improve the calculation code. I also appreciate other former and current students in our laboratory. Without them, I would not have had an enjoyable life in Kyoto.

I would like to appreciate Professor Koji Takahashi who gave precious guidance and valuable advice at Kyushu University. Moreover, I would like to offer my special thanks to Dr. Janusz S. Szmyd, Dr. Grezegorz Brus, Dr. Katarzyna Berent, and Easy-to-Assemble Stack Type (EAST) members at AGH University of Science and Technology in Poland. Their invaluable advice and suggestions were greatly helpful to develop microextrusion printing. Furthermore, I also express my gratitude to Dr. Ángel Larrea, Dr. Miguel A. Laguna-Bercero, and Dr. Ruth Lahoz at Universidad de Zaragoza, and Dr. Suk Won Cha at Seoul National University for fruitful discussion.

I would like to express my heartfelt thanks to my parents and elder sister for their financial support, constant encouragement, dedication, and understanding during my ten-year study abroad.

Most of all, I would like to offer my heartfelt thanks to the love of my life, Youjin Kim, for her true love and great encouragement.

1

Introduction

1.1 Background

Solid oxide fuel cells (SOFCs) are promising power generation devices for minimizing emissions of carbon dioxide and nitrogen oxides, noise problems, and transmission losses because they can convert the chemical energy of fuels directly into electrical power via electrochemical processes. Since SOFCs are typically operated at high temperatures of around 600–1000 °C, they not only can achieve a high energy conversion efficiency of about 60 % but also do not require any precious metal catalysts such as platinum. Owing to these advantages, SOFCs have been put into practical use as power sources for residential houses in recent years. For SOFC systems to make active inroads into the energy market, however, realizing the low-temperature operation through further improvement in the electrochemical performance of SOFCs is the top priority.

Lowering the operating temperature of SOFCs is one of the major goals to reduce degradation rate, startup and shutdown times, and manufacturing cost (*1–4*). However, it inevitably causes a marked drop in the electrochemical performance of SOFCs because cell resistance increases with decreasing operating temperature. Recently, owing to the development of anode-supported SOFCs designed with a thin electrolyte film of about 10 μm thickness, the ohmic resistance attributed to an electrolyte is greatly reduced. Nevertheless, it is still required to reduce the activation resistance associated with the electrochemical reaction inside the electrodes of SOFCs to compensate for the drawbacks of the low-temperature operation.

For a desirable cell performance even at low operating temperatures, it is necessary to increase the volumetric density of reaction sites, which mainly contribute to the electrochemical reaction. However, it has been confirmed that the electrochemical reaction mainly occurs not at all reaction sites but at those distributed in an electrochemically active region within about 20 μm from the electrode–electrolyte interface (*5–12*). From this viewpoint, various approaches to increasing the density of reaction sites near the electrode–electrolyte interface in a wide range of length scales have been reported. For instance, attaching a functional layer between an electrode and an electrolyte is a common approach to improving cell performance (*7*, *13–16*). Generally, the functional layer composed of fine metal and ceramic particles in the range of 0.1–1 μm has a higher density of reaction sites than a support layer so that it offers a higher electrocatalytic activity of an electrode. The introduction of metal or ceramic nanoparticles (no more than 0.1 μm) into an as-prepared porous structure by wet infiltration (*17–26*) is another approach to increasing the density of the reaction sites, particularly triple-phase boundaries (TPBs). Typically, the wet infiltration technique entails the introduction and thermal decomposition of a metal or ceramic precursor solution in the porous structure. The most remarkable feature of this technique is that the sintering processes for metal and ceramic particles are independently carried out, particularly in the preparation of a composite cathode. That is, particles for infiltration can be prepared at a lower sintering temperature so that particle agglomeration due to high-temperature sintering can be avoided. This results in an increase in the volumetric density of TPBs in the entire region of an electrode and thereby improvement in the electrocatalytic activity of the electrode.

As an alternative approach to increasing the density of reaction sites, extending the electrode–electrolyte interfacial area by fabricating a mesostructure in the range of 10–100 μm at the interface is attracting widespread attention. For example, Konno et al. (*27*) machined mesoscale grooved structures on a flat electrolyte made of yttria-stabilized zirconia (YSZ), which was followed by sintering a NiO–YSZ anode to prepare a cell having a corrugated interface structure. By evaluating the electrochemical performance of the cell, they clarified that the cell had a higher performance than a flat cell. Specifically,

the current density of the cell where the interfacial area was increased by 60 % compared with that of the flat cell was 25 % higher than that of the flat cell at the terminal voltage of 0.5 V at 800 °C with pure hydrogen. Similarly, it has also been reported that mesoscale grooves on an electrolyte substrate can be patterned by using other processes, *e.g.*, micropowder imprinting (*28–30*) and laser machining (*31–38*). For instance, Xu et al. (*28*, *29*) reported that line-and-space patterns in the range of 10–100 μm on a thin YSZ sheet were successfully fabricated by employing a micropowder imprinting process, which uses a fine-patterned mold to fill a YSZ precursor binder followed by hot pressing. They found that the maximum power density of a mesoscale-modified cell where a 30 % increase in the anode–electrolyte interfacial area was achieved exhibited three times higher than that of a flat cell under the operating condition of 800 °C with 3 % humidified hydrogen (*29*). Cebollero et al. (*34*, *38*) achieved periodic cone-shaped patterns with diameters of about 20–30 μm and 7 μm depth on a YSZ electrolyte surface by applying a laser beam machining process. Through electrochemical impedance spectroscopy (EIS), they confirmed that the cathode activation resistance in a mesoscale-modified cell with an increase in the cathode–electrolyte interfacial area of 30 % was reduced by 25–50 % compared with that in a flat cell at 750–900 °C (*38*). That is, both of these approaches resulted in the enhanced electrochemical performance of the cells because of the increased electrode–electrolyte interfacial area (*29*, *31*, *33–38*). Nevertheless, although the micropowder imprinting process is considered suitable for processing complicated micro- to mesoscale shapes, it was pointed out that the thin electrolyte sheet tended break when the mold was separated from it (*28*). Moreover, although the laser beam machining process can precisely pattern the substrate with relatively high accuracy, some cracks in the cell often formed during the process under high laser power conditions (*32*, *35*). Therefore, it is difficult to control the grooved structures precisely and to prevent breakage and cracks during such mechanical processing of electrolyte surfaces. Thus, it is necessary to find alternative fabrication methods for increasing the interfacial area between the electrode and the electrolyte to overcome these critical problems.

On the other hand, a positive influence on improving cell performance was demonstrated but there

is no consistency in the relationships between the interfacial area enlargement factor and the relative decrease in cell resistance among the existing experimental results. This is essentially due to the fact that the electrochemical performance of SOFCs is affected by multiple factors such as the cell structure, operating condition, and material for the cell components. Hence, it is highly expected that a numerical simulation in which those factors are appropriately considered gives important clues to the understanding of the effect of the mesostructural modification. Thus far, various numerical models have been developed to investigate the effect of the mesostructural modification for SOFCs on cell performance (*27*, *36*, *39*–*45*). For instance, Konno et al. (*27*, *40*) found by analyzing the distributions of physicochemical quantities within mesoscale-modified SOFCs during power generation that introducing mesoscale grooved structures on the electrode–electrolyte interface reduces both ohmic and activation overpotentials. Also, they clarified that its effect became more prominent with increasing the electrode–electrolyte interfacial area, particularly in a cell having a thin electrolyte such as anode-supported SOFCs. Iwai et al. (*39*), Bertei et al. (*41*), Chesnaud et al. (*36*), Chueh et al. (*43*), and He et al. (*45*) manifested that the geometrical shape of the electrode–electrolyte interface is one of the key factors that can maximize the improvement in cell performance. Moreover, He et al. (*42*) found that the attachment of gadolinium-doped ceria (GDC) pillars on the cathode–electrolyte interface was more effective in lanthanum strontium cobalt ferrite (LSCF) and LSCF–GDC cathodes with a relatively small particle size (a few tens of nanometers). This suggests that the electrode microstructure is also an important factor that determines the improvement in cell performance due to the mesostructural modification of the electrode–electrolyte interface (*40*, *42*, *44*). Despite these key findings, a detailed mechanism whereby the mesostructural modification improves cell performance has not yet been clarified. In addition, a lack of comprehension regarding the improvement in cell performance by the mesostructural modification in quantitative terms still remains (*27*, *36*). For example, according to the literature (*36*), the current density at 0.7 V at 800 °C increased from 0.13 to 0.30 A cm^{-2} in the measurement, whereas from 0.96 to 1.6 A cm^{-2} in the simulation. Deservedly, these quantitative discrepancies between the electrochemical characteristics of each cell obtained from the

experiment and simulation led to a mismatch of the increases in cell performance of a mesoscale-modified cell relative to a flat cell. This is because the structures of the cells they used in the electrochemical testing were not properly considered in the numerical model they developed. Therefore, a numerical model with high validity has to be constructed to clarify the aforementioned unclear issues.

In addition to numerical analysis, another powerful tool for evaluating the electrochemical performance of SOFCs is EIS widely used in analyzing the resistance of electrochemical devices. In the EIS measurement, when a small amplitude of an alternating current (AC) current signal with multi frequencies is imposed on a cell, an AC potential response is obtained. Since several resistance components in SOFCs emerge as the form of an integrated curve, EIS data are typically analyzed by fitting to an equivalent circuit model using the complex nonlinear least-squares (CNLS) method. However, it is difficult to clearly separate the resistance components from EIS data when some of their time constants have the same order of magnitude. In this case, the distribution of relaxation time (DRT) method, which can separate each resistance component with high resolution (*46–55*), is very useful. Although the DRT method is based on only pure mathematics, it offers very accurate fitting results when EIS data obtained under a set of operating conditions are given. Moreover, this method does not require specific information on tested cells (*e.g.*, the properties of materials and cell structures) so that it has relatively high degrees of freedom in analyzing EIS data. Thus, the DRT method will provide a great opportunity to quantitatively analyze the effect of the mesostructural modification for SOFC, particularly under operating conditions where such databases have not yet been built.

1.2 Aims and outline of dissertation

The main objective of this dissertation is summarized into two parts as follows. One is to find an alternative fabrication method for increasing the electrode–electrolyte interfacial area in SOFCs and then verify its applicability. The other is to quantitatively elucidate a detailed mechanism whereby the mesostructural modification improves the electrochemical performance of SOFCs through experiment and numerical analysis. In this work, anode-supported SOFCs are used unlike electrolyte-supported SOFCs used in the previous works (*27*, *29*, *31–35*, *38*, *39*) since the increase in the interfacial area is most effective when the electrolyte is thinner (*27*, *40*).

In Chapter 2, the applicability of microextrusion printing is verified and the effect of the mesostructural modification of the electrode–electrolyte interface in anode-supported SOFCs on improving cell performance is confirmed through electrochemical testing. The goal of this chapter is to predict the line width of an extruded paste from a micronozzle by developing a mathematical model and to demonstrate improvement in the electrochemical performance of anode-supported SOFCs by the mesostructural modification of the electrode–electrolyte interface.

Chapter 3 discusses the mechanism of improvement in cell performance by the mesostructural modification during power generation through numerical simulation. By using a two-dimensional (2D) numerical model where the structures of tested cells are implemented, distributions of the physicochemical quantities that contribute to the electrochemical reactions are quantitatively analyzed.

Chapter 4 analyzes the effect of the mesostructural modification on cell performance through EIS. The goal of this chapter is to clarify which resistance component mainly causes its effect to fade away under a low hydrogen partial pressure condition using the DRT method.

Chapter 5 summarizes the major findings covered in this dissertation and offers directions for the future.

2

Microextrusion printing for increasing electrode–electrolyte interface in anode-supported SOFCs

2.1 Introduction

To create mesoscale structures in SOFCs without structural failures, additive manufacturing processes including inkjet printing (*15*, *56*, *57*), stereolithography (*58*, *59*), and microextrusion printing (also called direct writing) (*60–63*) are considered as candidates. Among these candidates, it is important to find the most desirable additive manufacturing process which has a sufficiently high printing resolution of a printing technique, and high shape retainability and hardenability of printing material. Young et al. (*15*) demonstrated the applicability of inkjet printing for the fabrication of NiO–YSZ anode functional layers and YSZ electrolyte layers with thicknesses of about 6–18 and 6–12 μm, respectively, by multilayer printing. However, since inks for use in inkjet printing have relatively low viscosity (below 20 mPa s) and surface tension (28–350 mN m^{-1}) (*64*), it is difficult to keep its shape after being printed. Hernández-Rodríguez et al. (*59*) used stereolithography to fabricate a self-supported YSZ electrolyte with a thickness of about 100 μm by multilayer printing. However, suspensions used in stereolithography need not only to be cured by photochemical treatment but also to be eventually sintered by thermal treatment to obtain a stiff layer. In microextrusion printing, a highly viscoelastic paste composed of metal and/or ceramic powders is extruded through a micronozzle onto an object, whose relative position is precisely controlled. This technique allows the construction

of three-dimensional (3D) structures in the range from about 1 to 250 μm (*65*, *66*) since it enables production with high speed, positional accuracy, and good reproducibility because of robotic control (*66*). Also, pastes can easily retain its shape after printing because of its relatively high viscosity (1–10^5 Pa s (*67*)). Moreover, extruded pastes can form a stiff layer by only thermal treatment, so that the hardening process is relatively simple. Therefore, microextrusion printing can be an alternative fabrication method for increasing the electrode–electrolyte interface.

The feasibility of microextrusion printing for fabricating SOFCs having complex structures and patterns has been demonstrated. For instance, Kim et al. (*61*) produced a planar SOFC cell consisting of two serially integrated cells by extruding paste materials of all cell components through a micronozzle of 210 μm diameter. They achieved a cell having line-shaped electrodes and an electrolyte whose width and thickness were over 500 μm and up to 30 μm, respectively. Also, Khun et al. (*62*, *63*) used microextrusion printing to manufacture single-chamber SOFCs having patterned electrodes on electrolyte plates. However, the aforementioned studies only focused on the fabrication of SOFC electrodes and electrolytes using microextrusion printing.

In this chapter, the applicability of microextrusion printing as an alternative fabrication method for increasing the electrode–electrolyte interfacial area is verified and then the effect of its increase on the electrochemical performance of anode-supported SOFCs is investigated. First, a homogeneous NiO–YSZ anode paste is prepared as an extrusion material, and its rheological properties are evaluated. Then, printing resolution defined as line width in this study is evaluated to determine printing parameters for cell fabrication, by comparing with a developed mathematical model. By varying one of the parameters for the microextrusion printing process, two types of anode-supported SOFCs having different interfacial area enlargement ratios are prepared by extruding the anode paste onto anode disks. The cross-sectional structure of the cells is observed by scanning electron microscopy (SEM) and their electrochemical performance is evaluated. Finally, the effect of increasing the interfacial area on the cell performance under several operating temperatures and hydrogen partial pressures is discussed.

2.2 Experimental

2.2.1 Preparation of anode paste

The anode paste material used in this study was a mixture of NiO and YSZ powders. 66 wt% NiO powder (FUJIFILM Wako Pure Chemical Corp., Japan, average particle size = *ca*. 1–2 μm) and 34 wt% $(Y_2O_3)_{0.08}(ZrO_2)_{0.92}$ powder (TZ-8Y, Tosoh Corp., Japan, crystallite size = 22 nm) were mixed; then an appropriate amount of isopropanol was added to the mixed powder with zirconia balls (ϕ 4.0 mm), then the mixture was ball-milled at 450 rpm for 1 h to disperse the particles. After that, the isopropanol was evaporated using a drier. The resultant powder, whose average particle size is *ca*. 0.46 μm (observed by SEM), was sieved with a 53 μm mesh to remove agglomeration. Thereafter, a 25 wt% terpineol-based binder (VEH, Nexceris, LLC, USA) was added, which was followed by stirring at 2000 rpm for 30 min to form a uniform anode paste.

2.2.2 Rheological characterization

To understand the rheological behavior of the prepared anode paste during the microextrusion printing process, the rheological properties of the anode paste were characterized using a rotational double coaxial cylinder viscometer (Viscolead ADV, Fungilab, S.A., Spain) schematically shown in **Fig. 2.1**. To eliminate the dissolved gas inside the paste, the paste was deaired under a pressure of 0.01–0.02 MPa during magnetic stirring in a vacuum desiccator. Thereafter, the paste was filled into a gap between the inner and outer cylinders of the viscometer. The outer diameter of the inner cylinder and the inner diameter of the outer cylinder were 7.6 and 18.8 mm, respectively. By rotating the inner cylinder, the shear stress and apparent viscosity of the paste were calculated from the measurement of the torque transferred between the cylinders via the paste. The measurement was conducted under various rotational speeds of the inner cylinder in the range from 0.3 to 100 rpm. A thermostatic water bath was used to keep the paste temperature at 27 °C.

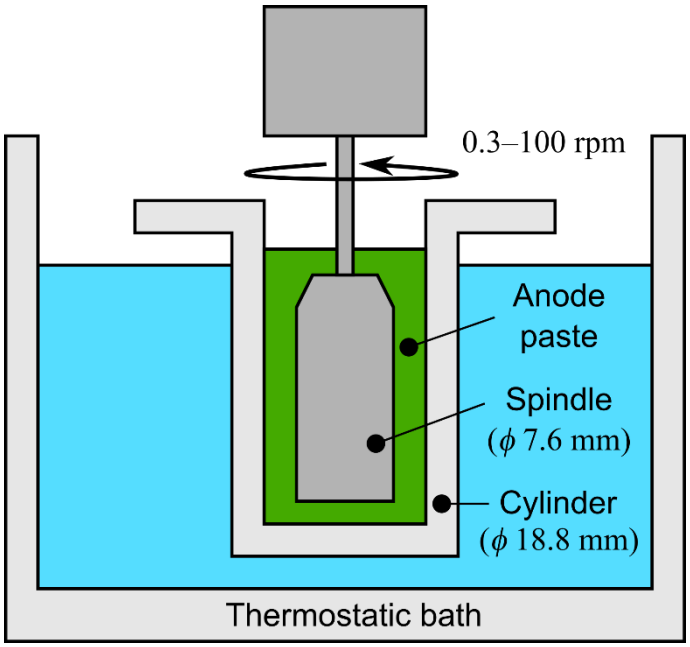

Fig. 2.1 Schematic view of rotational double coaxial cylinder viscometer.

2.2.3 Printing resolution test

As schematically shown in **Fig. 2.2**, when a paste is ejected from a micronozzle with applied volumetric flow rate Q from the vertical direction z, and at the same time an object moves in the horizontal direction y with speed v, the paste extruded from the nozzle is printed onto the object and forms a line.

The anode paste was placed into a gas-tight syringe and pushed with a piston until a small amount of paste was extruded from the syringe to remove the remaining air. The syringe was fixed vertically to a syringe pump (Pump 11 Elite Nanomite, Harvard Bioscience, Inc., USA) before a nozzle tip (nozzle length= 6.35 mm, Nordson Corp., USA) with an inner diameter of 150 μm was attached to the end of the syringe. A 50 mm × 50 mm flat substrate made of alumina was fixed on a precision stage. The distance between the nozzle tip and the alumina substrate was adjusted to about 100 μm using a z-axis stage. The extrusion process was observed from the side using an optical microscope. After printing, the line width of the printed anode was measured using a 3D measurement system (VR-3100, Keyence Corp., Japan).

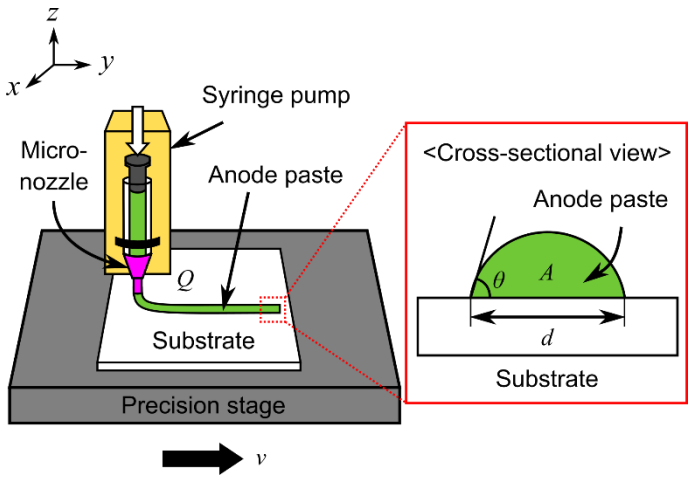

Fig. 2.2 Schematic view of microextrusion printing process.

When the paste is extruded from the nozzle, the cross-sectional area of the extruded paste S_0 can be calculated as

$$S_0 = \pi \left(\frac{D_0}{2}\right)^2, \tag{2.1}$$

where D_0 represents the inner diameter of the nozzle tip. Since every material has a different wettability, however, the contact angle between the paste and the substrate has to be taken into consideration to estimate the line width of the printed paste. Therefore, the cross-sectional area of the printed paste A can be expressed as a function of the line width (resolution) of the printed paste d and the contact angle θ in radians as

$$A = \left(\frac{d}{2\sin\theta}\right)^2 \left(\theta - \frac{1}{2}\sin 2\theta\right). \tag{2.2}$$

Thus, the volumetric flow rate of the printed paste on the substrate is equal to the product of A and v, as expressed in the following equation:

$$Q = Av = \left(\frac{d}{2\sin\theta}\right)^2 \left(\theta - \frac{1}{2}\sin 2\theta\right) v. \tag{2.3}$$

Then, d can be estimated as

$$d = \sqrt{\frac{8\sin^2\theta}{2\theta - \sin 2\theta} \frac{Q}{v}}. \tag{2.4}$$

A small droplet of the anode paste of pL order was observed from the side using an optical microscope to evaluate the contact angle. The width and height of the droplet were measured using the open-source image processing program "ImageJ" (*68*), and the value of θ was analyzed using the half-angle method, which assumes that a sessile drop is part of an ideal sphere.

To investigate the line width of the anode paste, a printing experiment was conducted under a total of 16 conditions, four different stage speeds and four different flow rates, using the precision stage and the syringe pump, as shown in **Table 2.1**.

Table 2.1 Printing parameters for resolution study.

Nozzle size / μm	Applied flow rate, Q / μL min^{-1}	Speed of stage, v / mm s^{-1}
150	9.49 / 14.2 / 19.0 / 23.7	5.0 / 10 / 15 / 20

2.2.4 Cell fabrication

Three types of anode-supported SOFCs having different interfacial area enlargement ratios were prepared including a flat cell (Cell REF) as a reference. Note that the flat cell was prepared to compare a relative increase in the electrochemical performance of the cells. First, NiO–YSZ mixed powder at a ratio of NiO:YSZ = 66:34 (wt%) was prepared by planetary ball milling for 1 h, with the addition of 10 wt% carbon black (Asahi#15, Asahi Carbon Co., Ltd., Japan) as a pore former. 2.0 g of the mixed powder was weighed and then uniaxially hand-pressed at a pressure of 60 MPa for 1 min to form a

pellet with a diameter of 30 mm. Thereafter, the pellet was presintered at 1250 °C for 2 h with heating and cooling rates of 200 °C h^{-1}.

By microextrusion printing, the prepared anode paste was printed on the anode disks in a region of 16 mm × 16 mm. The anode patterning was conducted at a stage speed of 10 mm s^{-1} and an applied flow rate of 9.49 μL min^{-1}. To clarify the effect of the increase in the electrode–electrolyte interfacial area on the electrochemical performance of the cells, the paste was printed to cover 40 and 80 % of the target region, and the printed samples were named Cell 40 and Cell 80, respectively. After printing, the line width of the printed anode on the anode disk was measured using the 3D measurement system. Then, the printed anodes were sintered at 1250 °C for 2 h at heating and cooling rates of 200 °C h^{-1}.

To avoid a difference in the microstructure in the effective reaction area owing to the difference in the starting material of the anode disk and the printed anode, a fine-grade NiO (Sumitomo Metal Mining Co., Ltd., Japan, median diameter = 0.4 μm)–YSZ anode functional layer (AFL) was spin-coated on the anode disks after the anode patterning. An AFL suspension made of 10.0 wt% NiO–YSZ mixed powder (NiO:YSZ = 66:34 wt%), 0.80 wt% polyvinyl butyral (PVB, Sigma-Aldrich Co., LLC, USA), and 89.2 wt% ethanol was prepared for the spin coating. The AFL suspension was ball-milled at 1000 rpm for 10 min with zirconia balls (ϕ 1.0 mm), which was followed by ultrasonication for 5 min to form a well-dispersed suspension. After that, it was added dropwise onto the anode disk and immediately spun at 1000 rpm for 30 s to form the AFL. After 10 cycles of spin coating, the coated samples were sintered at 1250 °C for 2 h at heating and cooling rates of 200 °C h^{-1}.

To form a dense electrolyte, a YSZ suspension was deposited on the anode disk by spin coating. The suspension was composed of 10.0 wt% YSZ powder, 0.80 wt% PVB, and 89.2 wt% ethanol. It was prepared by the same method as the AFL suspension, and then added dropwise onto the AFL and immediately spun at 3000 rpm for 30 s to form a thin YSZ layer. After 20 cycles of spin coating, the coated samples were sintered at 1400 °C for 5 h. The heating and cooling processes were conducted at 120 and 200 °C h^{-1}, respectively.

To prevent the formation of insulating phases such as $La_2Zr_2O_7$ and $SrZrO_3$ by the reaction of the

lanthanum strontium cobalt ferrite (LSCF) cathode and YSZ electrolyte, a gadolinium-doped ceria (GDC) barrier layer was coated on the YSZ electrolyte by spin coating. A GDC suspension consisted of 10.0 wt% $Gd_{0.1}Ce_{0.9}O_{1.95}$ powder (GDC-10(AU), Shin-Etsu Astech Co., Ltd., Japan), 0.80 wt% PVB, and 89.2 wt% ethanol was prepared then added dropwise onto the YSZ electrolyte, which was followed by spinning at 1000 rpm for 30 s. After 10 cycles of spin coating, the coated samples were sintered at 1350 °C for 10 h at heating and cooling rates of 200 °C h^{-1}.

An LSCF–GDC cathode paste composed of 75 wt% $La_{0.6}Sr_{0.4}Co_{0.2}Fe_{0.8}O_{3-\delta}$ (LSCF-6428-N, Kceracell Co., Ltd., Korea)–GDC mixed powder (LSCF:GDC = 50:50 wt%) and 25 wt% terpineol-based binder was screen-printed on the GDC thin film with a mask of 60 μm thickness, which was followed by sintering at 950 °C for 5 h. The heating and cooling processes were conducted at 200 °C h^{-1}. The apparent geometrical cathode area was about 0.785 cm^2.

2.2.5 Performance evaluation and structure observation

The electrochemical characterization of the anode-supported SOFCs was conducted using a commercial fuel cell evaluation system (Micro MRB, USA), as schematically shown in **Fig. 2.3**. The cell was sandwiched by alumina tubes with sealing glass rings attached on both sides of the cell, and then heated to 800 °C. A platinum mesh was used for current collection for both electrodes. Prior to the measurement, NiO in the anode was reduced to Ni by supplying a mixture of nitrogen and hydrogen gases with a total flow rate of 100 sccm, where the proportion of hydrogen gas was gradually increased from 0 to 100 % over 1 h. Then the cell was kept in pure hydrogen for 3 h.

After the reduction process, the electrochemical measurement was conducted at operating temperatures of 600 and 700 °C while feeding 20 % humidified hydrogen gas (20 %, 80 %) with balance nitrogen gas and dry air (N_2:O_2 = 79 %:21 %) to the anode and cathode, respectively, whose total flow rate was 100 sccm on both sides. The current–voltage (*i–V*) and AC impedance characteristics were measured using a Solatron 1455A frequency response analyzer and a Solatron 1470E potentio/galvanostat electrochemical interface (Solartron Analytical, UK). The applied

frequency was in the range from 0.1 MHz to 0.1 Hz with a current amplitude of 10 mA under an operation condition of 0–0.3 A cm^{-2} with an increment of 0.1 A cm^{-2}.

After the electrochemical characterization, the cross section of the tested cells was observed using an SEM (Miniscope TM3000, Hitachi High-Tech Corp., Japan). The cells were cooled in reducing atmosphere and then impregnated with epoxy resin (EpoFix, Struers, Denmark) under 34 Pa for 10 min at room temperature. To observe the cross section of the tested cells with the SEM, the cured samples were cut and polished to expose the cross section of the printed lines.

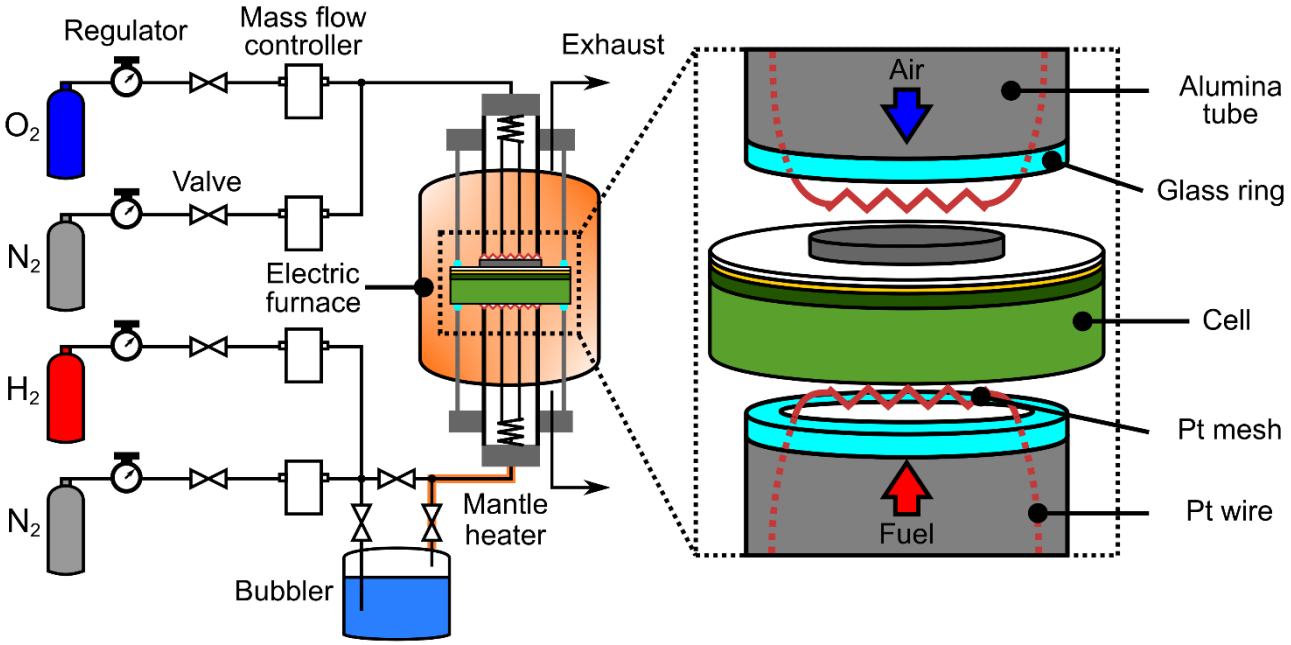

Fig. 2.3 Schematic view of commercial fuel cell evaluation system.

2.3 Results and discussion

2.3.1 Rheological properties

Figure 2.4 shows the shear stress and apparent viscosity curves of the anode paste as a function of the shear rate. A solid line in **Fig. 2.4** represents the fitted result of the measured data (scatter plot) to the Herschel–Bulkley fluid model (*69*), a generalized model of non-Newtonian fluid, which combines yield stress and shear-thinning or shear-thickening behavior in a fluid, described as

$$\tau = \tau_0 + K\left(-\frac{\partial u}{\partial r}\right)^n, \tag{2.5}$$

where τ is the shear stress, τ_0 is the yield stress correlated to the viscoelasticity of the fluid, K is the consistency, u is the velocity distribution of the fluid, r is the pipe radius, and n is the flow index. The rheological parameters obtained by fitting to the Herschel–Bulkley fluid model are shown in **Table 2.2**. As can be seen in this graph, the shear stress increases, and the apparent viscosity decreases as the shear rate increases. Also, the shear stress curve possesses the yield stress obtained as the vertical intercept. These results indicate that the anode paste is a yield pseudoplastic fluid. Thereby, this rheological behavior allows the paste viscosity to be relatively lower when the paste is being extruded.

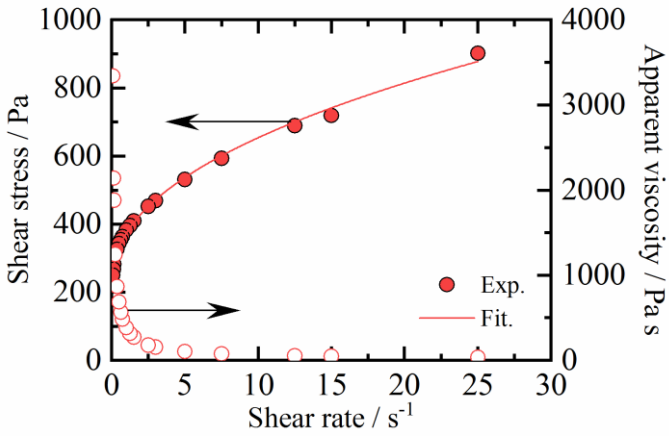

Fig. 2.4 Shear stress and apparent viscosity curves of anode paste as a function of shear rate.

Table 2.2 Fitted values of the paste rheological properties in the Herschel−Bulkley fluid model.

Yield stress, τ_0 / Pa	Consistency, K / Pa s^n	Flow index, n / -	R^2
224.11	150.05	0.46	0.995

2.3.2 Printing resolution test

Figure 2.5 shows a droplet of the anode paste on an alumina substrate and the results of the printing resolution test. As shown in **Fig. 2.5(a)**, it is confirmed that the contact angle between the paste and the solid surface is about 68.6° at room temperature. **Figure 2.5(b)** shows images of the line shape of the paste printed on the alumina substrate at various applied flow rates of the paste and speeds of the stage. Note that all extrusion processes were carried out without direct contact of the nozzle with the substrate. It is confirmed that the anode paste is printed continuously on the alumina substrate under each printing condition except for the condition of Q = 9.49 μL min^{-1}, v = 20 mm s^{-1}. Also, it is clearly seen that the higher the stage speed or the smaller the applied flow rate, the smaller the width of the printed paste. When Q = 9.49 μL min^{-1} and v = 20 mm s^{-1}, discontinuous strands appear, which indicate that the flow velocity of the extruded paste cannot match the stage speed. The printing resolutions from the experiment and the theoretical prediction using Eq. (2.4) are plotted with solid lines as a function of Q in **Fig. 2.5(c)**. As can be seen from the graph, the measured printed width d tends to increase with increasing Q as well as decreasing v, and they are close to the theoretical values. Note that, when the contact angle between the paste and the substrate is not taken into consideration, *i.e.*, the cross-sectional area is calculated as $\pi D_0^2/4$, the modeled values plotted with the dashed line in **Fig. 2.5(c)** do not agree with the experimental data. Therefore, it is important to consider the wettability of the printed paste to the target to precisely predict the line width.

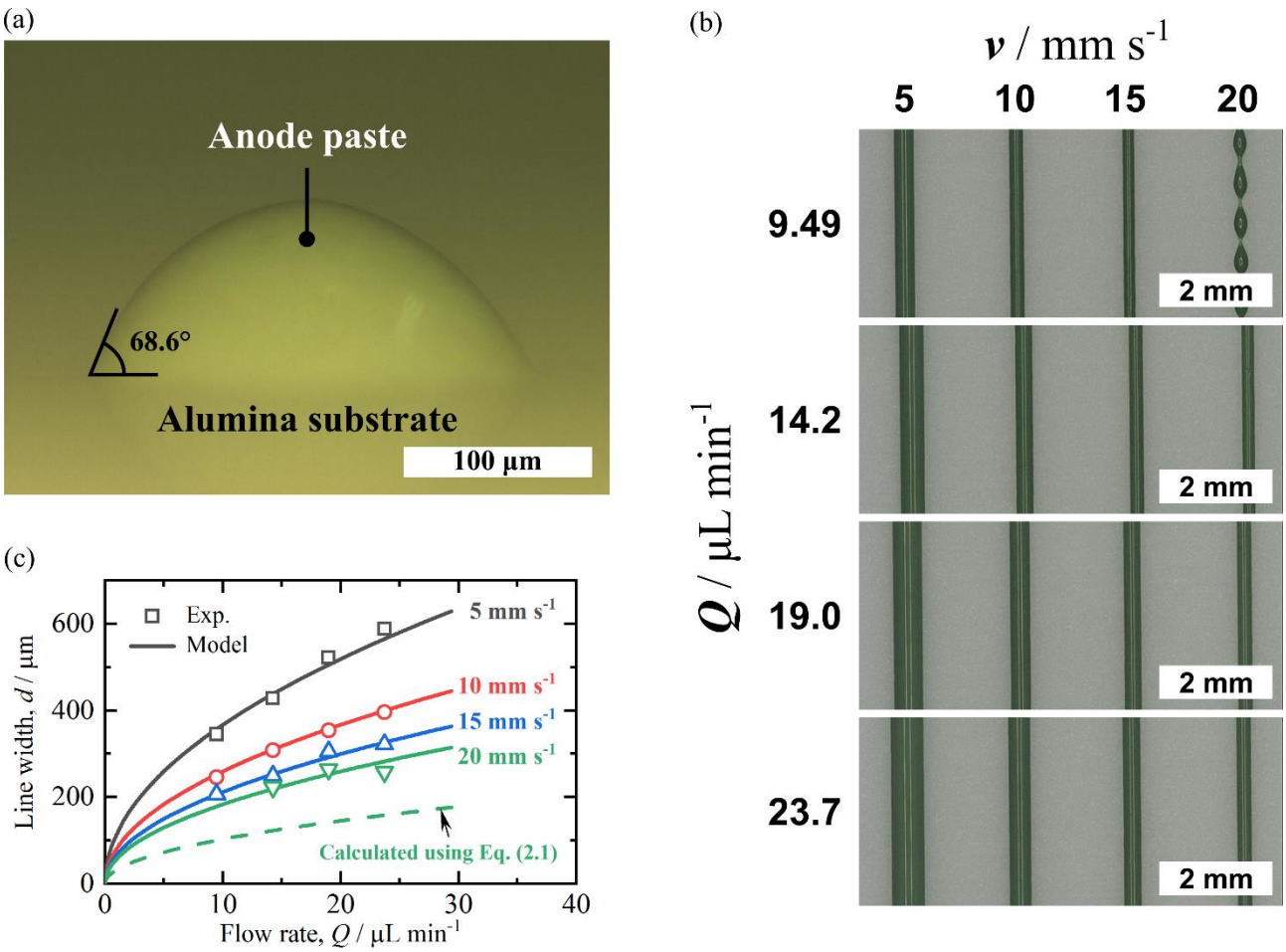

Fig. 2.5 (a) Contact angle of the anode paste on an alumina substrate, (b) images of line shape of the printed paste on the alumina substrate at different applied flow rates and stage speeds, and (c) relationship between the width of the extruded paste and the applied flow rate for experimental (scatter plot) and theoretical data (solid line) at different stage speeds with a contact angle of 68.6º.

2.3.3 Cell structure

The fabrication condition of a stage speed of 10 mm s^{-1} and an applied flow rate of 9.49 µL min^{-1} is selected from the results of the resolution study, and then anode patterning on the anode disk to increase the electrode–electrolyte interfacial area is conducted. The contact angle between the anode paste and the anode disk was measured to be about 87.3° at room temperature (see **Fig. 2.6**). From these values, the print width on the anode disk is predicted to be 206.8 µm. The measured mean widths

of the lines on the anode disk of Cell 40 and Cell 80 are 205.5 and 205.7 μm, respectively, as shown in **Fig. 2.7(a)**, which closely agree with the predicted values.

Figure 2.7(b) shows cross-sectional SEM images of the cells after the electrochemical testing. The average structural geometries of the mesoscale-modified cells are summarized in **Table 2.3**. The average width and average height of each corrugated structure after testing are measured as 202.8 and 38.2 μm in Cell 40, and 204.1 and 38.0 μm in Cell 80, respectively. Note that the width of the anode ridge structures is smaller than that of the as-printed lines because the anode paste, as well as the anode disk, shrinks during the sintering. However, it is considered that their width is increased by attaching the AFL with a thickness of about 15 μm on the surface of the anode disk. Note that a difference in the microstructure between the AFL and the anode disk cannot be distinguished strictly on this scale. The interfacial area enlargement α is calculated from the ratio of the contact area between the electrode and electrolyte of the mesoscale-modified cells to that of the flat cell as

$$\alpha = \frac{(w_{\mathrm{int}} - w) + l_{\mathrm{arc}}}{w_{\mathrm{int}}} = 1 + \frac{l_{\mathrm{arc}} - w}{w_{\mathrm{int}}} , \tag{2.6}$$

where w_{int}, w, and l_{arc} represent the average interval between the printed anodes, average line width, and average arc length of the printed anodes, respectively. From these values, it is found that the interfacial areas are extended by approximately 7.0 % in Cell 40 and 13.5 % in Cell 80. Also, it is observed that dense YSZ films with an average thickness of about 11 μm are formed without any delamination from either electrode. However, a few tiny pores are found in the YSZ thin films in the mesoscale-modified cells, which indicates that the mesostructures on the anode surface may affect the quality of the YSZ films. Moreover, a thin layer of sliver used to further improve the current collection can be seen on top of the cathode surface.

Table 2.3 Average values of the structural geometries of mesoscale-modified cells.

	Average interval, w_{int} / μm	Average line width, w / μm	Average arc length, l_{arc} / μm
Cell 40	456.9	202.8	234.7
Cell 80	229.9	204.1	235.2

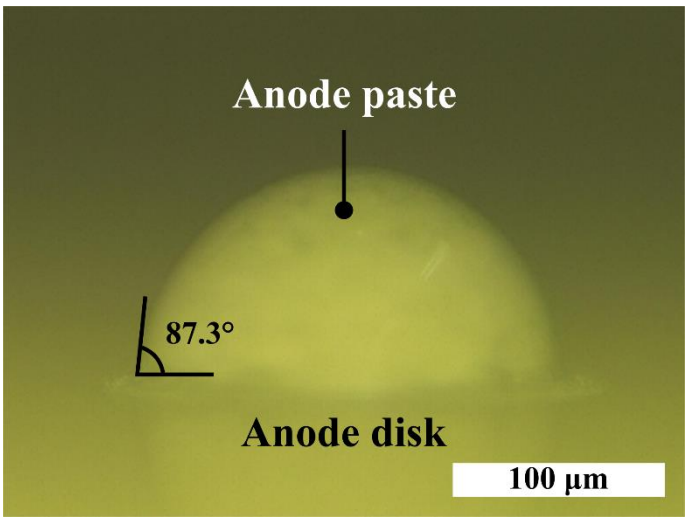

Fig. 2.6 Contact angle of NiO–YSZ anode paste on NiO–YSZ anode disk.

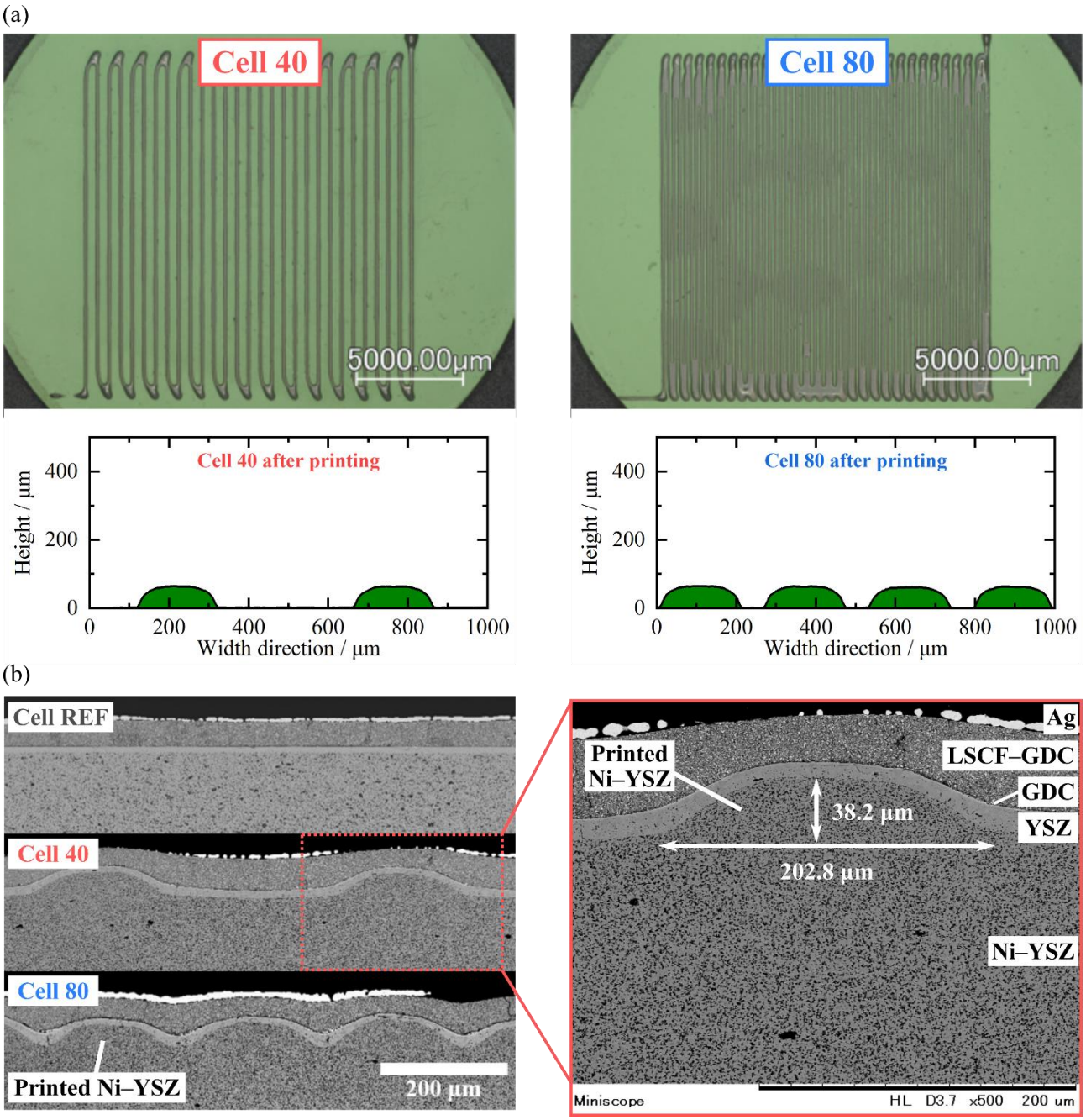

Fig. 2.7 (a) Surface images and profiles of anode disks after printing and (b) cross-sectional SEM images of tested cells.

2.3.4 Cell performance

Figure 2.8 shows the *i–V* and current–power (*i–P*) curves of the tested cells under the operating conditions of 600 and 700 °C with 80 % H_2–20 % H_2O. Note that the current density is defined as the current divided not by the actual electrode–electrolyte interfacial areas but by the apparent geometrical cathode area for each tested cell. This is because the extended interfacial area in the mesoscale-modified cells has complicated effects on the cell performance, some of which are strongly dependent on the size and shape of the mesostructure (*39*, *41*, *45*) and the thickness inhomogeneity. The open-circuit voltage (OCV) values of all cells under all operating conditions considered in this study agree well with the theoretical values obtained with the Nernst equation with a difference of no more than 33 mV as shown in **Table 2.4**; this confirms the existence of a thin but dense YSZ electrolyte, sufficient gas sealing, and fuel humidification. However, the OCV values of the mesoscale-modified cells are slightly lower than those in the flat cell, which indicates a little gas crossover between the electrodes caused by the tiny pores in the YSZ thin films in the mesoscale-modified cells. The *i–V* and *i–P* curves show that the cell performance is improved with increasing electrode–electrolyte interfacial area, regardless of the operating conditions. For instance, when the current density is 0.3 A cm^{-2} under the operating condition of 600 °C, the terminal voltage of Cell REF is 0.49 V, whereas those of Cell 40 and Cell 80 are improved to 0.62 and 0.72 V, respectively. This indicates that the cell overpotential is reduced by increasing the interfacial area between the electrode and electrolyte. This will be discussed in detail on the basis of the impedance data. Moreover, it is clearly seen that the effect of the interfacial area enlargement is greater at lower temperature. For instance, compared with that of Cell REF, the terminal voltage of Cell 80 at the current density of 0.3 A cm^{-2} is 47 and 10 % higher at 600 and 700 °C, respectively.

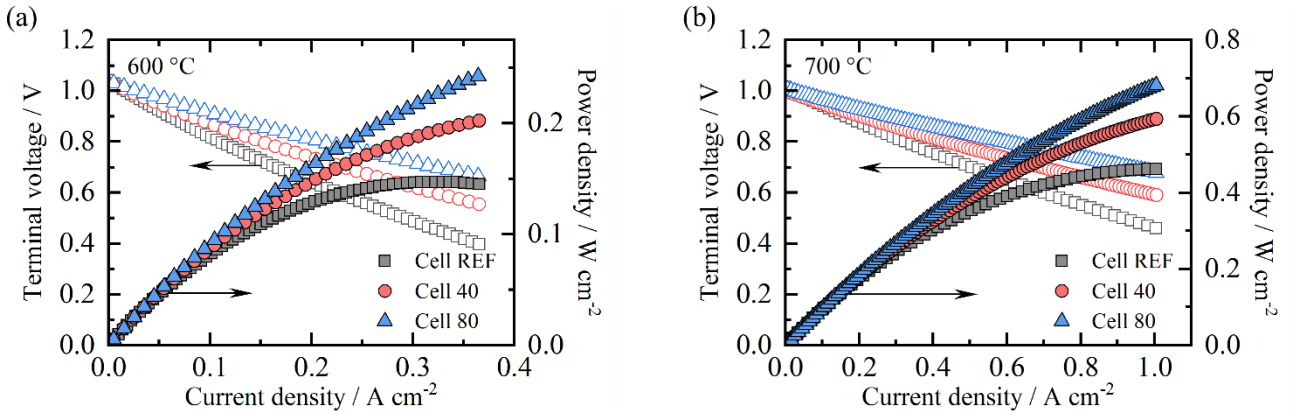

Fig. 2.8 *i–V* and *i–P* curves of cells at (a) 600 °C and (b) 700 °C with 80 % H_2.

Table 2.4 Theoretical and measured OCVs at 600 and 700 °C with 80 % H_2.

Temperature / °C	Theoretical / V	Cell REF / V	Cell 40 / V	Cell 80 / V
600	1.057	1.043	1.024	1.030
700	1.031	1.015	0.997	1.006

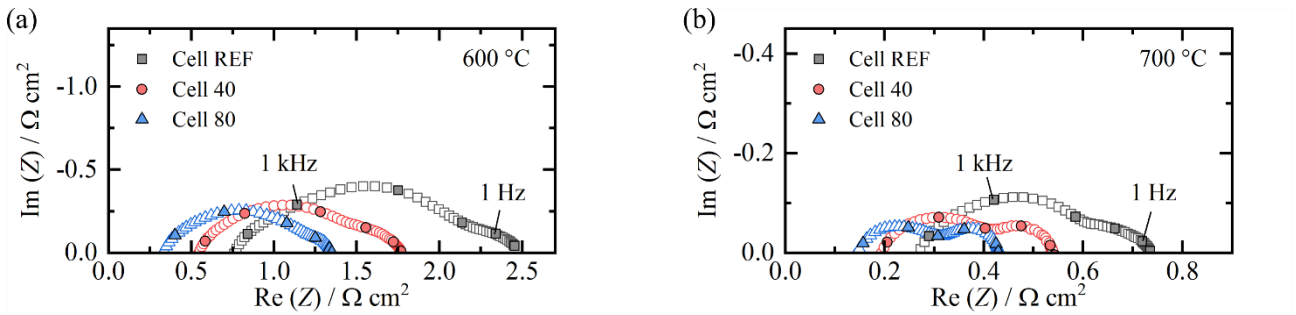

Fig. 2.9 Nyquist plots of EIS of cells at (a) 600 °C and (b) 700 °C with 80 % H_2 under OCV condition.

Figure 2.9 shows Nyquist plots of the electrochemical impedance spectroscopy (EIS) data obtained under the OCV condition at the operating temperatures of 600 and 700 °C with 80 % H_2–20 % H_2O. The EIS data again illustrate that the cell performance is improved with increasing electrode–electrolyte interfacial area at both operating temperatures. For instance, the ohmic resistance R_{ohm}, which is obtained as the high-frequency intercept of the real axis, is 0.76 Ω cm^2 in Cell REF, 0.55 Ω cm^2 in Cell 40, and 0.34 Ω cm^2 in Cell 80 at 600 °C as shown in **Fig. 2.9(a)**. Also, the

polarization resistance R_{pol} can be calculated by subtracting the high-frequency intercept from the low-frequency intercept of the arc. It is measured as 1.2 Ω cm^2 in Cell 40 and 1.0 Ω cm^2 in Cell 80, whereas it is 1.8 Ω cm^2 in Cell REF at 600 °C. Thus, the total resistance (R_{total}) decreases with increasing interfacial area because both R_{ohm} and R_{pol} are reduced; it is measured as 1.8 Ω cm^2 in Cell 40 and 1.4 Ω cm^2 in Cell 80, which are significantly lower than 2.5 Ω cm^2 in Cell REF at 600°C. Moreover, each resistance component at 700 °C also decreases as the interfacial area is increased as shown in **Fig. 2.9(b)**. Specifically, R_{ohm} are 0.27, 0.20, and 0.15 Ω cm^2 and R_{total} are 0.46, 0.34, and 0.29 Ω cm^2 in Cell REF, Cell 40 and Cell 80, respectively; thereby, R_{total} are 0.73, 0.54, and 0.44 Ω cm^2 in Cell REF, Cell 40 and Cell 80, respectively. Furthermore, the relative decreases in R_{total} in each mesoscale-modified cell are almost the same regardless of the operating temperature, *i.e.,* they are 26–28 % in Cell 40 and 42–45 % in Cell 80. From these results, the decreases in R_{total} in the mesoscale-modified cells become larger at the lower temperature, since the cell resistance is relatively larger at 600 °C than at 700 °C. Therefore, it can be concluded that the improvement in the cell performance due to the interfacial area enlargement is more prominent with decreasing operating temperature.

2.3.5 Effect of interface enlargement on cell performance

The effect of the interfacial area enlargement on the cell performance is quantitatively investigated under various operating conditions. For the EIS analysis, an equivalent circuit model with two *RQ* elements (a resistor in parallel with a constant phase element) is introduced, as shown in **Fig. 2.10(a)**, to separate the measured data into three resistance components, which are R_{ohm} and R_{pol} at high and low frequencies (R_1 and R_2). **Figures 2.10(b)** and **2.10(c)** show the area-specific resistances (R_{ohm}, R_1, and R_2) obtained by separating R_{total} for each tested cell as a function of the interfacial area enlargement factor at 600 and 700 °C, respectively. As can be seen in these figures, both R_{ohm} and R_1 for the mesoscale-modified cells decrease with increasing interfacial area under every operating condition, but R_2 is almost the same in all cells. Specifically, R_{ohm} is reduced by 26–28 %

in Cell 40 and 42–45 % in Cell 80, in comparison with that in Cell REF, as mentioned above. Assuming that the current flows uniformly in the thickness direction inside the electrolyte, the local current density in a mesoscale-modified cell whose interfacial area enlargement factor is α is $1/\alpha$ times lower than that in the flat cell. Then, the Joule heating in the flat cell $Q_{\mathrm{ohm,FLAT}}$ and the mesoscale-modified cell $Q_{\mathrm{ohm,MESO}}$ can be estimated as follows.

$$Q_{\mathrm{ohm,FLAT}} = R_{\mathrm{ohm,FLAT}} \times i^2 \times A_{\mathrm{FLAT}} \tag{2.7}$$

$$Q_{\mathrm{ohm,MESO}} = R_{\mathrm{ohm,FLAT}} \times \left(\frac{i}{\alpha}\right)^2 \times \alpha A_{\mathrm{FLAT}} = \frac{Q_{\mathrm{ohm,FLAT}}}{\alpha} \tag{2.8}$$

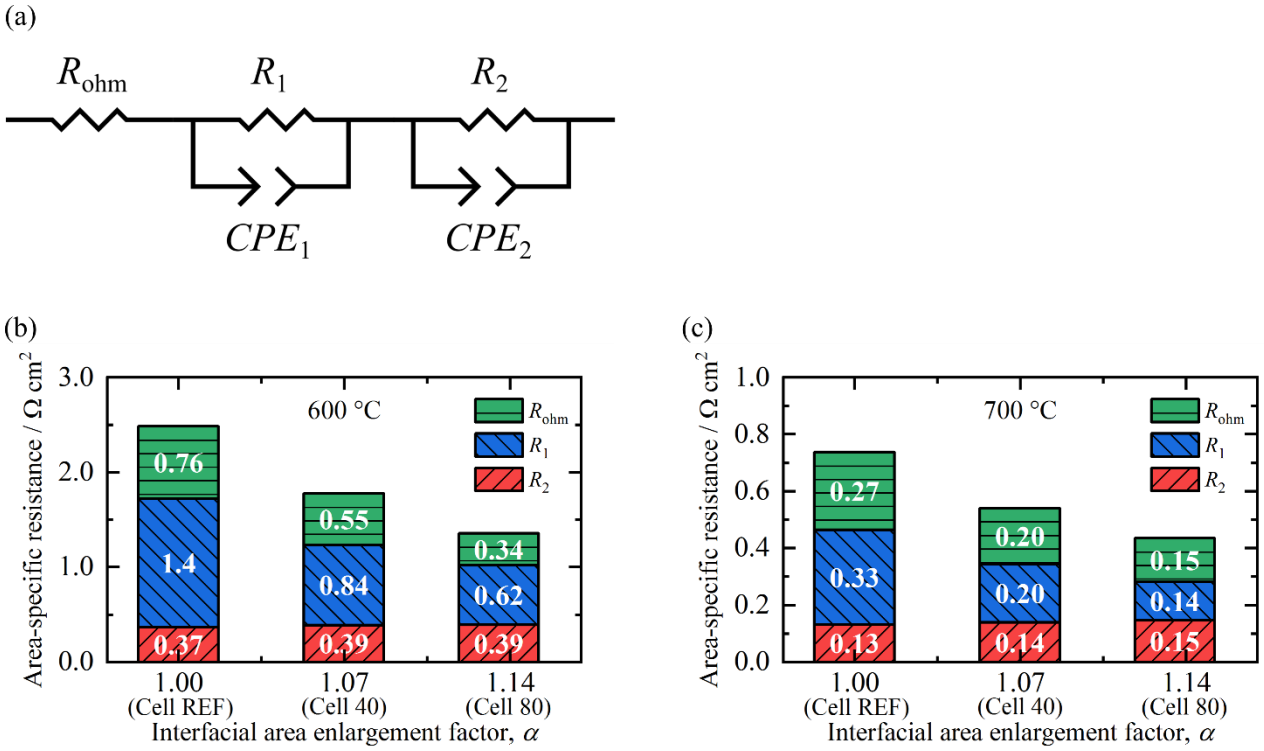

Fig. 2.10 (a) Equivalent circuit model for fitting analysis and area-specific resistances of cells at (b) 600°C and (c) 700°C with 80 % H_2 as a function of interfacial area enlargement factor.

where $R_{\mathrm{ohm,FLAT}}$, i, and A_{FLAT} represent the ohmic resistance, current density, and electrode–electrolyte interfacial area in the flat cell, respectively. Thus, this causes the ohmic loss in the mesoscale-modified cell to be reduced to $1/\alpha$ times that in the flat cell; thus, R_{ohm} for both

mesoscale-modified cells is decreased (*39*, *40*). Note that, however, the predicted relative decreases of R_{ohm} calculated from the interfacial area enlargement factor are 6.5 % in Cell 40 and 12 % in Cell 80, which are lower than the measured values mentioned above. It is considered that these mismatches are caused by the difference between the electrolyte thickness at the top of the corrugated structure (*ca*. 9 μm) and that on the nonpatterned (flat) area (*ca*. 12 μm) (see **Fig. 2.7(b)**). Note that the YSZ suspension flows down along the corrugated structures from the top part during spin coating, since the viscosity of the suspension containing ethanol is relatively low, resulting in an inhomogeneous electrolyte thickness. From the fact that the measured relative decreases of R_{ohm} are much larger than the predicted values, there is a possibility that the ohmic loss is further decreased by the combination of both the mesoscale structures and the inhomogeneous electrolyte thickness effects. To clarify details of this unresolved mechanism, numerical analysis is in progress.

Similarly, R_1 also decreases as the interfacial area is increased, which is reduced by 38 % in Cell 40 and 54–59 % in Cell 80. Thus, it can be presumed that R_1 indicates the activation resistance of both electrodes, because the electrochemical reaction region near the interface between the electrode and electrolyte is extended by increasing the interfacial area (*27*, *34*, *35*, *40*). Additionally, the relative decrease in R_1 for a given enlargement factor is much higher than the experimental results in the literature (*27*, *34*, *35*). This is because the interfacial area between one electrode (the anode or the cathode) and the electrolyte was increased in the previous studies, whereas the interfacial area between both electrodes and the electrolyte is increased in this study. Also, it is considered that the local current density decreases by increasing the interfacial area, and thereby the electrochemical reaction amount per unit reaction site is reduced. Thus, this leads to a further decrease in the activation overpotential because of the nonlinear correlation between the local current density and the activation overpotential.

On the other hand, R_2 in all tested cells are almost the same at every operating temperature. The effect of gas diffusion can be assumed to be similar among the cells, since the anode ridge structures as well as the cathode are negligibly thin compared with the anode disk (in this study, the thickness of the anode including the AFL is *ca.* 800 μm and that of the cathode is *ca*. 50 μm), which indicates that

R_2 is mainly attributed to the gas diffusion in the anode. Note that, both the material selection and the preparation of each component for all the tested cells are carried out identically. Therefore, it is reasonable to conclude that the decrease in R_{total} is largely due to both the decrease in ohmic loss and the extension of the electrochemical reaction region by increasing the electrode–electrolyte interfacial area.

Figure 2.11 illustrates the relative decrease in the total resistance RD, calculated as the difference between the total resistances of Cell REF and the mesoscale-modified cell, $R_{\text{total,FLAT}} - R_{\text{total,MESO}}$, with respect to the total resistance of Cell REF, $R_{\text{total,FLAT}}$, at each current density as follows.

$$RD = 1 - \frac{R_{\text{total,MESO}}}{R_{\text{total,FLAT}}} \tag{2.9}$$

RD in any mesoscale-modified cell are almost constant under 80 % H_2, regardless of the operating temperature and the current density as shown in **Fig. 2.11(a)**. On the other hand, under the 20 % H_2 condition, it is clearly seen that RD in both mesoscale-modified cells decrease as the current density increases as shown in **Fig. 2.11(b)**. It can be presumed that the decrease in RD with decreasing the H_2 partial pressure is mainly caused by the fact that the proportion of the concentration overpotential with respect to the total overpotential increases. That is, the fuel utilization becomes higher with decreasing the H_2 partial pressure, which causes the increase in the concentration overpotential at the anode side. Moreover, the concentration overpotential becomes much larger as the current density increases under lower H_2 partial pressure (*70*). Thus, the effect of the interfacial area enlargement on the cell performance becomes significantly smaller under a low H_2 partial pressure. It can be concluded that the effect of interfacial area enlargement is most prominent when the anode-supported SOFCs having corrugated structures are operated at a low temperature and high H_2 partial pressure.

According to a previous numerical analysis (*40*), the anode-supported SOFCs having an enlargement factor of 1.19 achieved a cell performance improvement of only 19 % compared with the

flat cell. This indicates that the degree of the performance improvement by increasing the interfacial area predicted in the numerical analysis is much lower than that in this work. This is because the electrochemical performance of the cell having a corrugated structure is strongly affected by the anode microstructure (*40*) and the geometrical shape of the corrugated structure (*36*). Therefore, clarifying the effect of the interfacial area enlargement through numerical simulation while taking these factors into consideration, which will be described in the next chapter.

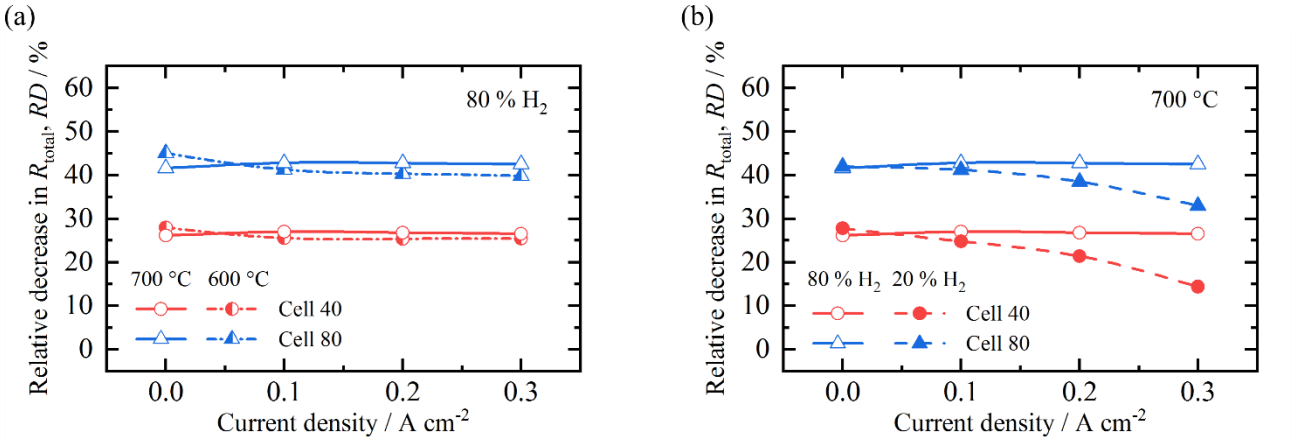

Fig. 2.11 Total decrease in resistance of both mesoscale-modified cells relative to Cell REF (a) at different operating temperatures with 80 % H_2 and (b) with different H_2 partial pressures at 700 °C.

2.4 Summary

For the first time, the additive manufacturing process was used to increase the electrode–electrolyte interfacial area of anode-supported SOFCs to improve the electrochemical performance. To predict the printed width in microextrusion printing, a printing resolution study was conducted experimentally, and the results were compared with the mathematical model. The experimental data agreed well with the mathematical model, particularly when the contact angle between the paste and the substrate was considered. Also, two types of anode-supported SOFCs having different interfacial area enlargement ratios were fabricated by extruding the anode paste onto the flat anode disks and testing them to investigate the correlation between the electrochemical performance and the increase in the interfacial area. It was found that the interfacial areas in Cell 40 and Cell 80 were extended by about 7.0 % and 13.5 %, respectively, compared with that in the flat cell. The electrochemical performance of the cell having corrugated structures was significantly enhanced because of the decrease in both the ohmic resistance and the activation resistance by the interfacial enlargement. It was also found that the cell performance improvement of the mesoscale-modified cells was prominent under the operating condition of 600 °C and 80 % H_2 partial pressure. Therefore, it can be concluded that the cell performance can still be improved by increasing the electrode–electrolyte interfacial area within the same combination of the conventional materials for each cell component.

3

Mechanism of improvement in the electrochemical performance of anode-supported SOFCs by mesostructural modification during power generation

3.1 Introduction

As discussed in Chapter 2, the improvement in the electrochemical performance of anode-supported SOFCs became more prominent with increasing interfacial area but could not be represented by a linear relationship; the same trend can be found in the literature (*34*, *36–40*, *71*). This suggests that the improvement in cell performance cannot be simply predicted with only the interfacial area enlargement factor. Also, it was confirmed that the decreases in the ohmic resistance were further larger than those estimated under the assumption that the current uniformly flows inside a cell. This may be caused by the fact that the physicochemical quantities attributed to the electrochemical reactions are not uniformly distributed within the mesoscale-modified cells because of their structural features: the corrugated electrode–electrolyte interface and inhomogeneous thickness. Since it is challenging to analyze such distributions within SOFCs through experiments, it is highly expected that numerical simulation gives important clues to the understanding of the effect of the mesostructural modification.

Researchers investigated the effect of the mesostructural modification of the electrode–electrolyte interface in SOFCs on the cell performance through numerical analysis in their works (*27, 36, 39–45*),

some of which have experimentally demonstrated it (*27*, *36*, *39*, *44*). For instance, Konno et al. (*27*) developed a numerical model where rectangular grooves with a width and depth were 200 μm were engraved with an interval of 400 μm on a surface of a flat electrolyte with a thickness of 500 μm. Also, they made an electrolyte-supported cell with a similar structure on the macroscopic scales to the numerical model they developed, which was followed by electrochemical testing. They confirmed that the simulation results qualitatively agreed with the experimental ones. However, there was an abysmal lack of quantitative agreement between the electrochemical characteristics of the cells obtained from the simulation and experiment. Specifically, the increase in the current density of a mesoscale-modified cell relative to a flat cell at 0.5 V at 800 °C was measured to be 25 %, whereas was simulated to be 10 %. This mismatch is essentially due to errors in cell performance, which resulted from the fact that the structures of the tested cells were not properly considered in the numerical model they developed. Therefore, to quantitatively discuss the effect of the mesostructural modification in terms of the improvement in cell performance, it is necessary to develop a numerical model with high validity by adequately considering cell structures in a wide range of length scales.

Herein, the mechanism whereby the mesostructural modification improves the electrochemical performance of anode-supported SOFCs is elucidated. After preparing two types of anode-supported SOFC having different electrode–electrolyte interfacial areas, their structural analyses and electrochemical characterization are carried out. Next, a two-dimensional (2D) numerical model where the structures of the tested cells are implemented is developed and then its validity is verified by comparing the simulation results with the experimental ones. Subsequently, changes in the overpotential components of the mesoscale-modified cell relative to the flat cell are quantitatively evaluated. Through analyzing distributions of physicochemical quantities that contribute to the electrochemical reactions inside the cells, the mechanism of the improvement in cell performance by the mesostructural modification is discussed on the basis of the energy losses attributed to such quantities. Finally, the effect of the mesostructural modification under various current density conditions is investigated.

3.2 Experimental

3.2.1 Anode slurry preparation

A homogeneous anode slurry was formed and then used in preparing an anode disk and an anode ridge structure by tape casting and microextrusion printing, respectively. The composition of the anode slurry used in this work is shown in **Table 3.1**. 60 wt% NiO powder (FUJIFILM Wako Pure Chemical Corp., Japan) and 40 wt% $(Y_2O_3)_{0.08}(ZrO_2)_{0.92}$ powder (TZ-8Y, Tosoh Corp., Japan) were firstly mixed by planetary ball milling in isopropanol with zirconia balls (ϕ4.0 mm) at 300 rpm for 3 h. After the evaporation of the isopropanol, NiO–YSZ mixture powder was sieved with a 53 μm mesh to remove agglomeration. The mixture powder, ethanol as the organic solvent, and Triton X-100 (MP Biomedicals, LLC, USA) as the dispersant were mixed with zirconia balls (ϕ4.0 mm) at 200 rpm for 24 h. Thereafter, polyvinyl butyral (PVB, Mowital B60H, Kuraray Co., Ltd., Japan) as the binder and polyethylene glycol 400 (PEG 400, FUJIFILM Wako Pure Chemical Corp., Japan) and glycerin (Nacalai Tesque, Inc., Japan) as the plasticizers were added and then mixed for another 24 h to form a homogeneous anode slurry. By measuring the rheological properties of the anode slurry using a rotational double coaxial cylinder viscometer (Viscolead ADV, Fungilab, S.A., Spain), it was confirmed that the slurry is a shear thinning fluid that follows the Ostwald–de Waele relationship (*72*); its power law index and consistency were evaluated as 0.87 and 5.6 Pa $s^{0.87}$, respectively, at 25 °C (see **Fig. 3.1**). Note that the ethanol-based anode slurry prepared in this chapter has very high volatility so that a small amount of extruded slurry can easily maintain its shape despite relatively low viscoelasticity.

Table 3.1 Composition of NiO–YSZ anode slurry in weight ratio.

Powder		Solvent	Dispersant	Binder	Plasticizer	
NiO	YSZ	Ethanol	Triton X-100	PVB	PEG 400	Glycerin
31.8	21.2	33.8	1.06	6.36	2.89	2.89

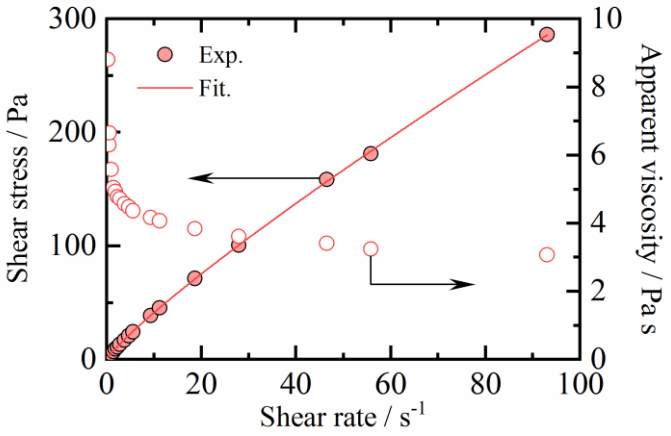

Fig. 3.1 Shear stress and apparent viscosity curves of NiO–YSZ anode slurry.

3.2.2 Cell fabrication

To remove the dissolved gas inside the prepared anode slurry before tape casting, the slurry was degassed under a pressure of 0.15 atm for 10 min during magnetic stirring in a vacuum desiccator. Subsequently, the slurry was cast on a glass substrate at a casting speed of 10 mm s^{-1} and a doctor blade gap of 2.0 mm using a commercial tape caster (Imoto Machinery Co., Ltd., Japan). After fully drying the cast slurry overnight at 20 °C and 80 % relative humidity using a temperature and humidity chamber (Yamato Scientific Co., Ltd., Japan), a green tape was cut into a disk shape with a diameter of 30 mm.

Using a self-made lab-scale 3D printer, which comprises motorized *x*–*y*-axis stages, a manual *z*-axis stage, and a syringe pump, the slurry was printed in a line shape on the surface of the flat green disk in a target region of 20 mm × 20 mm. The slurry was placed into a gas-tight syringe after degassing, then a nozzle tip with an inner diameter of 100 μm (Nordson Corp., USA) was attached to the end of the syringe. Thereafter, the syringe was fixed vertically to the syringe pump. The green disk was placed onto the *z*-axis stage and then fixed. The distance between the disk and the nozzle tip was adjusted to about 120 μm using the *z*-axis stage. The printing of the slurry was conducted at a stage speed of 20 mm s^{-1}, an applied flow rate of 200 nL s^{-1}, and a printing interval of 280 μm. The average width and

average height of the printed slurry were measured to be 140.6 and 35.4 μm, respectively, using a three-dimensional (3D) surface measurement system (VR-3100, Keyence Corp., Japan).

A YSZ electrolyte thin film was prepared by spin coating. A mixture of 10.0 wt% YSZ powder, 0.8 wt% PVB (Sigma-Aldrich Co., LLC, USA), and 89.2 wt% ethanol was added dropwise onto the presintered anode disk and immediately spun at 3000 rpm for 30 s. After 20 cycles of spin coating, the NiO–YSZ anode and YSZ electrolyte were cosintered at 1350 °C for 5 h at heating and cooling rates of 120 and 200 °C h^{-1}, respectively. A GDC barrier layer and an LSCF cathode were prepared by screen printing. A GDC ink composed of 50 wt% $Gd_{0.1}Ce_{0.9}O_{1.95}$ powder (GDC-10(AU), Shin-Etsu Astech Co., Ltd., Japan) and a 50 wt% ink vehicle (VEH, Nexceris, LLC, USA) was prepared by planetary ball milling at 600 rpm for 30 min. The GDC ink was screen-printed on the surface of the YSZ electrolyte with a mask of 20 μm thickness and then sintered at 1250 °C for 2 h. Thereafter, an LSCF ink composed of 67 wt% $La_{0.6}Sr_{0.4}Co_{0.2}Fe_{0.8}O_{3-\delta}$ powder (LSCF-6428-N, Kceracell Co., Ltd., Korea) and a 33 wt% ink vehicle was prepared by the same method as that for the GDC ink. The LSCF ink was screen-printed on the surface of the GDC barrier layer with a mask of 60 μm thickness, which was followed by sintering at 950 °C for 5 h. Each sintering process was conducted at heating and cooling rates of 200 °C h^{-1} except for the cosintering process mentioned above. The apparent geometrical cathode area was *ca.* 0.785 cm^2.

3.2.3 Performance evaluation

The electrochemical characteristics of the cells were investigated at an operating temperature of 700 °C. Prior to the electrochemical testing, NiO in the anode was reduced in a reducing atmosphere at 800 °C for 2 h. Thereafter, mixture gases of 97 % H_2–3 % H_2O and 21 % O_2–79 % N_2 were supplied to the anode and cathode, respectively, whose total flow rate was 100 sccm on both sides. Current–voltage (*i–V*) characteristics were measured using a Solartron 1455A frequency response analyzer and a Solartron 1470E potentio/galvanostat electrochemical interface (Solartron Analytical, UK).

3.2.4 Structure observation

Prior to structural analysis, the cells were cooled down in a reducing atmosphere after the electrochemical testing and then impregnated with epoxy resin (EpoFix, Struers, Denmark) under a pressure of 34 Pa for 10 min. For a mesostructural analysis, the cured samples were cut and polished to observe their cross sections by scanning electron microscopy (SEM) (Miniscope TM3000, Hitachi High-Tech Corp., Japan). For a microstructural analysis (*23*, *73–76*), a small piece of the cured sample was painted with a commercial silver paste (Ted Pella, Inc., USA) and then coated with osmium under a pressure of 8–10 Pa for 10 s. The three-dimensional (3D) microstructures of both electrodes were imaged using an NVision 40 (Carl Zeiss AG, Germany) focused ion beam (FIB) SEM system. An in-lens secondary electron detector and a standard secondary electron detector with an acceleration voltage of 2.0 kV were used to distinguish the solid phases in the Ni–YSZ anode and LSCF cathode, respectively, in SEM images. Sliced SEM images were aligned and segmented into three and two phases for the Ni–YSZ anode and LSCF cathode, respectively, and then reconstructed to quantify microstructural parameters. The phase volume fraction, particle and pore size, tortuosity factor, surface-to-volume ratio, double-phase boundary (DPB) density, and triple-phase boundary (TPB) density were quantified using a commercial 3D visualization and analysis software application “Avizo” (Thermo Fisher Scientific Inc., USA) and an in-house code.

3.3 Numerical simulation

3.3.1 Numerical model

A steady-state 2D numerical model where the structures of the cells after the electrochemical testing were implemented was developed. **Figure 3.2(a)** shows the cross-sectional SEM images of the tested cells. The areas colored with green, yellow, white, and gray in the SEM images correspond to the Ni–YSZ anode, YSZ electrolyte, GDC barrier layer, and LSCF cathode; their average thicknesses in the flat cell were measured to be about 450, 8.0, 6.0, and 36 μm, respectively. On the other hand, the thicknesses of each layer in the mesoscale-modified cell could not be defined because of their inhomogeneity. Therefore, we identified each layer from its cross-sectional SEM image and then obtained geometric shape data using the software "Avizo". The average interval between two adjacent anode ridge structures after sintering at 1350 °C, which was measured to be about 202 μm by a 3D laser confocal scanning microscopy (LEXT OLS4000, Olympus Corp., Japan), was set at a single repeating unit L. The interfacial area enlargement factor α—the ratio of the contact area between the electrode and electrolyte of the mesoscale-modified cell to that of the flat cell—was calculated to be about 1.14 for the anode–electrolyte interface and about 1.08 for the cathode–electrolyte interface. Thereby, the average interfacial area enlargement factor was about 1.11 $= \frac{\alpha_{A-E}L+\alpha_{C-E}L}{L+L}$. Note that the ratio of the cross-sectional area of the YSZ/GDC bilayer in the mesoscale-modified cell to that in the flat cell was calculated to be 1.14. By taking these values into consideration, the calculation domains of each cell were designated as the areas surrounded by the blue solid lines in **Fig. 3.2(b)**. Note that x and y in the orthogonal coordinate system shown in **Fig. 3.2(b)** were defined as the cell width and cell thickness directions, respectively. To reduce computational load, the calculation grid sizes were set at 1×1 μm^2 in a region where y is greater than 420 μm and 1×5 μm^2 in the rest of the region. Taking into account the porosity of the GDC barrier layer (*ca*. 50 %) and the ionic conductivity of GDC (*3*, *77*), the barrier layer thickness was included in the electrolyte thickness as an equivalent YSZ thickness (*78*). The electrode microstructures were assumed to be homogeneous in the entire

regions of each electrode. **Figures 3.2(c)** and **3.2(d)** show the 3D reconstructed structures of the electrodes, whose volumes were 14.86 × 21.05 × 12.96 and 9.74 × 11.45 × 9.75 μm^3 for the Ni–YSZ anode and LSCF cathode, respectively. The microstructural parameters quantified by the FIB-SEM analysis summarized in **Table 3.2** were used in the numerical simulation.

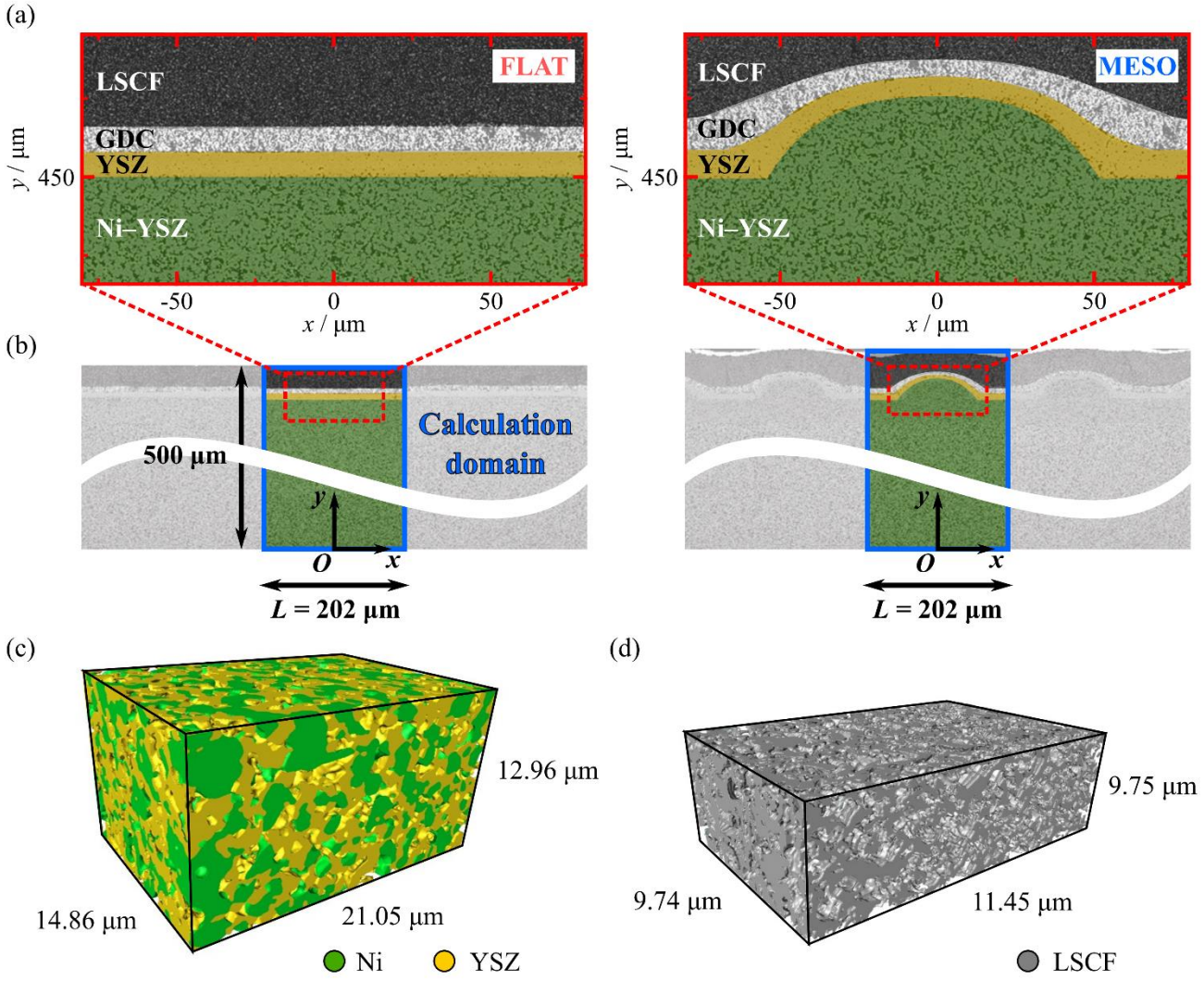

Fig. 3.2 (a) Cross-sectional SEM images and (b) calculation domains of cells, and 3D reconstructed structures of (c) Ni–YSZ anode and (d) LSCF cathode.

Table 3.2 Microstructural parameters of electrodes of tested cells.

Parameter	Anode			Cathode	
	Ni	YSZ	Pore	LSCF	Pore
Volume fraction / %	33.0	38.9	28.1	54.6	45.4
Particle/pore size / μm	1.50	1.12	0.955	0.218	0.211
Tortuosity factor / –	3.43	2.33	7.89	2.64	1.79
Surface-to-volume ratio / $\mu m^2\ \mu m^{-3}$	4.02	5.37	5.97	11.1	13.4
DPB density / $\mu m^2\ \mu m^{-3}$	–			6.07	
TPB density / $\mu m\ \mu m^{-3}$	2.29			–	

3.3.2 Governing equations

Conservation of electrons and oxide ions are expressed as

$$\nabla \cdot \left(\frac{\sigma_{e^-}^{eff}}{F} \nabla \mu_{e^-} \right) = -i_{ct} \tag{3.1}$$

$$\nabla \cdot \left(\frac{\sigma_{O^{2-}}^{eff}}{2F} \nabla \mu_{O^{2-}} \right) = i_{ct}, \tag{3.2}$$

where $\sigma_{e^-}^{eff}$ and $\sigma_{O^{2-}}^{eff}$ are respectively the effective electronic and ionic conductivities, F is the Faraday constant, $\bar{\mu}_{e^-}$ and $\mu_{O^{2-}}$ are respectively the electrochemical potentials of the electrons and oxide ions, and i_{ct} is the charge-transfer current density associated with the electrochemical reactions in the electrodes. In this numerical model, LSCF, Ni, and YSZ were considered as mixed ion-electron, pure electron, and pure ion conductors, respectively.

Gas diffusion in the electrodes is expressed by the dusty-gas model (*79–82*).

$$\nabla \cdot N_i = s_i \tag{3.3}$$

$$\frac{N_i}{D_{i,\mathrm{K}}^{\mathrm{eff}}} + \sum_{j=1,j\neq i}^{n} \frac{X_j N_i - X_i N_j}{D_{ij}^{\mathrm{eff}}} = -\frac{P_{\mathrm{t}}}{RT}\nabla X_i - \frac{X_i}{RT}\left(1 + \frac{K P_{\mathrm{t}}}{\mu D_{i,\mathrm{K}}^{\mathrm{eff}}}\right)\nabla P_{\mathrm{t}} \tag{3.4}$$

Here, N_i and X_i represent the molar flux and molar fraction, respectively, and s_i is the sink/source term associated with the electrochemical reaction as

$$s_{\mathrm{H_2}} = -\frac{i_{\mathrm{ct}}}{2F},\ s_{\mathrm{H_2O}} = \frac{i_{\mathrm{ct}}}{2F},\ s_{\mathrm{O_2}} = -\frac{i_{\mathrm{ct}}}{4F},\ s_{\mathrm{N_2}} = 0. \tag{3.5}$$

Also, $D_{i,\mathrm{K}}^{\mathrm{eff}}$ and D_{ij}^{eff} are respectively the effective Knudsen and effective molecular diffusivities, and P_{t}, K, and μ are respectively the total pressure, permeability, and mixture viscosity.

The effective conductivities and gas diffusivities were evaluated by modifying bulk transport coefficients using the ratio of the volume fraction V_i to the tortuosity factor τ_i as

$$\Gamma_i^{\mathrm{eff}} = \frac{V_i}{\tau_i}\Gamma_i \ \ (\Gamma_i \equiv \sigma_{\mathrm{e^-}}, \sigma_{\mathrm{O^{2-}}}, D_{i,\mathrm{K}}, D_{ij}). \tag{3.6}$$

Empirical formulas for the bulk conductivities and bulk gas diffusivities were used as (*83–87*)

$$\log \sigma_{\mathrm{e^-,LSCF}} = -0.0095\left(\log\frac{P_{\mathrm{O_2}}}{10^5}\right)^2 - 0.0011\log\frac{P_{\mathrm{O_2}}}{10^5} + 4.8152 \tag{3.7}$$

$$\sigma_{\mathrm{e^-,Ni}} = 3.27\times 10^6 - 1065.3T \tag{3.8}$$

$$\sigma_{\mathrm{O^{2-},LSCF}} = \frac{8F^2\widetilde{D}}{RTV_{\mathrm{m}}}\frac{\partial\delta}{\partial \ln P_{\mathrm{O_2}}} \tag{3.9}$$

$$\sigma_{\mathrm{O^{2-},YSZ}} = 3.40\times 10^4 \exp\left(-\frac{10350}{T}\right) \tag{3.10}$$

$$D_{i,\mathrm{K}} = \frac{d_{\mathrm{pore}}}{3}\sqrt{\frac{8RT}{10^{-3}\pi M_i}} \tag{3.11}$$

$$D_{ij} = \frac{0.01013T^{1.75}\left(M_i^{-1}+M_j^{-1}\right)^{1/2}}{P_{\mathrm{t}}\left[\left(\sum_i \upsilon_i\times 10^6\right)^{1/3}+\left(\sum_j \upsilon_j\times 10^6\right)^{1/3}\right]^2}. \tag{3.12}$$

Here, $\widetilde{D}$ is the chemical diffusion coefficient, which is expressed as (*83*)

$$\log \widetilde{D} = -0.1882 \left(\log \frac{P_{O_2}}{10^5}\right)^2 - 0.2490 \log \frac{P_{O_2}}{10^5} - 9.7676. \quad (3.13)$$

Also, V_m is the perovskite molar volume and was set at 35.17 cm^3 mol^{-1} (*88*) in this work. δ is the oxygen nonstoichiometry, d_{pore} is the mean pore diameter, M_i is the molecular mass, and v_i is the molecular diffusion volume. The permeability of the porous electrodes was evaluated using Eq. (3.14) proposed by Kishimoto et al. (*74*).

$$K = \frac{V_{pore}}{6\tau_{pore}(S/V)_{pore}^2} \quad (3.14)$$

Here, $(S/V)_{pore}$ indicates the surface-to-volume ratio of the pore phase.

The electrochemical reactions are assumed to occur at TPBs in the Ni–YSZ anode and DPBs in the LSCF cathode, which are described with the nonlinear Butler–Volmer-type equations (*84*, *89*) as

$$i_{ct,ano} = i_{0,TPB,ano} l_{TPB,ano} \left[\exp\left(\frac{2F}{RT}\eta_{act,ano}\right) - \exp\left(-\frac{F}{RT}\eta_{act,ano}\right)\right] \quad (3.15)$$

$$i_{ct,cat} = i_{0,DPB,cat} A_{DPB,cat} \left[\exp\left(\frac{1.2F}{RT}\eta_{act,cat}\right) - \exp\left(-\frac{F}{RT}\eta_{act,cat}\right)\right]. \quad (3.16)$$

Here, i_0 indicates the exchange current density and was given by (*90*, *91*)

$$i_{0,TPB,ano} = 1.30 \times 10^{-3} P_{H_2}^{0.11} P_{H_2O}^{0.67} \exp\left(-\frac{8.49\times10^4}{RT}\right) \quad (3.17)$$

$$i_{0,DPB,cat} = 1.47 \times 10^{6} P_{O_2}^{0.2} \exp\left(-\frac{8.59\times10^4}{RT}\right). \quad (3.18)$$

$l_{\mathrm{TPB,ano}}$ and $A_{\mathrm{DPB,cat}}$ represent the TPB and DPB densities, respectively, for which the quantified values obtained from the microstructural analysis shown in **Table 3.2** were used. η_{act} is the activation overpotential and was defined as

$$\eta_{\mathrm{act,ano}} = -\frac{1}{2F}\left(2\mu_{\mathrm{e}^-} - \mu_{\mathrm{O}^{2-}} + \Delta G_0 - RT\ln\frac{P_{\mathrm{H_2}}^{\mathrm{bulk}}}{P_{\mathrm{H_2O}}^{\mathrm{bulk}}}\right) - \eta_{\mathrm{con,ano}} \tag{3.19}$$

$$\eta_{\mathrm{act,cat}} = -\frac{1}{2F}\left(2\mu_{\mathrm{e}^-} - \mu_{\mathrm{O}^{2-}} + \frac{RT}{2}\ln P_{\mathrm{O_2}}^{\mathrm{bulk}}\right) - \eta_{\mathrm{con,cat}}. \tag{3.20}$$

Here, ΔG_0 indicates the standard Gibbs free energy change associated with the hydrogen oxidation reaction and η_{con} is the concentration overpotential and was defined as

$$\eta_{\mathrm{con,ano}} = \frac{RT}{2F}\ln\left(\frac{P_{\mathrm{H_2}}^{\mathrm{bulk}}}{P_{\mathrm{H_2}}}\frac{P_{\mathrm{H_2O}}}{P_{\mathrm{H_2O}}^{\mathrm{bulk}}}\right) \tag{3.21}$$

$$\eta_{\mathrm{con,cat}} = \frac{RT}{4F}\ln\left(\frac{P_{\mathrm{O_2}}}{P_{\mathrm{O_2}}^{\mathrm{bulk}}}\right). \tag{3.22}$$

3.3.3 Boundary conditions

Boundary conditions on the electrode surfaces are summarized in **Table 3.3** (t_{cell} indicates the cell thickness). The cell temperature was assumed to be constant and uniform in the entire cell and set at 700 °C. Mixture gases of 97 % H_2–3 % H_2O and 21 % O_2–79 % N_2 were assumed to be supplied to the anode and cathode surfaces, respectively. The total pressure on the surfaces of both electrodes was set at 1 atm. The electrochemical potential of the electrons was set at the product of the terminal voltage V_{T} and the Faraday constant F at the anode surface and zero at the cathode surface (*92*). The gradients of the electrochemical potentials of the oxide ions at the electrode surfaces were set at zero. Symmetric boundary conditions were set on the side boundaries $x = \pm\frac{L}{2}$ for all variables.

Table 3.3 Boundary conditions on electrode surfaces.

Variables	Anode surface ($y = 0$)	Cathode surface ($y = t_{\mathrm{cell}}$)
H_2 partial pressure	$P_{H_2}(x,0) = P_{H_2}^{\mathrm{bulk}}$	–
H_2O partial pressure	$P_{H_2O}(x,0) = P_{H_2O}^{\mathrm{bulk}}$	–
O_2 partial pressure	–	$P_{O_2}(x,t_{\mathrm{cell}}) = P_{O_2}^{\mathrm{bulk}}$
N_2 partial pressure	–	$P_{N_2}(x,t_{\mathrm{cell}}) = P_{N_2}^{\mathrm{bulk}}$
Electrochemical potential of electrons	$\mu_{e^-}(x,0) = FV_{\mathrm{T}}$	$\mu_{e^-}(x,t_{\mathrm{cell}}) = 0$
Electrochemical potential of oxide ions	$\frac{\partial \mu_{O^{2-}}}{\partial y}(x,0) = 0$	$\frac{\partial \mu_{O^{2-}}}{\partial y}(x,t_{\mathrm{cell}}) = 0$

3.3.4 Overpotential evaluation

To quantitatively understand the improvement in the electrochemical performance of anode-supported SOFCs by the mesostructural modification, the average ohmic, average activation, and average concentration losses in the cells were introduced (*40*, *93*). In the previous work (*40*), the local ohmic loss attributed to oxide ion transport was calculated on the basis of the potential difference between an arbitrary point in an electrode and a reference point at the electrode–electrolyte interface. However, this calculation method cannot be applied to a mesoscale-modified cell because a definite reference potential cannot be specified (*40*). In this work, therefore, another calculation method for the average ohmic loss in the cell is proposed. The average ohmic loss η_{ohm} was calculated by averaging the total Joule heating with the total current as

$$\eta_{\mathrm{ohm}} = \frac{\sigma^{-1} \int\int i^2 dxdy}{\int\int i_{\mathrm{ct}} dxdy}, \tag{3.23}$$

where i is the local current density.

The average activation η_{act} and average concentration overpotentials η_{con} in each electrode were calculated by averaging the total energy loss with the total current as (*40*, *93*)

$$\eta_{\text{act}} = \frac{\eta_{\text{act}} i_{\text{ct}} dxdy}{i_{\text{ct}} dxdy} \tag{3.24}$$

$$\eta_{\text{con}} = \frac{\eta_{\text{con}} i_{\text{ct}} dxdy}{i_{\text{ct}} dxdy}. \tag{3.25}$$

3.4 Results and discussion

3.4.1 Model validity

Figure 3.3 shows the *i–V* and current–power (*i–P*) curves of the cells obtained from the experiment and numerical simulation at 700 °C. Note that the average current density was defined as the total current divided by the apparent electrode area. It is found that the electrochemical performance of the mesoscale-modified cell is improved compared with that of the flat cell under the same operating conditions in both the experimental and numerical results. This indicates that the cell overpotential is successfully reduced by the mesostructural modification of the electrode–electrolyte interface. Although small gaps between the measured and simulated data exist, the simulation results well reproduce the experimental ones because the structures of the tested cells were implemented in the numerical model we developed. Note that the gaps may be caused by an overestimation of the activation overpotential in the cathode; this is because the electrochemical reaction that occurs at the LSCF–GDC–pore TPBs, which also contributes to the electrochemical performance of SOFCs (*42*, *94*), was not taken into account in the numerical model. Additionally, an error associated with the contribution of gas diffusion within the anode may result in the gaps, particularly in a high current density region. Although the dusty-gas model was used in analyzing the gas diffusion in the electrodes

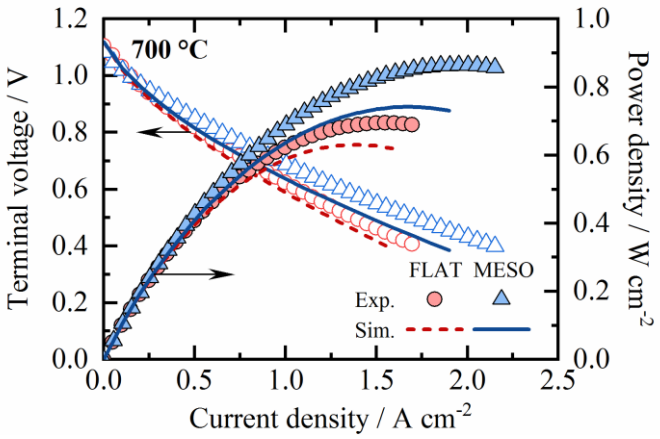

Fig. 3.3 *i–V* and *i–P* curves of cells obtained from experiment (scatter plots) and numerical simulation (line graphs) at 700 °C.

in this work, whether the existing gas diffusion models (*81*, *82*, *95–99*) can accurately express a phenomenon of mass transport within porous electrodes remains to be clarified. Nonetheless, a good agreement is achieved between the experimental and simulation results, so that the numerical model developed in this work is feasible for further quantitative analysis.

3.4.2 Cell overpotential

The average values of each overpotential component in the cells at an average current density of 1.0 A cm^{-2} at 700 °C as a representative operating condition are shown in **Fig. 3.4**. Also, the ohmic losses due to the electron transport in each cell component of the order of 0.01 mV and the concentration overpotential in the cathode of the order of 0.1 mV are omitted from the graphs. The percentages written between the bar graphs are the changes in each overpotential component of the mesoscale-modified cell relative to the flat cell; the plus and minus signs represent an increase and decrease, respectively. It is found that the total overpotential in the mesoscale-modified cell (481 mV) is 9.21 % (48.8 mV) smaller than that in the flat cell (530 mV). This is because all the overpotential components except for the concentration overpotential in the anode are reduced by the mesostructural modification of the electrode–electrolyte interface.

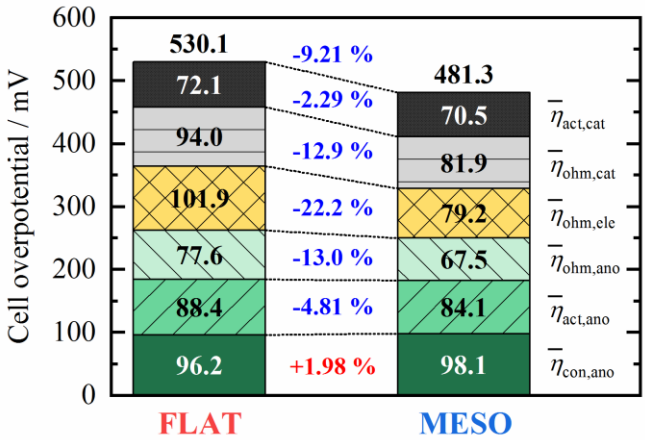

Fig. 3.4 Overpotential components in cells at 1.0 A cm^{-2} at 700 °C and their changes of mesoscale-modified cell relative to flat cell.

The ohmic loss due to the oxide ion transport in the electrolyte in the mesoscale-modified cell is 22.2 % (22.7 mV) lower than that in the flat cell. The relative decrease in the ohmic loss RD_{ohm} can be calculated as

$$RD_{\mathrm{ohm}} = 1 - \frac{\eta_{\mathrm{ohm,MESO}}}{\eta_{\mathrm{ohm,FLAT}}}. \tag{3.26}$$

The right-hand side of Eq. (3.26) is equal to the relative decrease in Joule heating, so that it can be re-written as

$$RD_{\mathrm{ohm}} = 1 - \frac{Q_{\mathrm{ohm,MESO}}}{Q_{\mathrm{ohm,FLAT}}}. \tag{3.27}$$

Here, Q_{ohm} is the Joule heating and can be expressed as

$$Q_{\mathrm{ohm}} = \sigma^{-1} \quad i^2 dxdy. \tag{3.28}$$

Consider a situation where the same electric current is applied to both a flat cell and a mesoscale-modified cell where the electrode–electrolyte interfacial area is α times larger than that in the flat cell. Assuming that the ionic current in the mesoscale-modified cell uniformly flows inside the electrolyte to the electrolyte thickness direction, it is reduced to $1/\alpha$ times that in the flat cell. If the electrolyte thickness t_{ele} is homogenous, the Joule heating in the electrolyte in the flat cell $Q_{\mathrm{ohm,ele,FLAT}}$ and the mesoscale-modified cell $Q_{\mathrm{ohm,ele,MESO}}$ can be respectively expressed as

$$Q_{\mathrm{ohm,ele,FLAT}} = \frac{i_{\mathrm{cell}}^2}{\sigma_{\mathrm{O^{2-},YSZ}}/t_{\mathrm{ele}}} L \tag{3.29}$$

$$Q_{\mathrm{ohm,ele,MESO}} = \frac{(i_{\mathrm{cell}}/\alpha)^2}{\sigma_{\mathrm{O^{2-},YSZ}}/t_{\mathrm{ele}}} \alpha L. \tag{3.30}$$

Here, i_{cell} is the current density. Thus, the relative decrease in the ohmic loss in the electrolyte $RD_{\mathrm{ohm,ele}}$ can be estimated as

$$RD_{\mathrm{ohm,ele}} = 1 - \frac{1}{\alpha}. \tag{3.31}$$

According to Eq. (3.31), the relative decrease in the ohmic loss in the electrolyte is estimated to be constant at 10.1 % (=1-1/1.11); however, that obtained from the simulation (22.2 %) is much larger than the estimate. This mismatch suggests that the assumption that the ionic current uniformly flows inside an electrolyte is incorrect because of the inhomogeneous electrolyte thickness in the mesoscale-modified cell. This issue will be discussed later.

The activation overpotentials in the anode and cathode in the mesoscale-modified cell are 4.81 % (4.25 mV) and 2.29 % (1.65 mV) lower than those in the flat cell, respectively. The activation overpotential, which is attributed to the electrochemical reaction that takes place at the reaction sites distributed in the electrochemically active region, is reduced owing to a decrease in the electrochemical reaction amount per unit reaction site. This is because the area of the electrochemically active regions in both electrodes is extended by the mesostructural modification of the electrode–electrolyte interface. Similar to Eqs. (3.26) and (3.27), the relative decrease in the activation overpotential RD_{act} can be calculated as

$$RD_{\mathrm{act}} = 1 - \frac{\eta_{\mathrm{act,MESO}}}{\eta_{\mathrm{act,FLAT}}} = 1 - \frac{Q_{\mathrm{act,MESO}}}{Q_{\mathrm{act,FLAT}}}. \tag{3.32}$$

Here, Q_{act} is the energy loss per associated with the electrochemical reaction and is expressed as

$$Q_{\mathrm{act}} = \quad \eta_{\mathrm{act}} i_{\mathrm{ct}} dxdy. \tag{3.33}$$

The activation overpotential η_{act} can be simply expressed by approximating the nonlinear Butler–Volmer-type equation as

$$\eta_{\text{act}} \cong \frac{RT}{\beta F}\sinh^{-1}\left(\frac{i_{\text{ct}}}{2i_0}\right), \tag{3.34}$$

where β is a constant. In this chapter, to approximate Eqs. (3.15) and (3.16) to the sine hyperbolic function, constants are given as 1.5 and 1.1, respectively. Substituting Eq. (3.34) into Eq. (3.33) gives

$$Q_{\text{act}} \cong \left(\frac{RT}{\beta F}\sinh^{-1}\left(\frac{i_{\text{ct}}}{2i_0}\right) i_{\text{ct}}\right) dxdy. \tag{3.35}$$

When the electrochemical reaction uniformly occurs inside an effective reaction region with a constant thickness t_{eff} of adjacent to the electrode–electrolyte interface, the following equations can be established:

$$\iota_{\text{ct,FLAT}} = \frac{i_{\text{cell}}}{t_{\text{eff}}}. \tag{3.36}$$

$$\iota_{\text{ct,MESO}} = \frac{i_{\text{cell}}}{\alpha t_{\text{eff}}}. \tag{3.37}$$

Here, ι_{ct} is a uniform charge-transfer current density. Assuming that t_{eff} is sufficiently small compared with the mesostructure, the activation energy losses in the flat cell $Q_{\text{act,FLAT}}$ and the mesoscale-modified cell $Q_{\text{act,MESO}}$ can be respectively written as

$$Q_{\text{act,FLAT}} \cong \frac{RT}{\beta F}\sinh^{-1}\left(\frac{i_{\text{cell}}}{2i_0 t_{\text{eff}}}\right) \times \frac{i_{\text{cell}}}{t_{\text{eff}}} \times L \times t_{\text{eff}} \tag{3.38}$$

$$Q_{\text{act,MESO}} \cong \frac{RT}{\beta F}\sinh^{-1}\left(\frac{i_{\text{cell}}}{2i_0 \alpha t_{\text{eff}}}\right) \times \frac{i_{\text{cell}}}{\alpha t_{\text{eff}}} \times \alpha L \times t_{\text{eff}}. \tag{3.39}$$

Thus, the relative decrease in the activation overpotential in the electrode can be estimated as

$$RD_{\mathrm{act}} = 1 - \frac{\sinh^{-1}\left(\frac{i_{\mathrm{cell}}}{2i_0 \alpha t_{\mathrm{eff}}}\right)}{\sinh^{-1}\left(\frac{i_{\mathrm{cell}}}{2i_0 t_{\mathrm{eff}}}\right)}. \tag{3.40}$$

According to Eq. (3.40), when the realistic values of 5–20 μm (*5*, *7*, *9*, *11*, *12*) are applied to the thickness of the effective reaction region t_{eff}, the relative decreases in the activation overpotentials in the anode are estimated to be 6.32–10.5 % and those in the cathode are 6.88–7.52 %. However, those obtained from the simulation (4.81 % in the anode and 2.29 % in the cathode) are smaller than each estimate. These mismatches may be drawn from the fact that the assumption that the electrochemical reaction uniformly occurs inside an effective reaction region is inappropriate, which will also be discussed later.

The concentration overpotential in the anode in the mesoscale-modified cell is 1.98 % (1.90 mV) higher than that in the flat cell. This is mainly caused by the fact that the average anode thickness in the mesoscale-modified cell is increased by about 18.1 μm compared with that in the flat cell by attaching the anode ridge structures on the surface of the anode disk; the concentration overpotential in the anode in a flat cell where the anode thickness was set at 470 μm (≈ 450+18.1 μm) is simulated to be 98.2 mV (not shown), which is almost the same as that in the mesoscale-modified cell. In addition, the increase in the concentration overpotential in the anode is relatively small, suggesting that it rarely hinders the improvement in cell performance under such a high hydrogen partial pressure condition set in this work.

3.4.3 Physicochemical quantities within mesoscale-modified cell

As mentioned in the previous section, the relative decreases in the ohmic and activation overpotentials obtained from the simulation differ from those estimated under the assumptions that the local ionic and charge-transfer current densities are uniformly distributed inside a cell. It is presumed

that the mismatches are caused by other factors such as the interfacial area enlargement and thickness inhomogeneity in the mesoscale-modified cell (see **Fig. 3.2(a)**). In this section, therefore, distributions of the physicochemical quantities that contribute to the electrochemical reactions in the cells are analyzed and the mismatches are quantitatively discussed on the basis of the energy losses attributed to such quantities.

3.4.3.1 Electrochemical potential of oxide ions

Figure 3.5 shows the distributions of the electrochemical potential of the oxide ions $\mu_{O^{2-}}$ in the flat and mesoscale-modified cells at 1.0 A cm^{-2} at 700 °C. Note that the dotted black lines in **Fig. 3.5** represent the electrode–electrolyte interface. It is found that the equipotential lines of the electrochemical potential of the oxide ions in the mesoscale-modified cell are not formed in parallel with the electrode–electrolyte interface; similar trends were reported in the literature (*27*, *39*, *40*, *44*, *45*). This means that the electrochemical potentials of oxide ions at points (calculation grids) located at the same distance from the electrode–electrolyte interface in the mesoscale-modified cell is not the same, unlike those in the flat cell.

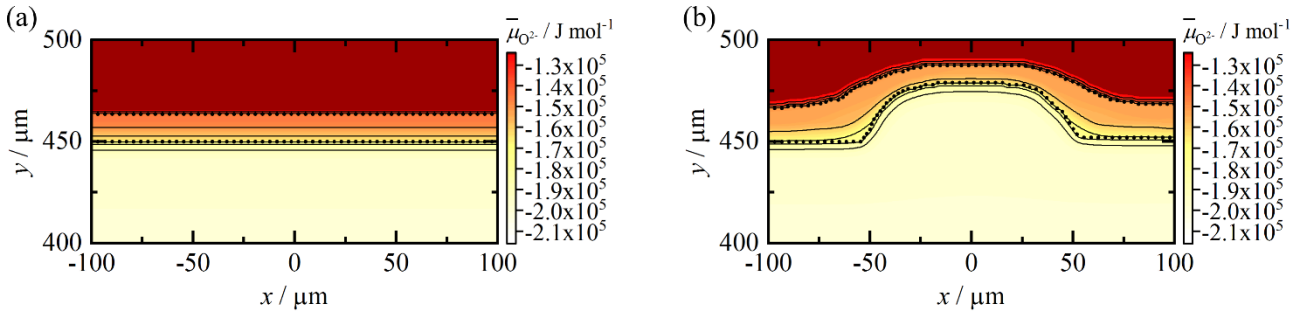

Fig. 3.5 Distributions of electrochemical potential of oxide ions in (a) flat cell and (b) mesoscale-modified cell at 1.0 A cm^{-2} at 700 °C (Dotted black lines: electrode–electrolyte interface).

3.4.3.2 Ionic current density

Figure 3.6 shows the distributions of the magnitude of the ionic current density $i_{O^{2-}}$ $(= \|\boldsymbol{i}_{O^{2-}}\|)$ in the flat and mesoscale-modified cells at 1.0 A cm^{-2} at 700 °C. The ionic current density in the electrolyte in the mesoscale-modified cell has a nonuniform distribution, contrary to that in the flat cell. That is, the assumption that the ionic current uniformly flows inside an electrolyte is incorrect for the mesoscale-modified cell prepared in this work. Therefore, the relative decrease in the ohmic loss in the electrolyte cannot be correctly expressed using Eq. (3.31).

In the mesoscale-modified cell, the local ionic current density becomes higher in regions where the local electrolyte thickness is smaller, and lower in regions where it is larger, as shown in **Fig. 3.6(b)**. From this fact, it can be inferred that not only the interfacial area enlargement but also the thickness inhomogeneity reduces the ohmic loss. From this, the relative decrease in the Joule heating in the electrolyte (Eq. (3.27)) is expressed by the form of the superposition of the effects of the two structural features in the mesoscale-modified cell as

$$RD_{\mathrm{ohm,ele}} = 1 - \frac{Q_{\mathrm{ohm,ele,MESO}}}{Q_{\mathrm{ohm,ele,FLAT}}} = 1 - \frac{Q_{\mathrm{ohm,ele,MESO}}}{Q_{\mathrm{ohm,ele,FLAT}}} \quad \frac{Q_{\mathrm{ohm,ele,MESO}}}{Q_{\mathrm{ohm,ele,MESO}}} \quad . \tag{3.41}$$

Here, $Q_{\mathrm{ohm,ele,MESO}}$ indicates the Joule heating in the electrolyte in a mesoscale-modified cell where

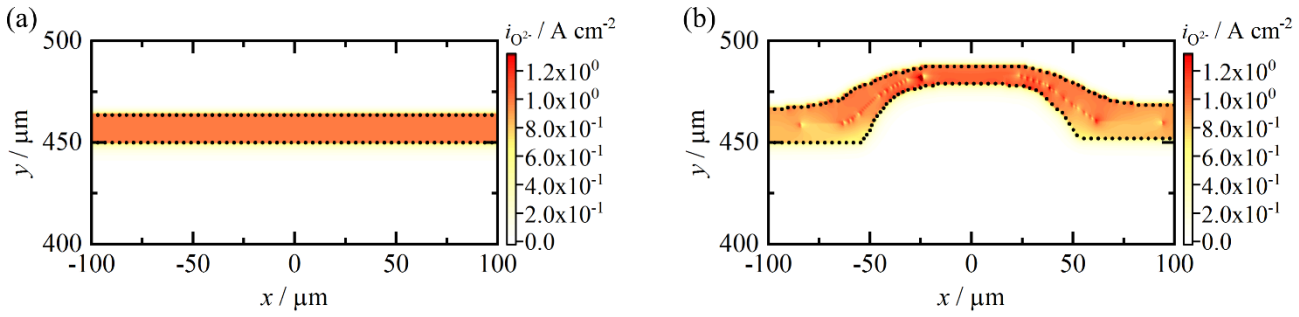

Fig. 3.6 Distributions of ionic current density in (a) flat cell and (b) mesoscale-modified cell at 1.0 A cm^{-2} at 700 °C (Dotted black lines: electrode–electrolyte interface).

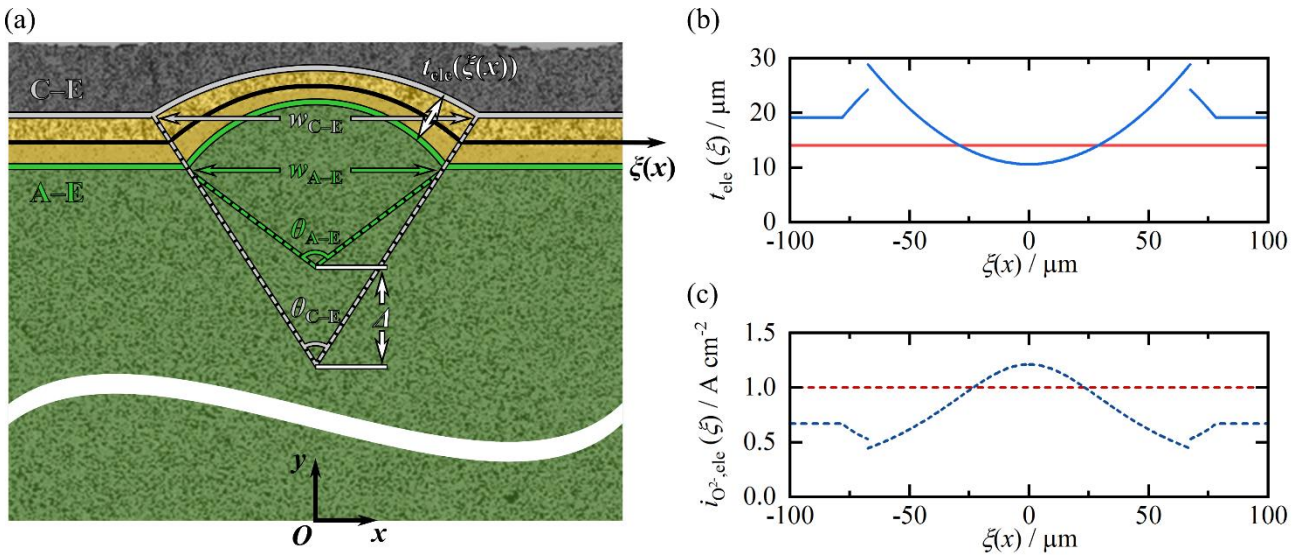

Fig. 3.7 (a) Approximated geometric shapes of electrode–electrolyte interface in mesoscale-modified cell based on SEM image and (b) electrolyte thickness and (c) ionic current density in electrolyte in flat and mesoscale-modified cells.

the electrode–electrolyte interfacial area is extended α by compared with that in the flat cell and has a homogeneous thickness. Note that the first and second ratios on the rightmost-hand side of Eq. (3.41) correspond to the interfacial area enlargement and thickness inhomogeneity effects on Joule heating, respectively.

To mathematically analyze the structural effects, I model the geometric shapes of the electrode–electrolyte interface in the mesoscale-modified cell with a circular arc in the patterned area and a straight line in the nonpatterned area, as shown in **Fig. 3.7(a)**. In this study, the electrolyte thickness $t_{ele}\left(\xi(x)\right)$ is defined in the direction perpendicular to the centerline between the interfaces (ξ-axis) and is approximated as follows (further details in Appendix A):

$$t_{\mathrm{ele}}\left(\xi(x)\right) = \begin{cases} \dfrac{w_{\mathrm{C\text{–}E}}}{2\sin\frac{\theta_{\mathrm{C\text{–}E}}}{2}} - \dfrac{w_{\mathrm{A\text{–}E}}}{2\sin\frac{\theta_{\mathrm{A\text{–}E}}}{2}} - \Delta, & x = 0 \\ \sqrt{\left(\dfrac{w_{\mathrm{C\text{–}E}}}{2\sin\frac{\theta_{\mathrm{C\text{–}E}}}{2}}\right)^2 - \dfrac{\left(B(x)+\frac{\Delta}{2}\right)^2}{\left(A(x)\right)^2+1}} - \sqrt{\left(\dfrac{w_{\mathrm{A\text{–}E}}}{2\sin\frac{\theta_{\mathrm{A\text{–}E}}}{2}}\right)^2 - \dfrac{\left(B(x)-\frac{\Delta}{2}\right)^2}{\left(A(x)\right)^2+1}} - \dfrac{A(x)\Delta}{\sqrt{\left(A(x)\right)^2+1}}, & 0 < |x| \le \dfrac{w_{\mathrm{A\text{–}E}}+w_{\mathrm{C\text{–}E}}}{4} \\ \sqrt{\left(\dfrac{w_{\mathrm{C\text{–}E}}}{2\sin\frac{\theta_{\mathrm{C\text{–}E}}}{2}}\right)^2 - x^2} - \dfrac{w_{\mathrm{A\text{–}E}}}{2\tan\frac{\theta_{\mathrm{A\text{–}E}}}{2}} - \Delta, & \dfrac{w_{\mathrm{A\text{–}E}}+w_{\mathrm{C\text{–}E}}}{4} \le |x| \le \dfrac{w_{\mathrm{C\text{–}E}}}{2} \\ \dfrac{w_{\mathrm{C\text{–}E}}}{2\tan\frac{\theta_{\mathrm{C\text{–}E}}}{2}} - \dfrac{w_{\mathrm{A\text{–}E}}}{2\tan\frac{\theta_{\mathrm{A\text{–}E}}}{2}} - \Delta, & \text{otherwise} \end{cases}. \tag{3.42}$$

Here, w and θ are the width of the ridge structure and central angle of the arc, respectively. Δ indicates the distance between the centers of the arcs and can be calculated as

$$\Delta = \frac{w_{\mathrm{C\text{–}E}}}{2\sin\frac{\theta_{\mathrm{C\text{–}E}}}{2}} - \frac{w_{\mathrm{A\text{–}E}}}{2\sin\frac{\theta_{\mathrm{A\text{–}E}}}{2}} - t_{\mathrm{ele,top}}, \tag{3.43}$$

where $t_{\mathrm{ele,top}}$ is the electrolyte thickness at the top of the corrugated structure. $A(x)$ and $B(x)$ are respectively described as

$$A(x) = \frac{\sqrt{\left(\frac{w_{\mathrm{C\text{–}E}}}{2\sin\frac{\theta_{\mathrm{C\text{–}E}}}{2}}+\frac{w_{\mathrm{A\text{–}E}}}{2\sin\frac{\theta_{\mathrm{A\text{–}E}}}{2}}\right)^2-\Delta^2}\sqrt{\left(\frac{w_{\mathrm{C\text{–}E}}}{2\sin\frac{\theta_{\mathrm{C\text{–}E}}}{2}}+\frac{w_{\mathrm{A\text{–}E}}}{2\sin\frac{\theta_{\mathrm{A\text{–}E}}}{2}}\right)^2-\Delta^2-4x^2}}{2\left(\frac{w_{\mathrm{C\text{–}E}}}{2\sin\frac{\theta_{\mathrm{C\text{–}E}}}{2}}+\frac{w_{\mathrm{A\text{–}E}}}{2\sin\frac{\theta_{\mathrm{A\text{–}E}}}{2}}\right)x} \tag{3.44}$$

$$B(x) = \frac{\Delta^2}{\frac{w_{\mathrm{C\text{–}E}}}{2\sin\frac{\theta_{\mathrm{C\text{–}E}}}{2}}+\frac{w_{\mathrm{A\text{–}E}}}{2\sin\frac{\theta_{\mathrm{A\text{–}E}}}{2}}}\sqrt{\frac{1}{4}-\frac{x^2}{\left(\frac{w_{\mathrm{C\text{–}E}}}{2\sin\frac{\theta_{\mathrm{C\text{–}E}}}{2}}+\frac{w_{\mathrm{A\text{–}E}}}{2\sin\frac{\theta_{\mathrm{A\text{–}E}}}{2}}\right)^2-\Delta^2}}. \tag{3.45}$$

Note that the electrolyte thickness in the mesoscale-modified cell, which is represented as the blue solid line in **Fig. 3.7(b)**, has discontinuities at $|x| = \frac{w_{\mathrm{A\text{–}E}}+w_{\mathrm{C\text{–}E}}}{4}$ (*i.e.*, $|\xi(x)| = \frac{(\alpha-1)L}{2} + \frac{w_{\mathrm{A\text{–}E}}+w_{\mathrm{C\text{–}E}}}{4}$) because the electrode–electrolyte interface was modeled by the combination of the two different shapes.

Since an equipotential line of the electrochemical potential of oxide ions is formed on the electrode–electrolyte interface, as shown in **Fig. 3.5(b)**, its difference between the interfaces $\Delta\overline{\mu}_{O^{2-}}$ is constant and can be expressed as

$$\Delta\overline{\mu}_{O^{2-}} = \overline{\mu}_{O^{2-},C-E} - \overline{\mu}_{O^{2-},A-E} = -2F \int \frac{\mathbf{i}_{O^{2-},ele}}{\sigma_{O^{2-},YSZ}} \bullet d\mathbf{r} = \text{constant}. \tag{3.46}$$

Here, $\overline{\mu}_{O^{2-},C-E}$ and $\overline{\mu}_{O^{2-},A-E}$ are respectively the electrochemical potentials of oxide ions at the cathode–electrolyte interface and anode–electrolyte interface, $\mathbf{i}_{O^{2-},ele}$ is the ionic current density vector flowing in the electrolyte, and $d\mathbf{r}$ is an infinitesimal displacement vector perpendicular to the ξ-axis direction. Now, supposing that a constant ionic current flows along the ξ-axis direction, then

$$\mathbf{i}_{O^{2-},ele} \bullet d\mathbf{r} = i_{O^{2-},ele}\left(\xi(x)\right) t_{ele}\left(\xi(x)\right) = \text{constant}. \tag{3.47}$$

When a mesoscale-modified cell where the electrode–electrolyte interfacial area is extended by α compared with that in the flat cell has an electrolyte with a homogeneous thickness of $(k/\alpha)t_{ele,FLAT}$, the following equation can be established:

$$i_{O^{2-},ele}\left(\xi(x)\right) t_{ele}\left(\xi(x)\right) = \frac{i_{cell}}{\alpha} \times \frac{k}{\alpha} t_{ele,FLAT}. \tag{3.48}$$

Here, k is the ratio of the electrolyte volume in the mesoscale-modified cell to that in the flat cell and $t_{ele,FLAT}$ is the electrolyte thickness in the flat cell. Note that the electrolyte volume in the mesoscale-modified cell is slightly larger than that in the flat cell, as mentioned in Section 3.3.1, *i.e.*, the ratio of the electrolyte thickness in the mesoscale-modified cell to that in the flat cell k/α (=1.02) is greater than 1. By using the above relationship, the ionic current density in the electrolyte in the mesoscale-modified cell, which is represented as the blue dashed line in **Fig. 3.7(c)**, can be expressed as

$$i_{\mathrm{O}^{2-},\mathrm{ele}}\left(\xi(x)\right) = \frac{i_{\mathrm{cell}}}{\alpha} \times \frac{k}{\alpha} t_{\mathrm{ele,FLAT}} \Big/ t_{\mathrm{ele}}\left(\xi(x)\right). \tag{3.49}$$

Hence, the Joule heating in the electrolyte in the mesoscale-modified cell $Q_{\mathrm{ohm,ele,MESO}}$ can be written as

$$Q_{\mathrm{ohm,ele,MESO}} = \frac{i_{\mathrm{O}^{2-},\mathrm{ele}}\left(\xi(x)\right)^2}{\sigma_{\mathrm{O}^{2-},\mathrm{YSZ}}} t_{\mathrm{ele}}\left(\xi(x)\right) d\xi(x) = \frac{\left(\frac{i_{\mathrm{cell}}}{\alpha} \times \frac{k}{\alpha} t_{\mathrm{ele,FLAT}}\right)^2}{\sigma_{\mathrm{O}^{2-},\mathrm{YSZ}} t_{\mathrm{ele}}\left(\xi(x)\right)} d\xi(x). \tag{3.50}$$

If the electrolyte thickness is uniform and constant at $(k/\alpha)t_{\mathrm{ele,FLAT}}$, Eq. (3.50) can be calculated as

$$Q_{\mathrm{ohm,ele,MESO}} = \frac{(i_{\mathrm{cell}}/\alpha)^2}{\sigma_{\mathrm{O}^{2-},\mathrm{YSZ}} / \frac{k}{\alpha} t_{\mathrm{ele,FLAT}}} \alpha L. \tag{3.51}$$

Table 3.4 Average values of the structural geometries of mesoscale-modified cell.

$\theta_{\mathrm{A–E}}$ / °	$\theta_{\mathrm{C–E}}$ / °	$w_{\mathrm{A–E}}$ / μm	$w_{\mathrm{C–E}}$ / μm	Δ / μm
109.3	55.3	102.4	145.5	8.4

By using the average values of the structural geometries of the mesoscale-modified cell measured using the open-source image processing program "ImageJ" (*68*), which are summarized in **Table 3.4**, the interfacial area enlargement and thickness inhomogeneity effects are calculated to be 8.21 and 17.5 %, respectively (*cf.* the Joule heating in the mesoscale-modified cell was approximately calculated by a Riemann sum of Eq. (3.50) over the closed interval $\left[-\frac{L}{2}, \frac{L}{2}\right]$ using 202000 uniform subdivisions.). According to Eq. (3.41), therefore, the Joule heating in the electrolyte is reduced by 24.3 %, which is close to that obtained from the numerical simulation (22.2 %). Note that the relative decreases in ohmic

resistance (loss) estimated by taking account of the structures of the mesoscale-modified cells prepared in Chapter 2 are very close to the measured values with a relative error of no more than 5.5 %.

3.4.3.3 Charge-transfer current density

As discussed in Section 3.4.2, the relative decreases in the activation overpotentials (4.81 % in the anode and 2.29 % in the cathode) are smaller than each of those estimated under the assumption that the electrochemical reactions uniformly occur in the effective reaction region (6.32–10.5 % in the anode 6.88–7.52 % in the cathode). This implies that the electrochemical reactions nonuniformly occur such that the relative decreases in the activation overpotential cannot be expressed by Eq. (3.40).

Considering that the total amount of the electrochemical reaction is the same for both cells ($i_{\mathrm{ct}}\,dxdy = \text{constant}$) and that the form of $x\sinh^{-1}(x)$ under the integral sign of the approximated activation energy loss (Eq. (3.35)) is a function that is strictly increasing and concave up for all positive real numbers, the following inequalities can be established:

$$Q_{\mathrm{act,FLAT}} \cong \frac{RT}{\beta F}\sinh^{-1}\frac{i_{\mathrm{ct,FLAT}}}{2i_0}\, i_{\mathrm{ct,FLAT}}dxdy \geq \frac{RT}{\beta F}\sinh^{-1}\frac{i_{\mathrm{cell}}}{2i_0 t_{\mathrm{eff}}}\, i_{\mathrm{cell}}L \tag{3.52}$$

$$Q_{\mathrm{act,MESO}} \cong \frac{RT}{\beta F}\sinh^{-1}\frac{i_{\mathrm{ct,MESO}}}{2i_0}\, i_{\mathrm{ct,MESO}}dxdy \geq \frac{RT}{\beta F}\sinh^{-1}\frac{i_{\mathrm{cell}}}{2i_0\alpha t_{\mathrm{eff}}}\, i_{\mathrm{cell}}L. \tag{3.53}$$

Details of the above inequalities are provided in Appendix B. Note that the ratio of the activation energy loss obtained from the simulation to that estimated under the assumption that the electrochemical reaction uniformly occurs increases greater when the nonuniformity of the distribution of the charge-transfer current density becomes stronger. Thus, the following inequality can be obtained:

$$\frac{Q_{\mathrm{act,MESO}}}{\frac{RT}{\beta F}\sinh^{-1}\frac{i_{\mathrm{cell}}}{2i_0\alpha t_{\mathrm{eff}}}\, i_{\mathrm{cell}}L} > \frac{Q_{\mathrm{act,FLAT}}}{\frac{RT}{\beta F}\sinh^{-1}\frac{i_{\mathrm{cell}}}{2i_0 t_{\mathrm{eff}}}\, i_{\mathrm{cell}}L}. \tag{3.54}$$

Therefore,

$$RD_{\mathrm{act}} = 1 - \frac{Q_{\mathrm{act,MESO}}}{Q_{\mathrm{act,FLAT}}} < 1 - \frac{\sinh^{-1}\left(\frac{i_{\mathrm{cell}}}{2i_0\alpha t_{\mathrm{eff}}}\right)}{\sinh^{-1}\left(\frac{i_{\mathrm{cell}}}{2i_0 t_{\mathrm{eff}}}\right)}. \tag{3.55}$$

From the above results, it can be concluded that the decreases in ohmic and activation overpotentials are respectively larger and smaller compared with those estimated under the assumptions that the ionic and charge-transfer current densities are uniformly distributed in a cell; this is mainly due to the nonuniform distributions of all physicochemical quantities that contribute to the electrochemical reactions in the mesoscale-modified cell.

3.4.4. Effect of distribution nonuniformity on cell performance

In this section, the effect of the mesostructural modification in terms of the electrochemical performance of anode-supported SOFCs under various current density conditions is discussed. **Figure 3.8** shows the decreases in average overpotentials of the mesoscale-modified cell relative to the flat cell as a function of the current density. Note that a relative increase is represented as the minus sign. The relative decrease in the total ohmic loss RD_{ohm} becomes larger with increasing current density. As described in Eq. (3.49), the ionic current density in the electrolyte in the mesoscale-modified cell is inversely proportional to the electrolyte thickness such that the local ionic current density becomes higher in regions where the local electrolyte thickness is smaller, and lower in regions where it is larger. This is more prominent under a high current density condition, resulting in stronger nonuniformity of the local Joule heating. Consequently, the Joule heating in the electrolyte in the mesoscale-modified cell is more reduced than that in the flat cell under high current density conditions, and thereby a significantly large relative decrease in the ohmic loss. Contrary to the relative decrease in the ohmic loss, those in the activation overpotentials in the electrodes RD_{act} become smaller with increasing current density. This is because the right-hand side of the inequality in Eq. (3.55) is a monotonically decreasing function with respect to the current density, resulting in only a slight difference between

the activation energy losses in both cells at high current density. On the other hand, the relative increase in the concentration overpotential in the anode $RD_{\mathrm{con,act}}$ is almost constant because it is mainly affected by the increase in the average anode thickness, as mentioned in Section 3.4.2. The relative decrease in the total cell overpotential RD_{total} becomes larger with increasing current density, whose trend is the same as that of the total ohmic loss. This is because the decrease in the sum of the ohmic losses in each cell component accounts for most of the total decrease in cell overpotential (*e.g.*, the ratio of the decrease in the total ohmic loss with respect to the total decrease at 1.0 A cm^{-2} at 700 °C is 91.8 %). From these results, it can be concluded that the effect of the mesostructural modification in terms of the improvement in the electrochemical performance of anode-supported SOFCs is more remarkable under high current density conditions.

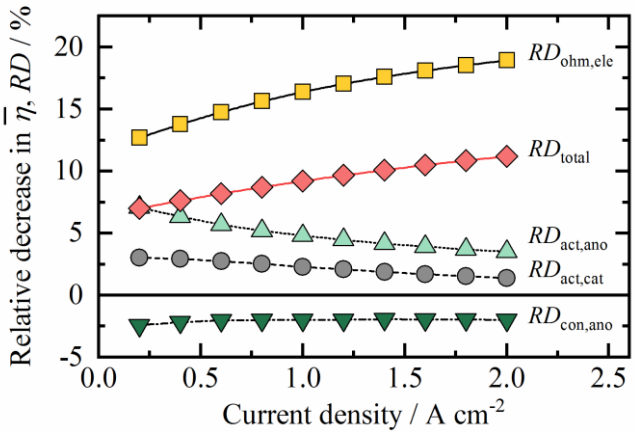

Fig. 3.8 Decreases in overpotential components of mesoscale-modified cell relative to flat cell at 700 °C.

3.5 Summary

The mechanism of improvement in the electrochemical performance of the anode-supported SOFC by the mesostructural modification of the electrode–electrolyte interface was clarified. After preparing two types of anode-supported SOFC having different electrode–electrolyte interfacial areas, the 2D numerical model where the cell structures in a wide range of length scales were implemented was developed. It was verified that the simulation results well reproduced the experimental ones in terms of the electrochemical characteristics, *i.e.*, the electrochemical performance of the mesoscale-modified cell was improved compared with that of the flat cell. It was found that the structural features in the mesoscale-modified cell, such as interfacial area enlargement and thickness inhomogeneity, caused nonuniform distributions of the physicochemical quantities that contribute to the electrochemical reactions. Consequently, the decreases in ohmic and activation overpotentials of the mesoscale-modified cell relative to the flat cell were respectively larger and smaller than those estimated under the assumptions that the ionic and charge-transfer current densities in a cell have uniform distributions. Moreover, the ionic current density distribution had strong nonuniformity under high current density conditions, leading to a significantly large relative decrease in the ohmic loss. On the other hand, the concentration overpotential in the anode was slightly increased, which was mainly caused by the fact that the average anode thickness was increased by attaching the anode ridge structures. However, it rarely hindered the improvement in cell performance under a high hydrogen partial pressure condition set in this work. Furthermore, the relative decrease in the cell overpotential was larger at high current density, indicating that the effect of the mesostructural modification in terms of the improvement in the electrochemical performance of anode-supported SOFCs is more prominent under high current density conditions.

4

Quantitative evaluation of mesostructural modification effect on the electrochemical performance of anode-supported SOFCs under various hydrogen partial pressures

4.1 Introduction

The mesostructural modification for anode-supported SOFCs is highly advantageous in realizing the low-temperature operation, as discussed in the previous two chapters. However, there is an obvious shortcoming: the cell performance is less improved under a low H_2 partial pressure condition, as discussed in Chapter 2. That is, a decrease in cell resistance due to the mesostructural modification became smaller with decreasing H_2 partial pressure. Specifically, when the current density was 0.3 A cm^{-2}, the total resistance in a mesoscale-modified cell was reduced by 27 % under 80 % H_2, whereas 14 % under 20 % H_2. According to numerical analysis, the resistance component attributed to gas diffusion in the anode in a mesoscale-modified cell whose average anode thickness was increased by about 1.9 % compared with that of a flat cell was only increased by 2.0 % at the current density of 1.0 A cm^{-2}, as discussed in Chapter 3. Thus, it can be presumed that the increase in gas diffusion resistance is not the only factor that causes the effect of the mesostructural modification on the cell performance to be smaller under a low H_2 partial pressure condition.

In this chapter, therefore, the effect of the mesostructural modification of the electrode–electrolyte interface on the electrochemical performance of anode-supported SOFCs is quantitatively investigated under various H_2 partial pressures. Additionally, to clarify which resistance component mainly causes the effect to fade away under a low H_2 partial pressure, the distribution of relaxation times (DRT) method, one of the most powerful tools for evaluating the electrochemical performance of anode-supported SOFCs (*47*, *50*, *52*, *55*), is employed. First, two types of anode-supported SOFCs having different interfacial areas, a flat cell and a mesoscale-modified cell, are prepared. Thereafter, the cross sections of the cells are observed by scanning electron microscopy (SEM) and their electrochemical performance is characterized by both current–voltage (*i*–*V*) measurement and electrochemical impedance spectroscopy (EIS). The EIS data of the cells are analyzed by the DRT method, which is followed by the complex nonlinear least-squares (CNLS) fitting. Finally, the changes in resistance components strongly affected by a change in H_2 partial pressure are quantitatively evaluated to find obstacles to improvement in cell performance.

4.2 Experimental

4.2.1 Anode paste preparation

A highly viscoelastic NiO–yttria-stabilized zirconia (YSZ) anode paste used in microextrusion printing was made with NiO powder (Sumitomo Metal Mining Co., Ltd., Japan, average particle size = *ca*. 0.4 μm), $(Y_2O_3)_{0.08}(ZrO_2)_{0.92}$ powder (TZ-8Y, Tosoh Corp., Japan, crystallite size = 21 nm), and a homemade ink vehicle composed of 96 wt% terpineol (mixed isomers) (Nacalai Tesque, Inc., Japan) and 4 wt% ethylcellulose (Nacalai Tesque, Inc., Japan). A mixture of 60 wt% NiO–YSZ mixed powder (NiO:YSZ = 66:34 wt%) and a 40 wt% homemade ink vehicle was ball-milled with zirconia balls (ϕ 10.0 mm) at 500 rpm for 12 h to obtain a homogeneous anode paste. By characterizing the rheological properties of the anode paste using a rotational double coaxial cylinder viscometer (Viscolead ADV,

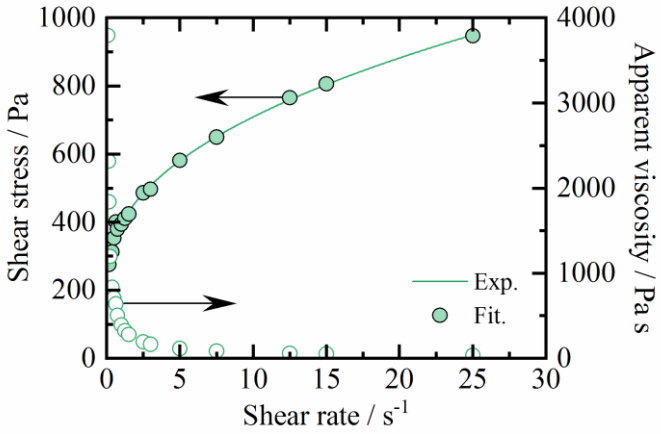

Fig. 4.1 Shear stress and apparent viscosity curves of anode paste as a function of shear rate.

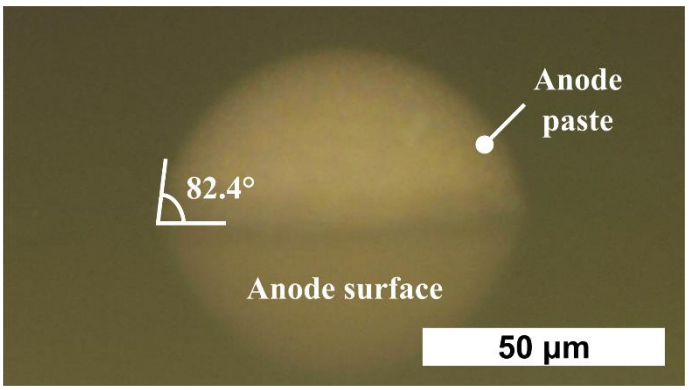

Fig. 4.2 Contact angle of NiO–YSZ anode paste on NiO–YSZ anode disk.

Fungilab, S.A., Spain), it was confirmed that the anode paste is a yield pseudoplastic fluid that follows the Herschel–Bulkley fluid model (*69*); its yield shear stress, consistency, and flow index were evaluated as 210.58 Pa, 185.31 Pa $s^{0.43}$, and 0.43, respectively, at 25 °C (see **Fig. 4.1**). Also, the contact angle between a NiO–YSZ anode disk whose details are described hereinafter and the NiO–YSZ anode paste was measured to be about 82.4° at room temperature by the half-angle method, as shown in **Fig. 4.2**. These physical properties are very close to those of the NiO–YSZ anode paste used in Chapter 2. Thus, the NiO–YSZ anode paste prepared in this work is available for the formation of anode ridge structures by microextrusion printing.

4.2.2 Cell fabrication

Two types of anode-supported SOFC having different interfacial areas, a flat cell (FLAT) and a mesoscale-modified cell (MESO), were fabricated. First, a flat NiO–YSZ anode disk was prepared by tape casting. The composition of the anode slurry used in this chapter is summarized in **Table 4.1**. NiO (FUJIFILM Wako Pure Chemical Corp., Japan, average particle size = *ca*. 1–2 μm) and YSZ powders (NiO:YSZ = 60:40 wt%) with the addition of 10 wt% crosslinked poly(methyl methacrylate) (PMMA) (SSX-108, Sekisui Plastic Co., Ltd., Japan, average particle size = 8 μm) as a pore former were mixed by planetary ball milling in isopropanol with zirconia balls (ϕ 4.0 mm) at 300 rpm for 3 h. After the isopropanol was completely evaporated, the resultant powder was sieved with a 53 μm mesh. The anode composite powder, organic solvent, dispersant were firstly mixed with zirconia balls (ϕ 4.0 mm) at 200 rpm for 24 h. Subsequently, the binder and plasticizers were added and then mixed for another 24 h to obtain a homogeneous anode slurry. After degassing the anode slurry under a pressure of 0.20 atm for 10 min during magnetic stirring, it was cast on a glass plate at a casting speed of 10 mm s^{-1} and a doctor blade gap of 2.0 mm using a commercial tape casting machine (Imoto Machinery Co., Ltd., Japan). The cast slurry was fully dried at 20 °C and 80 % relative humidity using a temperature and humidity chamber (Yamato Scientific Co., Ltd., Japan) for 24 h. A green sheet was cut into a disk shape with a diameter of 30 mm, which was followed by presintering at 1150 °C for 2 h.

Table 4.1 Composition of anode slurry for tape casting in weight ratio.

	Material	Weight ratio / %
Powder	NiO	28.6
	$(Y_2O_3)_{0.08}(ZrO_2)_{0.92}$	19.1
	PMMA	5.30
Solvent	Ethanol	33.8
Dispersant	Triton X-100	1.06
Binder	PVB	6.36
Plasticizer	PEG 400	2.89
	Glycerin	2.89

By microextrusion printing, anode ridge structures were formed on the flat anode disk. A nozzle tip with an inner diameter of 150 μm (Nordson Corp., USA) was attached to the end of a gas-tight syringe filled with the anode paste, and then the syringe was fixed vertically to the syringe pump. The anode disk was placed onto the *z*-axis stage to control the height between its surface and the nozzle tip. The anode paste was printed in a line shape on the surface of the anode disk at a stage speed of 20 mm s^{-1}, an applied flow rate of 10 μL min^{-1}, and a printing interval of 320 μm. After returning the *x*–*y*-axis stages to the origin and moving the *z*-axis stage downward through 60 μm, the printing of the anode paste was conducted once again onto the as-printed anode paste under the same printing condition. Using a 3D surface measurement system (VR-3100, Keyence Corp., Japan), it was confirmed that the width and height of the printed paste before drying were 156.4 ± 5.5 and 102.6 ± 1.1 μm, respectively, and those after drying were 155.9 ± 4.9 and 49.6 ± 1.5 μm, respectively. Note that the measured width of the printed paste before drying is very close to the predicted value (158.3 μm) calculated by the line width prediction model proposed in Chapter 2.

An anode functional layer (AFL), a YSZ electrolyte, and a gadolinium-doped ceria (GDC) barrier layer were prepared by slurry spin coating (*7*, *100*, *101*). NiO–YSZ, YSZ, and $Gd_{0.1}Ce_{0.9}O_{1.95}$ (GDC-

10(AU), Shin-Etsu Astech Co., Ltd., Japan) powders were added to the homemade ink vehicle with solid loadings of 60, 25, and 50 wt%, respectively, and then mixed by planetary ball milling at 500 rpm for 12 h to form homogeneous pastes. After painting an appropriate amount of the AFL paste on the surface of the anode disk, it was spun at 8000 rpm for 90 s and then dried at 200 °C on a hot plate. Note that the angular speed of spinning was gradually elevated at an angular acceleration of 100 rpm s^{-1} to uniformly spread the highly viscoelastic pastes throughout the disk surface. The YSZ and GDC pastes were spin-coated with the same method as that for the AFL paste. The NiO–YSZ anode and YSZ electrolyte were cosintered at 1400 °C for 5 h, and the GDC interlayer was sintered at 1250 °C for 2 h. Finally, a lanthanum strontium cobalt ferrite (LSCF)–GDC paste composed of 70 wt% $La_{0.6}Sr_{0.4}Co_{0.2}Fe_{0.8}O_{3-\delta}$ (LSCF-6428-N, Kceracell Co., Ltd., Korea)–GDC mixture powder and a 30 wt% commercial ink vehicle (VEH, Nexceris, LLC, USA) was screen-printed on the GDC surface with a mask of 60 μm thickness, which was followed by sintering at 950 °C for 5 h. The apparent geometrical cathode area was about 0.785 cm^2.

4.2.3 Performance evaluation and structure observation

The electrochemical performance of the cells was evaluated at an operating temperature of 600 °C. NiO in the anode was reduced to Ni in a reducing atmosphere at 800 °C for 2 h. Thereafter, mixture gases of *x* % H_2–20 % H_2O–(80-*x*) % N_2 (*x* = 5, 10, 20, 40, 80) and 21 % O_2–79 % N_2 were supplied to the anode and cathode, respectively. The total flow rate was 100 sccm on both electrodes. The *i–V* characteristics and EIS of the cells were measured using a Solartron 1455A frequency response analyzer and a Solartron 1470E potentio/galvanostat electrochemical interface (Solartron Analytical, UK). The EIS measurement was performed in the frequency range from 0.1 MHz to 0.1 Hz with an AC amplitude of 10 mA under open-circuit voltage (OCV).

The EIS data of each cell were analyzed by the DRT method using the commercial impedance analysis support software “Z-Assist” (Toyo Corp., Japan) after removing the inductance components included in a high-frequency region (*49*, *50*). In this software, the FTIKREG program (*102*) is used in

calculating distribution functions; when an impedance in a circuit where a number of parallel resistor–capacitor (RC) circuits are connected in series satisfies the Kramers–Kronig relations (*103*), either its real or imaginary part is solved by Tikhonov regularization (*104*) using a Fredholm equation of the first kind with the Kernel function. Details of the DRT analysis can be found elsewhere (*46*, *47*, *54*, *105*). Thereafter, the CNLS fitting for the EIS data of the tested cells was carried out with the parameters obtained from the DRT analysis using the software "ZView" (Scribner Associates Inc., USA).

After the electrochemical testing, the cross sections of the tested samples were observed by SEM. Each cell was impregnated with epoxy resin (EpoFix, Struers, Denmark) under a vacuum condition, which was followed by cutting and then polishing to observe their cross sections by SEM (Miniscope TM3000, Hitachi High-Tech Corp., Japan).

4.3 Results and discussion

4.3.1 Cell structure

The cross-sectional SEM images of the cells after the electrochemical testing are shown in **Fig. 4.3**. Two layers with obviously different microstructures in the Ni–YSZ anode are observed in both cells; the denser of them is the AFL and the other is the anode disk (anode support layer, ASL) with a thickness of about 450 μm. This microstructural difference results from the use of the pore former during the ASL preparation process, as mentioned in Section 4.2.2. Dense YSZ thin membranes with an average thickness of about 4.8 μm are successfully formed without any delamination from either the Ni–YSZ AFL or the GDC interlayer not only in the flat cell but also in the mesoscale-modified cell. In particular, the dense electrolyte in the mesoscale-modified cell is achieved owing to a perfect match of the thermal shrinkage ratios between the anode ridge structures and the AFL by using the same starting material when preparing them. Also, both the YSZ electrolyte and GDC interlayer in the mesoscale-modified cell have a relative homogeneous thickness because the highly viscoelastic terpineol-based pastes were used in the spin coating process (*7*, *100*, *101*), unlike those in mesoscale-modified cells prepared by using ethanol-based suspension, as described in Chapters 2 and 3. The average width, average height, and average arc length of the anode ridge structures are 146.8, 18.2, and 163.8 μm, respectively, and the average interval between two adjacent ridge structures is about

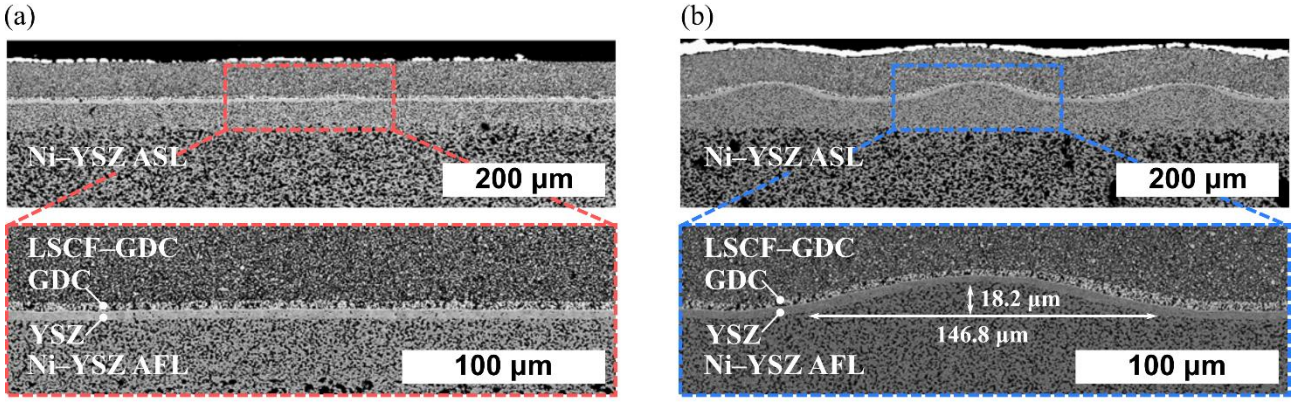

Fig. 4.3 Cross-sectional SEM images of (a) flat and (b) mesoscale-modified cells after electrochemical testing.

250.5 μm. From these values, the electrode–electrolyte interfacial area in the mesoscale-modified cell is extended by about 6.8 % compared with that in the flat cell, leading to an increase in the area of the electrochemically active regions in both electrodes. Note that, however, the aspect ratio of the anode ridge structure, the ratio of its height to its width, is drastically reduced compared with that after drying. This is mainly caused by a simultaneous increase in the width and decrease in the height due to the attachment of the AFL with a thickness of 33.8 μm on the surface of the anode disk by spin coating. Moreover, the average thickness of the Ni–YSZ AFL including the anode ridge structures in the mesoscale-modified cell is 53.2 μm, which is about 57 % larger than that in the flat cell. Owing to the increase in the AFL thickness, it is expected that gas diffusion resistance in the anode in the mesoscale-modified cell will be increased compared with that in the flat cell. Note that the brightest layer on top of the LSCF–GDC cathode in the SEM images of both cells is the silver current collector.

4.3.2 Cell performance

Figure 4.4 shows the *i–V* and current–power (*i–P*) curves of the cells at 600 °C with different H_2 partial pressures p_{H_2}. Note that the current density is defined as the current normalized with the apparent geometrical cathode area for each cell. As summarized in **Table 4.2**, the near-theoretical OCVs are achieved in both cells, indicating that the thin but dense YSZ membranes are of very high quality and gas sealing is sufficiently good during the electrochemical testing. As can be seen in **Fig. 4.4(a)**, the electrochemical performance of the mesoscale-modified cell is remarkably improved compared with that of the flat cell under high p_{H_2}. For instance, when the current density is 0.3 A cm^{-2} at 600 °C with 80 % H_2, the mesoscale-modified cell exhibits a terminal voltage of 0.79 V, which is 1.15 times higher than that of the flat cell. This results from the fact that cell overpotential is reduced by the mesostructural modification of the electrode–electrolyte interface (*37*, *40*, *101*). On the other hand, it is found that the effect of the mesostructural modification of the electrode–electrolyte interface fades away under low p_{H_2}, as shown in **Fig. 4.4(b)**. Specifically, the cell performance in a relatively low current density region, where the activation overpotential is predominant (*106*, *107*), has almost

no difference between both cells under the 5 % H_2 condition. From the fact that a decrease in cathodic activation overpotential due to the mesostructural modification is always the same regardless of p_{H_2}, it can be presumed that a decrease in anodic activation overpotential becomes smaller with decreasing p_{H_2}. In a current density region of over 0.2 A cm^{-2} under 5 % H_2, the mesoscale-modified cell rather shows lower cell performance than that of the flat cell. This is because the mesoscale-modified cell has a higher concentration overpotential than the flat cell owing to the increase in the average anode thickness. Thus, the increase in cell overpotential with decreasing p_{H_2} in the mesoscale-modified cell is greater than that in the flat cell. This brings a disadvantage in the improvement in the electrochemical performance of anode-supported SOFCs by the mesostructural modification of the electrode–electrolyte interface, particularly under a low p_{H_2} (high fuel utilization) condition.

Table 4.2 Theoretical and measured OCVs at 600 °C with different H_2 partial pressures.

H_2 partial pressure / atm	Theoretical value / V	FLAT / V	MESO / V
0.80	1.057	1.049	1.044
0.05	0.952	0.948	0.950

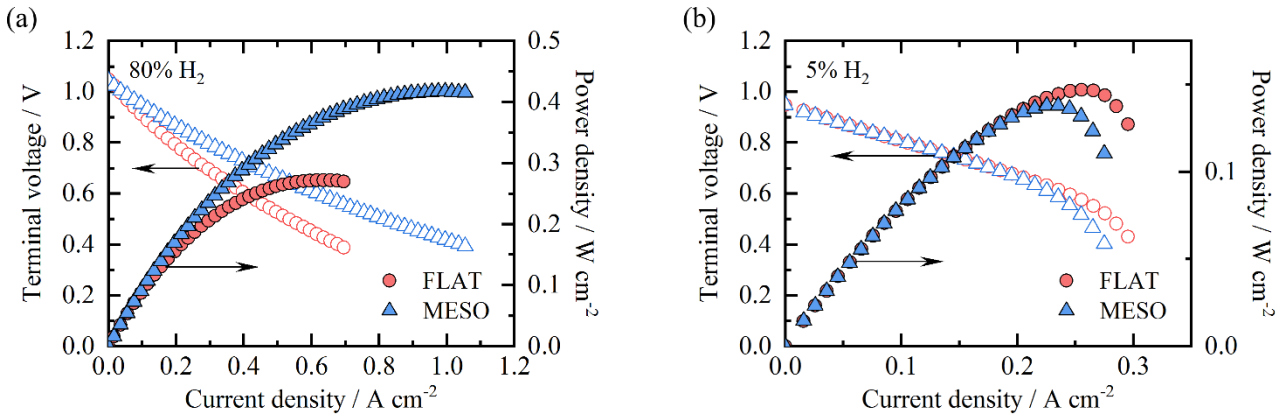

Fig. 4.4 *i–V* and *i–P* curves of tested cells at 600 °C with (a) 80 % H_2 and (b) 5 % H_2.

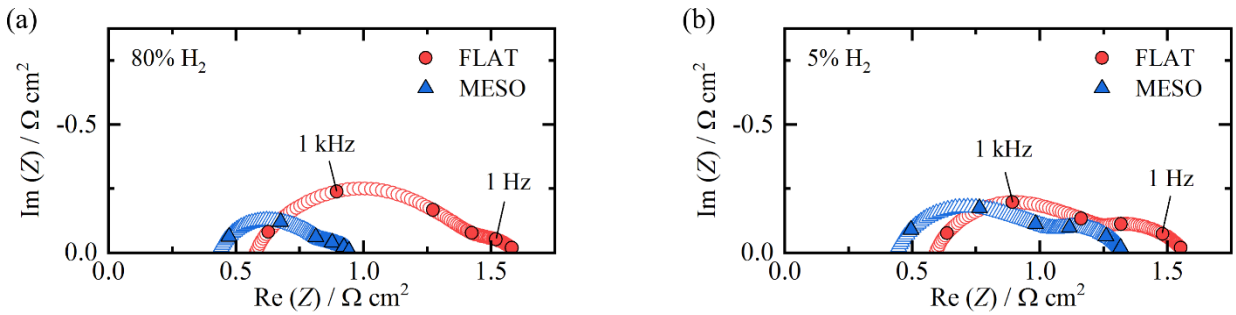

Fig. 4.5 Nyquist plots of EIS of the cells at 600 °C with (a) 80 % H_2 and (b) 5 % H_2 under OCV condition.

Figure 4.5 shows Nyquist plots of EIS obtained under the OCV condition at 600 °C with 80 % and 5 % H_2. It can be seen that the cell resistance is reduced by mesostructural modifying the electrode–electrolyte interface. For instance, the total cell resistance under the 80% H_2 condition is *ca.* 0.94 Ω cm^2 in the mesoscale-modified cell, which is significantly lower than *ca.* 1.6 Ω cm^2 in the flat cell. This is due to decreases in ohmic and activation resistances, whose details are described in the literature (*40*, *71*, *101*). On the other hand, the effect of the mesostructural modification in terms of the improvement in cell performance is smaller under lower p_{H_2}. Specifically, a relative decrease in the total cell resistance is 40 % under 80 % H_2, whereas 14 % under 5 % H_2. As p_{H_2} decreases, it is observed that the diameters of the impedance arcs at intermediate and low frequencies in the mesoscale-modified cell are both increased, whereas those in the flat cell are decreased and increased, respectively. This suggests that the activation resistance in both cells have the opposite dependence on p_{H_2}, while the gas diffusion resistances have the same one. Consequently, the cell resistance is less reduced under a low p_{H_2}.

4.3.3 DRT analysis

To quantitatively understand which resistance component mainly hinders the improvement in cell performance due to the mesostructural modification under a low p_{H_2}, the EIS data of the cells were analyzed using the DRT method. DRT spectra obtained by analyzing the EIS data are shown in **Fig.**

4.6. There are six different peaks in each DRT spectrum, two of which are notably changed with p_{H_2}. This indicates that the two peaks are possessed of a strong dependence on p_{H_2}. Referring to the results obtained from the literature (*47*, *50*, *54*, *105*, *108*, *109*), the physicochemical origins of each peak can be characterized and are summarized in **Table 4.3**. For the flat cell, as p_{H_2} decreases, the area of a curve with P_{a2} as a peak is reduced, whereas that with P_{dif} as a peak is increased. This indicates that a resistance component attributed to the O^{2-} conduction and charge transfer processes in the anode becomes smaller, whereas that attributed to the gas diffusion process becomes larger with decreasing p_{H_2}. This trend is the same as that in the literature (*108*), where the electrochemical testing of an anode-supported SOFC with the Ni–YSZ/YSZ/GDC/LSCF structure was conducted under several operating conditions at 800 °C with 20 % humidified H_2. On the other hand, for the mesoscale-modified cell, the areas of curves with P_{a2} and P_{dif} as peaks are both increased with decreasing p_{H_2}. This indicates that resistance components attributed to the O^{2-} conduction and charge transfer and gas diffusion processes in the anode are larger under lower p_{H_2}. That is, only the dependence of the O^{2-} conduction and charge transfer processes in the anode on p_{H_2} between the two cells reveals an outstanding difference. Note that, however, mechanisms regarding this issue are still unresolved and currently under investigation.

Table 4.3 Physicochemical origins of each DRT peak.

Peak	Frequency / Hz	Physicochemical origin
P_{c1}	4.0×10^{4}–5.0×10^{4}	Oxide ionic conduction process in the LSCF bulk
P_{a1}	7.1×10^{3}–8.9×10^{3}	Oxide ionic conduction and charge transfer processes in the anode
P_{a2}	6.3×10^{2}–2.0×10^{3}	
P_{a3}	8.9×10^{1}–2.8×10^{2}	
P_{c2}	2.2×10^{1}–5.6×10^{1}	Oxygen adsorption/desorption process on the LSCF surface
P_{dif}	6.3×10^{0}–2.2×10^{1}	Gas diffusion process in the anode

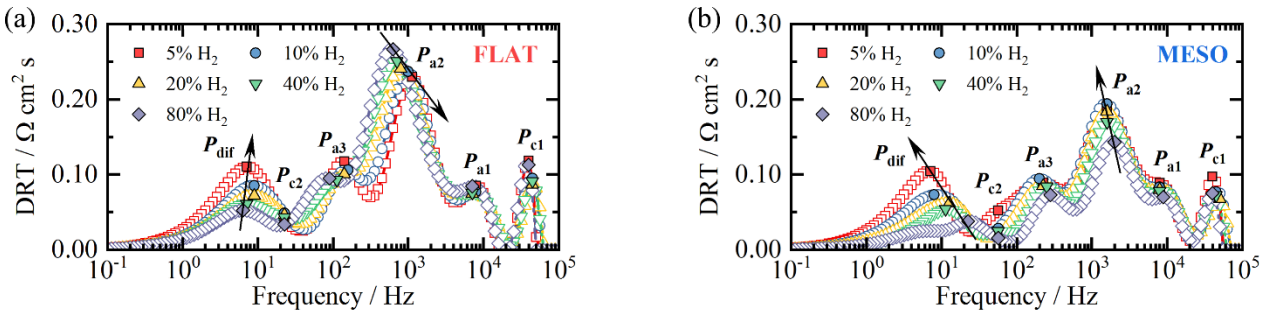

Fig. 4.6 DRT spectra of (a) flat and (b) mesoscale-modified cells at 600 °C with different H_2 partial pressures.

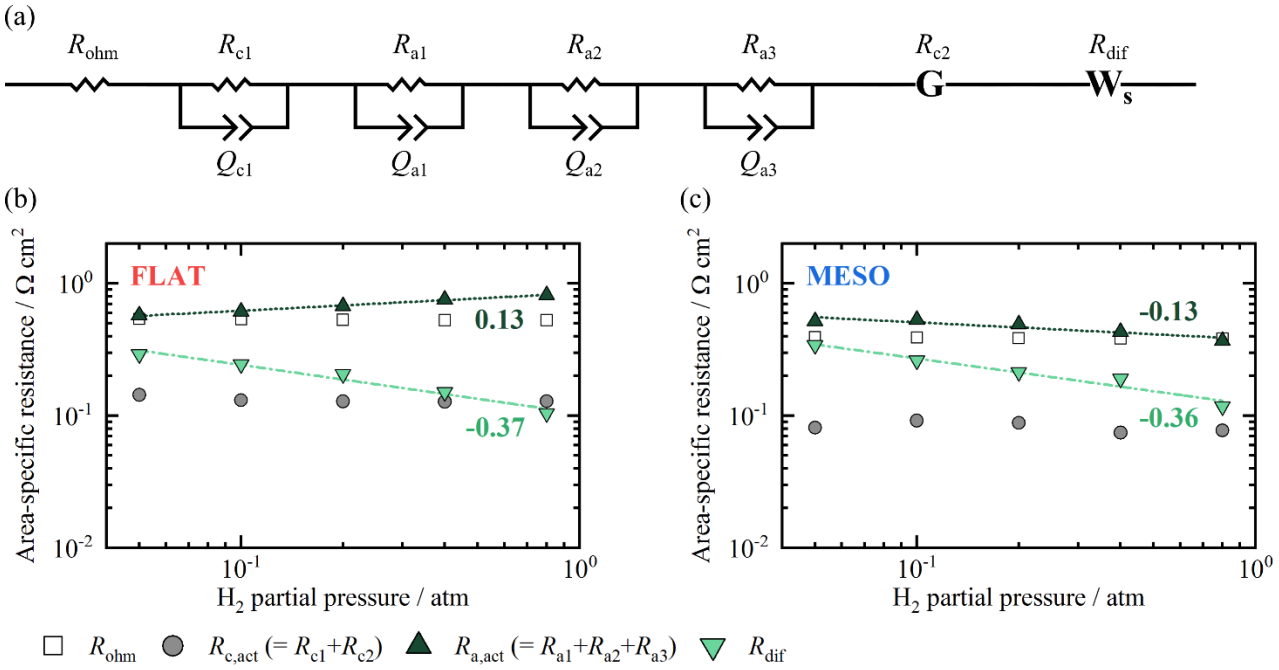

Fig. 4.7 (a) Equivalent circuit model for fitting analysis and area-specific resistances of (b) flat and (c) mesoscale-modified cells at 600 °C as a function of hydrogen partial pressure.

4.3.4 Quantitative evaluation of area-specific resistances

To quantitatively evaluate each resistance component in the tested cells, an equivalent circuit model (**Fig. 4.7(a)**), where a resistor element, four parallel *RQ* elements, a Gerischer element, and a generalized finite-length Warburg element are connected in series is introduced based on the DRT analysis. The Gerischer element $Z_G(\omega)$ (*96*, *110*, *111*) and the generalized finite-length Warburg

element $Z_{\mathrm{W}}(\omega)$ (*112*), which respectively correspond to the O_2 adsorption/desorption process on the LSCF surface and gas diffusion process in the anode, can be expressed as

$$Z_{\mathrm{G}}(\omega) = \frac{R_{\mathrm{G}}}{1+j\omega t} \tag{4.1}$$

$$Z_{\mathrm{W}}(\omega) = R_{\mathrm{W}} \frac{\tanh(j\omega \frac{l_{\mathrm{dif}}^2}{D_i^{\mathrm{eff}}})^n}{(j\omega \frac{l_{\mathrm{dif}}^2}{D_i^{\mathrm{eff}}})^n}. \tag{4.2}$$

Here, ω and j represent the frequency and imaginary unit, respectively. Also, R_{G} and t in Eq. (4.1) are respectively the characteristic resistance and time constant, which are related to the physicochemical properties of mixed ion-electron conductors such as Co-doped perovskite oxides (*96*). Moreover, R_{W}, l_{dif}, D_i^{eff}, and n in Eq. (4.2) are the diffusion resistance, effective diffusion length, effective diffusion coefficient of gas species i, and exponent of the generalized finite-length Warburg impedance, respectively.

The area-specific resistance components (R_{ohm}, $R_{\mathrm{c,act}}$, $R_{\mathrm{a,act}}$, R_{dif}) obtained by separating the total resistances in the flat and mesoscale-modified cells as a function of H_2 partial pressure are shown in **Figs. 4.7(b)** and **4.7(c)**, respectively. Note that the cathodic $R_{\mathrm{c,act}}$ and anodic activation resistances $R_{\mathrm{a,act}}$ are represented as the sum of the resistance components attributed to the electrochemical react-

Table 4.4 Decreases in each resistance component under OCV condition.

H_2 partial pressure / atm	ΔR_{ohm} / Ω cm^2	$\Delta R_{\mathrm{c,act}}$ / Ω cm^2	$\Delta R_{\mathrm{a,act}}$ / Ω cm^2	ΔR_{dif} / Ω cm^2	$\Delta R_{\mathrm{total}}$ / Ω cm^2
0.80	0.15 ± 0.0011	0.050 ± 0.0089	0.45	-0.025 ± 0.017	0.63
0.40			0.32		0.48
0.20			0.19		0.37
0.10			0.081		0.25
0.05			0.055		0.22

ions in each electrode. The ohmic R_{ohm} and cathodic activation resistances $R_{c,act}$ in both cells are constant regardless of p_{H_2}. In contrast, the anodic activation $R_{a,act}$ and gas diffusion resistances R_{dif} are gradually changed with p_{H_2}. These trends correspond to those revealed from the DRT analysis (see **Fig. 4.6**).

Table 4.4 summarizes the absolute decreases in each resistance component $\Delta R\ (= R_{FLAT} - R_{MESO})$ calculated as the difference between the resistances in the flat R_{FLAT} and mesoscale-modified cells R_{MESO}. Note that the minus sign represents that a resistance component in the mesoscale-modified cell is increased compared with that in the flat cell. R_{ohm} in the mesoscale-modified cell is 0.39 Ω cm^2, which is reduced by approximately 27 % compared with that in the flat cell (0.53 Ω cm^2). The decrease in R_{ohm} is because the local current density flowing inside the electrolyte is lower owing to the mesostructural modification of the electrode–electrolyte interface, leading to a decrease in Joule heating. Moreover, its relative decrease (*ca.* 27 %) coincides with that obtained from an anode-supported SOFC where the electrode–electrolyte interfacial area was extended by about 7.0 % compared with that in a flat cell (*ca*. 26–28 %), as mentioned in Chapter 2. $R_{c,act}$ in the mesoscale-modified cell (0.083 Ω cm^2) is about 37 % lower than that in the flat cell (0.13 Ω cm^2). This decrease is due to the fact that the electrochemical reaction amount per unit reaction site in the LSCF–GDC cathode is reduced by extending the electrode–electrolyte interfacial area.

Similar to $R_{c,act}$, $R_{a,act}$ is also reduced owing to a decrease in the electrochemical reaction amount per unit reaction site in the Ni–YSZ anode. Since $R_{a,act}$ has the opposite dependence on p_{H_2} for both cells, however, its decrease is strongly affected by p_{H_2}. $R_{a,act}$ in the flat cell (0.58–0.82 Ω cm^2) becomes smaller with decreasing p_{H_2} and is proportional to p_{H_2} to the 0.13 power, as shown in **Fig. 4.7(b)**. This trend is the same as that in the previous work (*108*) where an anodic activation resistance was found to be proportional to the one-tenth power of H_2 partial pressure. In contrast, $R_{a,act}$ in the mesoscale-modified cell (0.37–0.52 Ω cm^2) is proportional to p_{H_2} to the -0.13 power, *i.e.*, it becomes larger with decreasing p_{H_2}, as shown in **Fig. 4.7(c)**. Accordingly, compared with $R_{a,act}$ in

the flat cell, that in the mesoscale-modified cell is reduced by about 10–55 %, which becomes remarkably smaller under a low p_{H_2}.

Unlike the other resistance components reduced by the mesostructural modification of the electrode–electrolyte interface, R_{dif} is increased by about 13.2 % in the mesoscale-modified cell (0.12–0.34 Ω cm^2) in comparison with that in the flat cell (0.10–0.29 Ω cm^2). R_{dif} in the flat and mesoscale-modified cells are respectively proportional to the -0.37 and -0.36 powers of p_{H_2}, indicating that its dependence on p_{H_2} is almost the same for both cells. That is, the increase in R_{dif} is caused not by the extension of the electrode–electrolyte interfacial area but by the increase in the average anode thickness. Moreover, the absolute change in R_{dif} shows the smallest among the others, as summarized in **Table 4.4**, and is almost the same regardless of p_{H_2}. This indicates that the increase in R_{dif} is not a factor that impedes the improvement in cell performance due to the mesostructural modification.

Owing to the changes in each resistance component by the mesostructural modification, the total resistance in the mesoscale-modified cell (0.95–1.3 Ω cm^2) is reduced compared with that in the flat cell (1.5–1.6 Ω cm^2), but its decrease becomes smaller with decreasing p_{H_2}. Therefore, it can be concluded that the effect of the mesostructural modification on the cell performance that fades away under a low H_2 is mainly caused by the fact that the decrease in the anodic activation resistance becomes smaller with decreasing p_{H_2}.

4.4 Summary

In this chapter, the effect of the mesostructural modification of the electrode–electrolyte interface on the electrochemical performance of anode-supported SOFCs was quantitatively evaluated under various H_2 partial pressures through EIS analysis. The flat and mesoscale-modified cells with the configuration of Ni–YSZ/YSZ/GDC/LSCF–GDC were prepared and then their structural analysis and electrochemical characterization were carried out. The electrode–electrolyte interfacial area in the mesoscale-modified cell was extended by about 6.8 % compared with that in the flat cell, resulting in an increase in the area of the electrochemically active regions in both electrodes. Simultaneously, the average anode thickness in the mesoscale-modified cell was also increased. By evaluating the electrochemical performance of the cells, it was confirmed that the cell performance was less improved under a low H_2 partial pressure condition. To clarify which resistance component mainly caused the effect of the mesostructural modification to fade away, the EIS data of the cells were analyzed using the DRT method followed by the CNLS fitting. The gas diffusion resistance was increased because of the increase in the anode thickness, but its increase was relatively small and was almost constant regardless of the H_2 partial pressure. On the other hand, the anodic activation resistances in the flat and mesoscale-modified cells were decreased and increased, respectively, with decreasing H_2 partial pressure. Owing to the opposite dependence on the H_2 partial pressure, its decrease became smaller with decreasing H_2 partial pressure, leading to little improvement in cell performance particularly under a low H_2.

5

Conclusions and outlook

5.1 Conclusions

This dissertation addressed the preparation and electrochemical characteristics of anode-supported SOFCs where the electrode–electrolyte interface is structurally modified on the mesoscale order.

In Chapter 2, microextrusion printing, one of the additive manufacturing processes, was proposed as an alternative fabrication method for increasing the electrode–electrolyte interface to overcome the problems in subtractive manufacturing. To predict the line width of an extruded paste from a micronozzle, the mathematical model where the contact angle between the paste and the substrate is taken into consideration was developed. Using this model, desirable anode ridge structures were successfully fabricated on the flat anode disk. By varying a paste coverage area, two types of anode-supported SOFCs having different interfacial area enlargement ratios were prepared. It was demonstrated that the cell performance was improved by increasing the interfacial area, which was due to the decreases in the ohmic and activation resistances. Also, the improvement in cell performance was prominent at a low operating temperature and high hydrogen partial pressure.

In Chapter 3, the mechanism of the improvement in cell performance by the mesostructural modification of the electrode–electrolyte during power generation was clarified through experiment and numerical simulation. The 2D numerical model where the structures in a wide range of length scales of the tested cells were implemented was developed, and then its validity was verified by comparing the simulation results with the experimental ones. The structural features in the mesoscale-

modified cell, such as interfacial area enlargement and thickness inhomogeneity, caused nonuniform distributions of the physicochemical quantities that contribute to the electrochemical reactions. Consequently, the decreases in the ohmic and activation overpotentials of the mesoscale-modified cell relative to the flat cell obtained from the simulation were larger and smaller than those estimated under the assumptions that the ionic and charge-transfer currents uniformly flow inside a cell, respectively. Moreover, the ionic current density distribution had strong nonuniformity under high current density conditions, leading to a significantly large relative decrease in the ohmic loss. On the other hand, the concentration overpotential in the anode was slightly increased, which was mainly caused by the fact that the average anode thickness was increased by attaching the anode ridge structures. However, it rarely hindered the improvement in cell performance under a high hydrogen partial pressure condition set in this work. Furthermore, the decrease in the total ohmic loss accounted for the majority of the total decrease in cell overpotential, which made the greatest contribution to the improvement in cell performance.

In Chapter 4, the mesostructural modification effect on the cell performance under various hydrogen partial pressure conditions was quantitatively evaluated through electrochemical impedance spectroscopy analysis. To clarify which resistance component mainly caused the effect of the mesostructural modification to fade away, the EIS data of the cells were analyzed using the DRT method followed by the CNLS fitting. The gas diffusion resistance was increased because of the increase in the average anode thickness, but its increase was relatively small and was almost constant regardless of the hydrogen partial pressure. On the other hand, the anodic activation resistances in the flat and mesoscale-modified cells were decreased and increased, respectively, with decreasing hydrogen partial pressure. Owing to the opposite dependence on the H_2 partial pressure, its decrease became smaller with decreasing hydrogen partial pressure, leading to little improvement in cell performance particularly under a low hydrogen partial pressure condition.

5.2 Outlook

Through this dissertation, it was clarified that the effect of the mesostructural modification for anode-supported SOFCs in terms of the improvement in cell performance is most prominent under a low operating temperature and high hydrogen partial pressure. Owing to this advantage, its application to practical-size cells (typically around 100×100 mm^2) is highly expected in the future. Note that, however, the physicochemical quantities that contribute to the electrochemical reactions are nonuniformly distributed in the entire region of such cells, regardless of whether or not the electrode–electrolyte interface is flat. It can be presumed from this fact that their inhomogeneity will considerably be stronger in mesoscale-modified cells with a larger size, causing severer cell degradation. Therefore, it is extremely challenging but necessary to make distributions inside a mesoscale-modified cell relatively homogeneous during power generation to realize a long-life cell with high performance.

On the other hand, even though practical-size cells, there is a space limitation of the printable area in a horizontal plane that is parallel to the electrode–electrolyte interface. Thus, fully utilizing the advantages of 3D printing will play a vital role in the further extension of the electrode–electrolyte interfacial area. For instance, it is considered effective to reduce the width of an anode ridge structure created by microextrusion printing and simultaneously to increase its height. This will give an additional improvement in the electrochemical performance of SOFCs.

Appendix

Appendix A. Electrolyte thickness in mesoscale-modified cell

This appendix describes the electrolyte thickness in the mesoscale-modified cell discussed in Section 3.4.3.2.

As illustrated in **Fig. A.1**, suppose that the equations of the geometric shapes of the anode–electrolyte interface (green solid line) and cathode–electrolyte interface (gray solid line), which are defined on a closed interval $\left[-\frac{L}{2}, \frac{L}{2}\right]$, are respectively given as

$$y' = \begin{cases} \frac{\Delta}{2} + \sqrt{\left(\frac{w_{\text{A–E}}}{2\sin\frac{\theta_{\text{A–E}}}{2}}\right)^2 - x'^2}, & |x'| \le \frac{w_{\text{A–E}}}{2} \\ \frac{\Delta}{2} + \frac{w_{\text{A–E}}}{2\tan\frac{\theta_{\text{A–E}}}{2}}, & \text{otherwise} \end{cases} \tag{A.1}$$

$$y' = \begin{cases} -\frac{\Delta}{2} + \sqrt{\left(\frac{w_{\text{C–E}}}{2\sin\frac{\theta_{\text{C–E}}}{2}}\right)^2 - x'^2}, & |x'| \le \frac{w_{\text{C–E}}}{2} \\ -\frac{\Delta}{2} + \frac{w_{\text{C–E}}}{2\tan\frac{\theta_{\text{C–E}}}{2}}, & \text{otherwise} \end{cases}. \tag{A.2}$$

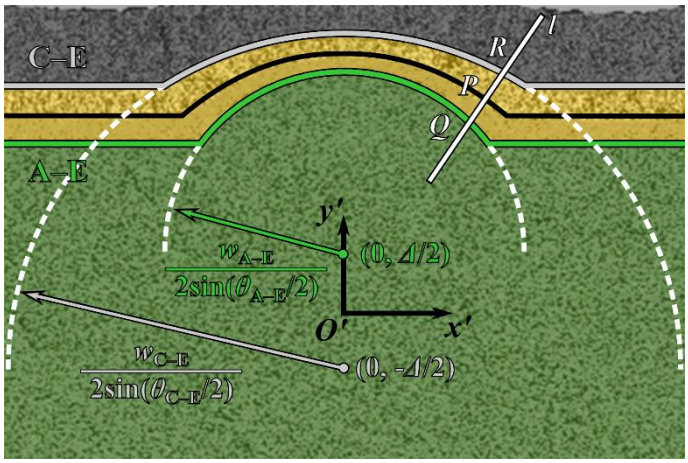

Fig. A.1 Geometric shapes of the electrode–electrolyte interface in mesoscale-modified cell modeled by circular arc and straight line.

Then, the centerline between the interfaces is an ellipse whose minor and major axes are respectively $\sqrt{\left(\frac{w_{\mathrm{A-E}}}{2\sin\frac{\theta_{\mathrm{A-E}}}{2}}+\frac{w_{\mathrm{C-E}}}{2\sin\frac{\theta_{\mathrm{C-E}}}{2}}\right)^2-\Delta^2}$ and $\frac{w_{\mathrm{A-E}}}{2\sin\frac{\theta_{\mathrm{A-E}}}{2}}+\frac{w_{\mathrm{C-E}}}{2\sin\frac{\theta_{\mathrm{C-E}}}{2}}$ (*113*) when $|x'|\le\frac{w_{\mathrm{A-E}}+w_{\mathrm{C-E}}}{4}$, and a straight line otherwise. Thus, its equation can be written as

$$y'=\begin{cases}\frac{1}{2}\dfrac{\frac{w_{\mathrm{A-E}}}{2\sin\frac{\theta_{\mathrm{A-E}}}{2}}+\frac{w_{\mathrm{C-E}}}{2\sin\frac{\theta_{\mathrm{C-E}}}{2}}}{\sqrt{\left(\frac{w_{\mathrm{A-E}}}{2\sin\frac{\theta_{\mathrm{A-E}}}{2}}+\frac{w_{\mathrm{C-E}}}{2\sin\frac{\theta_{\mathrm{C-E}}}{2}}\right)^2-\Delta^2}}\sqrt{\left(\frac{w_{\mathrm{A-E}}}{2\sin\frac{\theta_{\mathrm{A-E}}}{2}}+\frac{w_{\mathrm{C-E}}}{2\sin\frac{\theta_{\mathrm{C-E}}}{2}}\right)^2-\Delta^2-4x'^2}, & |x'|\le\frac{w_{\mathrm{A-E}}+w_{\mathrm{C-E}}}{4}\\ \frac{1}{2}\left(\frac{w_{\mathrm{A-E}}}{2\tan\frac{\theta_{\mathrm{A-E}}}{2}}+\frac{w_{\mathrm{C-E}}}{2\tan\frac{\theta_{\mathrm{C-E}}}{2}}\right), & \text{otherwise}\end{cases}. \tag{A.3}$$

Now, supposing that a line l perpendicular to a tangent line at a given point $P(x_P{}', y_P{}')$, on the centerline between the interfaces passes through the given point, its equation can be expressed as

$$l:\begin{cases}y'=A(x_P{}')x'+B(x_P{}'), & 0<|x'|\le\frac{w_{\mathrm{A-E}}+w_{\mathrm{C-E}}}{4}\\ x'=x_P{}', & \text{otherwise}\end{cases}. \tag{A.4}$$

Here, $A(x_P{}')$ and $B(x_P{}')$ are respectively described as

$$A(x_P{}')=\frac{\sqrt{\left(\frac{w_{\mathrm{C-E}}}{2\sin\left(\frac{\theta_{\mathrm{C-E}}}{2}\right)}+\frac{w_{\mathrm{A-E}}}{2\sin\left(\frac{\theta_{\mathrm{A-E}}}{2}\right)}\right)^2-\Delta^2}\sqrt{\left(\frac{w_{\mathrm{C-E}}}{2\sin\left(\frac{\theta_{\mathrm{C-E}}}{2}\right)}+\frac{w_{\mathrm{A-E}}}{2\sin\left(\frac{\theta_{\mathrm{A-E}}}{2}\right)}\right)^2-\Delta^2-4x_P{}'^2}}{2\left(\frac{w_{\mathrm{C-E}}}{2\sin\left(\frac{\theta_{\mathrm{C-E}}}{2}\right)}+\frac{w_{\mathrm{A-E}}}{2\sin\left(\frac{\theta_{\mathrm{A-E}}}{2}\right)}\right)x_P{}'} \tag{A.5}$$

$$B(x_P{}')=\frac{\Delta^2}{\frac{w_{\mathrm{C-E}}}{2\sin\frac{\theta_{\mathrm{C-E}}}{2}}+\frac{w_{\mathrm{A-E}}}{2\sin\frac{\theta_{\mathrm{A-E}}}{2}}}\sqrt{\frac{1}{4}-\frac{x_P{}'^2}{\left(\frac{w_{\mathrm{C-E}}}{2\sin\frac{\theta_{\mathrm{C-E}}}{2}}+\frac{w_{\mathrm{A-E}}}{2\sin\frac{\theta_{\mathrm{A-E}}}{2}}\right)^2-\Delta^2}}. \tag{A.6}$$

If two points $Q(x_Q', y_Q')$ and $R(x_R', y_R')$ that are respectively on the anode–electrolyte interface and cathode–electrolyte interface are on the line l, their coordinates are respectively calculated as

$$x_Q' = \begin{cases} \dfrac{-A(x_P)\left(B(x_P)-\frac{\Delta}{2}\right)+\sqrt{(A(x_P))^2+1\left(\frac{w_{\text{A–E}}}{2\sin\frac{\theta_{\text{A–E}}}{2}}\right)^2-\left(B(x_P)-\frac{\Delta}{2}\right)^2}}{(A(x_P))^2+1}, & 0<|x_P'|\le\frac{w_{\text{A–E}}+w_{\text{C–E}}}{4} \\ x_P', & \text{otherwise} \\ \frac{\Delta}{2}+\dfrac{w_{\text{A–E}}}{2\sin\frac{\theta_{\text{A–E}}}{2}}, & x_P'=0 \end{cases} \tag{A.7}$$

$$y_Q' = \begin{cases} A(x_P)\dfrac{-A(x_P)\left(B(x_P)-\frac{\Delta}{2}\right)+\sqrt{(A(x_P))^2+1\left(\frac{w_{\text{A–E}}}{2\sin\frac{\theta_{\text{A–E}}}{2}}\right)^2-\left(B(x_P)-\frac{\Delta}{2}\right)^2}}{(A(x_P))^2+1}+B(x_P), & 0<|x_P'|\le\frac{w_{\text{A–E}}+w_{\text{C–E}}}{4} \\ \frac{\Delta}{2}+\dfrac{w_{\text{A–E}}}{2\tan\frac{\theta_{\text{A–E}}}{2}}, & \text{otherwise} \end{cases} \tag{A.8}$$

$$x_R' = \begin{cases} \dfrac{-A(x_P)\left(B(x_P)+\frac{\Delta}{2}\right)+\sqrt{(A(x_P))^2+1\left(\frac{w_{\text{C–E}}}{2\sin\frac{\theta_{\text{C–E}}}{2}}\right)^2-\left(B(x_P)+\frac{\Delta}{2}\right)^2}}{(A(x_P))^2+1}, & 0<|x_P'|\le\frac{w_{\text{A–E}}+w_{\text{C–E}}}{4} \\ x_P', & \text{otherwise} \end{cases} \tag{A.9}$$

$$y_R' = \begin{cases} -\frac{\Delta}{2}+\dfrac{w_{\text{C–E}}}{2\sin\frac{\theta_{\text{C–E}}}{2}}, & x_P'=0 \\ A(x_P)\dfrac{-A(x_P)\left(B(x_P)+\frac{\Delta}{2}\right)+\sqrt{(A(x_P))^2+1\left(\frac{w_{\text{C–E}}}{2\sin\frac{\theta_{\text{C–E}}}{2}}\right)^2-\left(B(x_P)+\frac{\Delta}{2}\right)^2}}{(A(x_P))^2+1}+B(x_P), & 0<|x_P'|\le\frac{w_{\text{A–E}}+w_{\text{C–E}}}{4} \\ -\frac{\Delta}{2}+\sqrt{\left(\frac{w_{\text{C–E}}}{2\sin\frac{\theta_{\text{C–E}}}{2}}\right)^2-x_P'^2}, & \frac{w_{\text{A–E}}+w_{\text{C–E}}}{4}\le|x_P'|\le\frac{w_{\text{C–E}}}{2} \\ -\frac{\Delta}{2}+\dfrac{w_{\text{C–E}}}{2\tan\frac{\theta_{\text{C–E}}}{2}}, & \text{otherwise} \end{cases} \tag{A.10}$$

Therefore, the electrolyte thickness defined in the direction perpendicular to the centerline between the interfaces corresponds to the distance between the two points QR, which can be calculated as

$$QR = \begin{cases} \frac{w_{\text{C–E}}}{2\sin\frac{\theta_{\text{C–E}}}{2}} - \frac{w_{\text{A–E}}}{2\sin\frac{\theta_{\text{A–E}}}{2}} - \Delta, & x_P' = 0 \\ \sqrt{\left(\frac{w_{\text{C–E}}}{2\sin\frac{\theta_{\text{C–E}}}{2}}\right)^2 - \frac{\left(B(x_P')+\frac{\Delta}{2}\right)^2}{\left(A(x_P')\right)^2+1}} - \sqrt{\left(\frac{w_{\text{A–E}}}{2\sin\frac{\theta_{\text{A–E}}}{2}}\right)^2 - \frac{\left(B(x_P')-\frac{\Delta}{2}\right)^2}{\left(A(x_P')\right)^2+1}} - \frac{A(x_P')\Delta}{\sqrt{\left(A(x_P')\right)^2+1}}, & 0 < |x_P'| \le \frac{w_{\text{A–E}}+w_{\text{C–E}}}{4} \\ \sqrt{\left(\frac{w_{\text{C–E}}}{2\sin\frac{\theta_{\text{C–E}}}{2}}\right)^2 - x_P'^2} - \frac{w_{\text{A–E}}}{2\tan\frac{\theta_{\text{A–E}}}{2}} - \Delta, & \frac{w_{\text{A–E}}+w_{\text{C–E}}}{4} \le |x_P'| \le \frac{w_{\text{C–E}}}{2} \\ \frac{w_{\text{C–E}}}{2\tan\frac{\theta_{\text{C–E}}}{2}} - \frac{w_{\text{A–E}}}{2\tan\frac{\theta_{\text{A–E}}}{2}} - \Delta, & \text{otherwise} \end{cases}$$

. (A.11)

Appendix B. Inequality of activation energy loss

This appendix describes the inequality of the activation energy loss in the mesoscale-modified cell discussed in Section 3.4.3.3.

Let $f(x)$ and $g(x)$ be continuous functions satisfying the following conditions:

I. $f(x)$ and $g(x)$ are defined on a closed interval $[x_0, x_n]$.

II. $f(x)$ is a constant function.

III. The definite integrals of $f(x)$ and $g(x)$ from x_0 to x_n are the same.

Assume that $f(x_i) + f(x_{n-i}) = g(x_i) + g(x_{n-i})$ $(0 \le i \le n,\ n \ne 0)$ for any real numbers included in the given closed interval. Now, supposing that $h(x)$ defined on the closed interval is a function that is strictly increasing and concave up (*e.g.*, $x\sinh^{-1}(x)$), the following inequality can be established (*114*):

$$h\big(f(x_i)\big) + h\big(f(x_{n-i})\big) \le h\big(g(x_i)\big) + h\big(g(x_{n-i})\big) \tag{B.1}$$

with equality if and only if $f(x_i) = g(x_i)$. Then,

$$\sum_{i=0}^{n}\big[h\big(f(x_i)\big) + h\big(f(x_{n-i})\big)\big] \le \sum_{i=0}^{n}\big[h\big(g(x_i)\big) + h\big(g(x_{n-i})\big)\big]. \tag{B.2}$$

Owing to the facts that

$$\sum_{i=0}^{n} h\big(f(x_i)\big) = \sum_{i=0}^{n} h\big(f(x_{n-i})\big) \tag{B.3}$$

$$\sum_{i=0}^{n} h\big(g(x_i)\big) = \sum_{i=0}^{n} h\big(g(x_{n-i})\big), \tag{B.4}$$

the following inequality can be obtained:

$$\sum_{i=0}^{n} h\big(f(x_i)\big) \leq \sum_{i=0}^{n} h\big(g(x_i)\big). \tag{B.5}$$

Multiplying both sides by $\frac{x_n - x_0}{n}$ gives

$$\sum_{i=0}^{n} h\big(f(x_i)\big)\frac{x_n - x_0}{n} \leq \sum_{i=0}^{n} h\big(g(x_i)\big)\frac{x_n - x_0}{n}. \tag{B.6}$$

Taking the limit of both sides of the above inequality as n approaches infinity, we have:

$$\lim_{n\to\infty} \sum_{i=0}^{n} h\big(f(x_i)\big)\frac{x_n - x_0}{n} \leq \lim_{n\to\infty} \sum_{i=0}^{n} h\big(g(x_i)\big)\frac{x_n - x_0}{n}. \tag{B.7}$$

Therefore,

$$\int_{x_0}^{x_n} h\big(f(x)\big)dx \leq \int_{x_0}^{x_n} h\big(g(x)\big)dx. \tag{B.8}$$

Equality holds if and only if $f(x) = g(x)$ (*i.e.*, $g(x)$ is a constant function).

Nomenclature

A_{DPB}	DPB density / $\mathrm{m^{-1}}$
$\widetilde{D}$	chemical diffusion coefficient / $\mathrm{m^2\ s^{-1}}$
D_{ij}	molecular diffusivity / $\mathrm{m^2\ s^{-1}}$
$D_{i,\mathrm{K}}$	Knudsen diffusivity / $\mathrm{m^2\ s^{-1}}$
d_i	particle/pore diameter / m
F	Faraday constant / $\mathrm{A\ s\ mol^{-1}}$
ΔG_0	standard Gibbs free energy change / $\mathrm{J\ mol^{-1}}$
i	current density / $\mathrm{A\ m^{-2}}$
$i_{0,\mathrm{DPB}}$	exchange current density per unit DPB area / $\mathrm{A\ m^{-2}}$
$i_{0,\mathrm{TPB}}$	exchange current density per unit TPB length / $\mathrm{A\ m^{-1}}$
i_{ct}	charge-transfer current density / $\mathrm{A\ m^{-3}}$
K	permeability / $\mathrm{m^2}$
k	ratio of electrolyte volume / –
L	single repeating unit / m
l_{TPB}	TPB density / $\mathrm{m^{-2}}$
M_i	molar mass / $\mathrm{kg\ mol^{-1}}$
N_i	molar flux / $\mathrm{mol\ m^{-2}\ s^{-1}}$
P_i	partial pressure / Pa
P_{t}	total pressure / Pa
Q	energy loss / W
R	universal gas constant / $\mathrm{J\ K^{-1}\ mol^{-1}}$
RD	relative decrease / –
$(S/V)_i$	surface-to-volume ratio / $\mathrm{m^{-1}}$
s_i	sink/source term for gas species / $\mathrm{mol\ m^{-3}\ s^{-1}}$

T	temperature / K
t	thickness / m
t_{eff}	thickness of effective reaction region / m
V_i	volume fraction / –
V_{m}	perovskite molar volume / $\mathrm{m^3\ mol^{-1}}$
V_{T}	terminal voltage / V
v_i	molecular diffusion volume / $\mathrm{m^3\ mol^{-1}}$
w	width of ridge structure / m
X_i	molar fraction / –

Greek symbols

α	interfacial area enlargement factor / –
Δ	distance between centers of two arcs / m
δ	oxygen nonstoichiometry / –
η	overpotential / V
θ	central angle / rad
μ	viscosity / Pa s
μ_i	electrochemical potential / $\mathrm{J\ mol^{-1}}$
σ_i	conductivity / $\mathrm{S\ m^{-1}}$
τ_i	tortuosity factor / –

Superscripts

bulk	value for bulk materials
eff	effective value for porous materials

Subscripts

A–E	anode–electrolyte interface
ano	anode
act	activation
C–E	cathode –electrolyte interface
cat	cathode
cell	cell
con	concentration
e^-	electronic
ele	electrolyte
FLAT	flat cell
MESO	mesoscale-modified cell
O^{2-}	oxide ionic
ohm	ohmic

References

1. D. J. L. Brett, A. Atkinson, N. P. Brandon, S. J. Skinner, Intermediate temperature solid oxide fuel cells. *Chem. Soc. Rev.* **37**, 1568–1578 (2008).
2. A. Tarancón, Strategies for lowering solid oxide fuel cells operating temperature. *Energies*. **2**, 1130–1150 (2009).
3. E. D. Wachsman, K. T. Lee, Lowering the temperature of solid oxide fuel cells. *Science.* **334**, 935–939 (2011).
4. B. Shri Prakash, R. Pavitra, S. Senthil Kumar, S. T. Aruna, Electrolyte bi-layering strategy to improve the performance of an intermediate temperature solid oxide fuel cell: A review. *J. Power Sources*. **381**, 136–155 (2018).
5. M. Brown, S. Primdahl, M. Mogensen, Structure/performance relations for Ni/yttria-stabilized zirconia anodes for solid oxide fuel cells. *J. Electrochem. Soc.* **147**, 475–485 (2000).
6. J. Kong, K. Sun, D. Zhou, N. Zhang, J. Mu, J. Qiao, Ni–YSZ gradient anodes for anode-supported SOFCs. *J. Power Sources*. **166**, 337–342 (2007).
7. K. Chen, X. Chen, Z. Lü, N. Ai, X. Huang, W. Su, Performance of an anode-supported SOFC with anode functional layers. *Electrochim. Acta*. **53**, 7825–7830 (2008).
8. H. Moon, S. D. Kim, E. W. Park, S. H. Hyun, H. S. Kim, Characteristics of SOFC single cells with anode active layer via tape casting and co-firing. *Int. J. Hydrogen Energy*. **33**, 2826–2833 (2008).
9. K. Yuan, Y. Ji, J. N. Chung, Physics-based modeling of a low-temperature solid oxide fuel cell with consideration of microstructure and interfacial effects. *J. Power Sources*. **194**, 908–919 (2009).
10. Q. Cai, C. S. Adjiman, N. P. Brandon, Investigation of the active thickness of solid oxide fuel cell electrodes using a 3D microstructure model. *Electrochim. Acta*. **56**, 10809–10819 (2011).

11. A. Konno, H. Iwai, M. Saito, H. Yoshida, Effect of characteristic lengths of electron, ion, and gas diffusion on electrode performance and electrochemical reaction area in a solid oxide fuel cell. *Heat Transf. Res.* **41**, 700–718 (2012).

12. M. Kishimoto, H. Iwai, M. Saito, H. Yoshida, Characteristic length of oxide-ion conduction for prediction of active thickness in SOFC anode. *ECS Trans.* **57**, 2515–2525 (2013).

13. A. A. E. Hassan, N. H. Menzler, G. Blass, M. E. Ali, H. P. Buchkremer, D. Stöver, Development of an optimized anode functional layer for solid oxide fuel cell applications. *Adv. Eng. Mater.* **4**, 125–129 (2002).

14. M. D. Gross, J. M. Vohs, R. J. Gorte, An examination of SOFC anode functional layers based on ceria in YSZ. *J. Electrochem. Soc.* **154**, B694–B699 (2007).

15. D. Young, A. M. Sukeshini, R. Cummins, H. Xiao, M. Rottmayer, T. Reitz, Ink-jet printing of electrolyte and anode functional layer for solid oxide fuel cells. *J. Power Sources*. **184**, 191–196 (2008).

16. Z. Wang, N. Zhang, J. Qiao, K. Sun, P. Xu, Improved SOFC performance with continuously graded anode functional layer. *Electrochem. commun.* **11**, 1120–1123 (2009).

17. S. P. Jiang, Y. Y. Duan, J. G. Love, Fabrication of high-performance Ni/Y_2O_3-ZrO_2 cermet anodes of solid oxide fuel cells by ion impregnation. *J. Electrochem. Soc.* **149**, A1175–A1183 (2002).

18. S. P. Jiang, Y. J. Leng, S. H. Chan, K. A. Khor, Development of (La,Sr)MnO_3-based cathodes for intermediate temperature solid oxide fuel cells. *Electrochem. Solid-State Lett.* **6**, A67–A70 (2003).

19. J. Chen, F. Liang, B. Chi, J. Pu, S. P. Jiang, L. Jian, Palladium and ceria infiltrated $La_{0.8}Sr_{0.2}Co_{0.5}Fe_{0.5}O_{3-\delta}$ cathodes of solid oxide fuel cells. *J. Power Sources*. **194**, 275–280 (2009).

20. T. Hong, L. Zhang, F. Chen, C. Xia, Oxygen surface exchange properties of $La_{0.6}Sr_{0.4}Co_{0.8}Fe_{0.2}O_{3-\delta}$ coated with $Sm_xCe_{1-x}O_{2-\delta}$. *J. Power Sources*. **218**, 254–260 (2012).

21. E. Zhao, Z. Jia, L. Zhao, Y. Xiong, C. Sun, M. E. Brito, One dimensional $La_{0.8}Sr_{0.2}Co_{0.2}Fe_{0.8}O_{3-\delta}/Ce_{0.8}Gd_{0.2}O_{1.9}$ nanocomposite cathodes for intermediate temperature solid oxide fuel cells. *J. Power Sources*. **219**, 133–139 (2012).

22. L. Zhao, S. Amarasinghe, S. P. Jiang, Enhanced chromium tolerance of $La_{0.6}Sr_{0.4}Co_{0.2}Fe_{0.8}O_{3-\delta}$ electrode of solid oxide fuel cells by $Gd_{0.1}Ce_{0.9}O_{1.95}$ impregnation. *Electrochem. commun.* **37**, 84–87 (2013).

23. M. Kishimoto, M. Lomberg, E. Ruiz-Trejo, N. P. Brandon, Enhanced triple-phase boundary density in infiltrated electrodes for solid oxide fuel cells demonstrated by high-resolution tomography. *J. Power Sources*. **266**, 291–295 (2014).

24. M. Kishimoto, Y. Kawakami, Y. Otani, H. Iwai, H. Yoshida, Improved controllability of wet infiltration technique for fabrication of solid oxide fuel cell anodes. *Scr. Mater.* **140**, 5–8 (2017).

25. F. Guan, X. Zhang, Y. Song, Y. Zhou, G. Wang, X. Bao, Effect of $Gd_{0.2}Ce_{0.8}O_{1.9}$ nanoparticles on the oxygen evolution reaction of $La_{0.6}Sr_{0.4}Co_{0.2}Fe_{0.8}O_{3-\delta}$ anode in solid oxide electrolysis cell. *Chinese J. Catal.* **39**, 1484–1492 (2018).

26. H. Shimada, T. Yamaguchi, H. Kishimoto, H. Sumi, Y. Yamaguchi, K. Nomura, Y. Fujishiro, Nanocomposite electrodes for high current density over 3 A cm^{-2} in solid oxide electrolysis cells. *Nat. Commun.* **10**, 5432 (2019).

27. A. Konno, H. Iwai, K. Inuyama, A. Kuroyanagi, M. Saito, H. Yoshida, K. Kodani, K. Yoshikata, Mesoscale-structure control at anode/electrolyte interface in solid oxide fuel cell. *J. Power Sources*. **196**, 98–109 (2011).

28. Y. Xu, F. Tsumori, H. Kang, H. Miura, Fabrication of micro patterned ceramic structure by imprinting process. *J. Japan Soc. Powder Powder Metall.* **58**, 673–678 (2011).

29. Y. Xu, F. Tsumori, H. Miura, T. Osada, Improvement of solid oxide fuel cell by imprinted micropatterns on electrolyte. *Micro Nano Lett.* **8**, 571–574 (2013).

30. F. Tsumori, Y. Xu, Y. Tanaka, T. Osada, H. Miura, Micrometer-scale imprinting process for ceramic sheet from powder compound material. *Procedia Eng.* **81**, 1433–1438 (2014).

31. A. Larrea, D. Sola, M. A. Laguna-Bercero, J. I. Peña, R. I. Merino, V. M. Orera, Self-supporting thin yttria-stabilised zirconia electrolytes for solid oxide fuel cells prepared by laser machining. *J. Electrochem. Soc.* **158**, B1193–B1197 (2011).

32. A. Cubero, J. I. Peña, M. A. Laguna-Bercero, Optimization of Ni–YSZ solid oxide fuel cell anodes by surface laser melting. *Appl. Surf. Sci.* **335**, 39–43 (2015).

33. H. Dai, S. He, H. Chen, L. Guo, A novel method of modifying electrolyte surface at mesoscale for intermediate-temperature solid oxide fuel cells. *Ceram. Int.* **42**, 2045–2050 (2016).

34. J. A. Cebollero, R. Lahoz, M. A. Laguna-Bercero, A. Larrea, Tailoring the electrode-electrolyte interface of solid oxide fuel cells (SOFC) by laser micro-patterning to improve their electrochemical performance. *J. Power Sources*. **360**, 336–344 (2017).

35. G. Cai, Y. Zhang, H. Dai, S. He, L. Ge, H. Chen, L. Guo, Modification of electrode/electrolyte interface by laser micro-processing for solid oxide fuel cell. *Mater. Lett.* **195**, 232–235 (2017).

36. A. Chesnaud, F. Delloro, M. Geagea, A.-P. Abellard, J. Ouyang, D. Li, T. Shi, B. Chi, R. Ihringer, M. Cassir, A. Thorel, Corrugated electrode/electrolyte interfaces in SOFC: Theoretical and experimental development. *ECS Trans.* **78**, 1851–1863 (2017).

37. Y. Zhang, G. Cai, Y. Gu, L. Ge, Y. Zheng, H. Chen, L. Guo, Modifying the electrode-electrolyte interface of anode supported solid oxide fuel cells (SOFCs) by laser-machining. *Energy Convers. Manag.* **171**, 1030–1037 (2018).

38. J. A. Cebollero, M. A. Laguna-Bercero, R. Lahoz, J. Silva, R. Moreno, A. Larrea, Optimization of laser-patterned YSZ-LSM composite cathode-electrolyte interfaces for solid oxide fuel cells. *J. Eur. Ceram. Soc.* **39**, 3466–3474 (2019).

39. H. Iwai, A. Kuroyanagi, M. Saito, A. Konno, H. Yoshida, T. Yamada, S. Nishiwaki, Power generation enhancement of solid oxide fuel cell by cathode–electrolyte interface modification in mesoscale assisted by level set-based optimization calculation. *J. Power Sources*. **196**, 3485–3495 (2011).

40. A. Konno, H. Iwai, M. Saito, H. Yoshida, A corrugated mesoscale structure on electrode–

electrolyte interface for enhancing cell performance in anode-supported SOFC. *J. Power Sources*. **196**, 7442–7449 (2011).

41. A. Bertei, F. Tariq, V. Yufit, E. Ruiz-Trejo, N. P. Brandon, Guidelines for the rational design and engineering of 3D manufactured solid oxide fuel cell composite electrodes. *J. Electrochem. Soc.* **164**, F89–F98 (2017).

42. A. He, T. Shimura, J. Gong, N. Shikazono, Numerical simulation of $La_{0.6}Sr_{0.4}Co_{0.2}Fe_{0.8}O_3$-$Gd_{0.1}Ce_{0.9}O_{1.95}$ composite cathodes with micro pillars. *Int. J. Hydrogen Energy*. **44**, 6871–6885 (2019).

43. C.-C. Chueh, A. Bertei, C. Nicolella, Design guidelines for the manufacturing of the electrode-electrolyte interface of solid oxide fuel cells. *J. Power Sources*. **437**, 226888 (2019).

44. T. Shimura, K. Nagato, N. Shikazono, Evaluation of electrochemical performance of solid-oxide fuel cell anode with pillar-based electrolyte structures. *Int. J. Hydrogen Energy*. **44**, 12043–12056 (2019).

45. A. He, J. Onishi, N. Shikazono, Optimization of electrode-electrolyte interface structure for solid oxide fuel cell cathode. *J. Power Sources*. **449**, 227565 (2020).

46. H. Schichlein, A. Müller, M. Voigts, A. Krügel, E. Ivers-Tiffée, Deconvolution of electrochemical impedance spectra for the identification of electrode reaction mechanisms in solid oxide fuel cells. *J. Appl. Electrochem.* **32**, 875–882 (2002).

47. A. Leonide, V. Sonn, A. Weber, E. Ivers-Tiffée, Evaluation and modeling of the cell resistance in anode-supported solid oxide fuel cells. *J. Electrochem. Soc.* **155**, B36–B41 (2008).

48. V. Sonn, A. Leonide, E. Ivers-Tiffée, Combined deconvolution and CNLS fitting approach applied on the impedance response of technical Ni/8YSZ cermet electrodes. *J. Electrochem. Soc.* **155**, B675–B679 (2008).

49. B. Liu, H. Muroyama, T. Matsui, K. Tomida, T. Kabata, K. Eguchi, Analysis of impedance spectra for segmented-in-series tubular solid oxide fuel cells. *J. Electrochem. Soc.* **157**, B1858–B1864 (2010).

50. H. Sumi, T. Yamaguchi, K. Hamamoto, T. Suzuki, Y. Fujishiro, T. Matsui, K. Eguchi, AC impedance characteristics for anode-supported microtubular solid oxide fuel cells. *Electrochim. Acta*. **67**, 159–165 (2012).

51. A. Kromp, H. Geisler, A. Weber, E. Ivers-Tiffée, Electrochemical impedance modeling of gas transport and reforming kinetics in reformate fueled solid oxide fuel cell anodes. *Electrochim. Acta*. **106**, 418–424 (2013).

52. M. Saccoccio, T. H. Wan, C. Chen, F. Ciucci, Optimal regularization in distribution of relaxation times applied to electrochemical impedance spectroscopy: Ridge and Lasso regression methods - A theoretical and experimental study. *Electrochim. Acta*. **147**, 470–482 (2014).

53. F. Ciucci, C. Chen, Analysis of electrochemical impedance spectroscopy data using the distribution of relaxation times: A Bayesian and hierarchical Bayesian approach. *Electrochim. Acta*. **167**, 439–454 (2015).

54. H. Sumi, H. Shimada, Y. Yamaguchi, T. Yamaguchi, Y. Fujishiro, Degradation evaluation by distribution of relaxation times analysis for microtubular solid oxide fuel cells. *Electrochim. Acta*. **339**, 135913 (2020).

55. S. Dierickx, A. Weber, E. Ivers-Tiffée, How the distribution of relaxation times enhances complex equivalent circuit models for fuel cells. *Electrochim. Acta*. **355**, 136764 (2020).

56. R. I. Tomov, M. Krauz, J. Jewulski, S. C. Hopkins, J. R. Kluczowski, D. M. Glowacka, B. A. Glowacki, Direct ceramic inkjet printing of yttria-stabilized zirconia electrolyte layers for anode-supported solid oxide fuel cells. *J. Power Sources*. **195**, 7160–7167 (2010).

57. V. Esposito, C. Gadea, J. Hjelm, D. Marani, Q. Hu, K. Agersted, S. Ramousse, S. H. Jensen, Fabrication of thin yttria-stabilized-zirconia dense electrolyte layers by inkjet printing for high performing solid oxide fuel cells. *J. Power Sources*. **273**, 89–95 (2015).

58. S. Masciandaro, M. Torrell, P. Leone, A. Tarancón, Three-dimensional printed yttria-stabilized zirconia self-supported electrolytes for solid oxide fuel cell applications. *J. Eur. Ceram. Soc.*

39, 9–16 (2019).

59. E. M. Hernández-Rodríguez, P. Acosta-Mora, J. Méndez-Ramos, E. Borges Chinea, P. Esparza Ferrera, J. Canales-Vázquez, P. Núñez, J. C. Ruiz-Morales, Prospective use of the 3D printing technology for the microstructural engineering of Solid Oxide Fuel Cell components. *Boletín la Soc. Española Cerámica y Vidr.* **53**, 213–216 (2014).
60. S.-J. Ahn, Y.-B. Kim, J. Moon, J.-H. Lee, J. Kim, Co-planar type single chamber solid oxide fuel cell with micro-patterned electrodes. *J. Electroceramics*. **17**, 689–693 (2006).
61. Y.-B. Kim, S.-J. Ahn, J. Moon, J. Kim, H.-W. Lee, Direct-write fabrication of integrated planar solid oxide fuel cells. *J. Electroceramics*. **17**, 683–687 (2006).
62. M. Kuhn, T. Napporn, M. Meunier, D. Therriault, S. Vengallatore, Fabrication and testing of coplanar single-chamber micro solid oxide fuel cells with geometrically complex electrodes. *J. Power Sources*. **177**, 148–153 (2008).
63. M. Kuhn, T. W. Napporn, M. Meunier, D. Therriault, Single-chamber micro solid oxide fuel cells: Study of anode and cathode materials in coplanar electrode design. *Solid State Ionics*. **181**, 332–337 (2010).
64. B.-J. de Gans, P. C. Duineveld, U. S. Schubert, Inkjet printing of polymers: state of the art and future developments. *Adv. Mater.* **16**, 203–213 (2004).
65. G. M. Gratson, M. Xu, J. A. Lewis, Microperiodic structures: Direct writing of three-dimensional webs. *Nature*. **428**, 386–386 (2004).
66. J. A. Lewis, G. M. Gratson, Direct writing in three dimensions. *Mater. Today*. **7**, 32–39 (2004).
67. E. N. Udofia, W. Zhou, A guiding framework for microextrusion additive manufacturing. *J. Manuf. Sci. Eng.* **141**, 050801 (2019).
68. C. A. Schneider, W. S. Rasband, K. W. Eliceiri, Historical commentary NIH Image to ImageJ : 25 years of image analysis. *Nat. Methods*. **9**, 671–675 (2012).
69. W. H. Herschel, R. Bulkley, Konsistenzmessungen von Gummi-Benzollösungen. *Kolloid-Zeitschrift*. **39**, 291–300 (1926).

70. H. Nakajima, T. Kitahara, T. Konomi, Electrochemical impedance spectroscopy analysis of an anode-supported microtubular solid oxide fuel cell. *J. Electrochem. Soc.* **157**, B1686–B1692 (2010).

71. G. Cai, Y. Gu, L. Ge, Y. Zhang, H. Chen, L. Guo, Modification of electrolyte surface with "windows" and "dimples array" structure for SOFC based on YSZ electrolyte. *Ceram. Int.* **43**, 8944–8950 (2017).

72. W. Ostwald, Ueber die rechnerische darstellung des strukturgebietes der viskosität. *Kolloid-Zeitschrift*. **47**, 176–187 (1929).

73. H. Iwai, N. Shikazono, T. Matsui, H. Teshima, M. Kishimoto, R. Kishida, D. Hayashi, K. Matsuzaki, D. Kanno, M. Saito, H. Muroyama, K. Eguchi, N. Kasagi, H. Yoshida, Quantification of SOFC anode microstructure based on dual beam FIB-SEM technique. *J. Power Sources*. **195**, 955–961 (2010).

74. M. Kishimoto, H. Iwai, M. Saito, H. Yoshida, Quantitative evaluation of solid oxide fuel cell porous anode microstructure based on focused ion beam and scanning electron microscope technique and prediction of anode overpotentials. *J. Power Sources*. **196**, 4555–4563 (2011).

75. M. Kishimoto, H. Iwai, M. Saito, H. Yoshida, Three-dimensional simulation of SOFC anode polarization characteristics based on sub-grid scale modeling of microstructure. *J. Electrochem. Soc*. **159**, B315–B323 (2012).

76. K. Miyoshi, T. Miyamae, H. Iwai, M. Saito, M. Kishimoto, H. Yoshida, Exchange current model for $(La_{0.8}Sr_{0.2})_{0.95}MnO_3$ (LSM) porous cathode for solid oxide fuel cells. *J. Power Sources*. **315**, 63–69 (2016).

77. B. Steele, Appraisal of $Ce_{1-y}Gd_yO_{2-y/2}$ electrolytes for IT-SOFC operation at 500°C. *Solid State Ionics*. **129**, 95–110 (2000).

78. M. Kishimoto, S. Kishida, H. Seo, H. Iwai, H. Yoshida, Prediction of electrochemical characteristics of practical-size solid oxide fuel cells based on database of unit cell performance. *Appl. Energy*. **283**, 116305 (2020).

79. R. B. Evans, G. M. Watson, E. A. Mason, Gaseous diffusion in porous media at uniform pressure. *J. Chem. Phys.* **35**, 2076–2083 (1961).

80. R. B. Evans, G. M. Watson, E. A. Mason, Gaseous diffusion in porous media. II. Effect of pressure gradients. *J. Chem. Phys.* **36**, 1894–1902 (1962).

81. D. Arnošt, P. Schneider, Dynamic transport of multicomponent mixtures of gases in porous solids. *Chem. Eng. J. Biochem. Eng. J.* **57**, 91–99 (1995).

82. M. García-Camprubí, N. Fueyo, Mass transfer in hydrogen-fed anode-supported SOFCs. *Int. J. Hydrogen Energy*. **35**, 11551–11560 (2010).

83. H. J. M. Bouwmeester, M. W. Den Otter, B. A. Boukamp, Oxygen transport in $La_{0.6}Sr_{0.4}Co_{1-y}Fe_yO_{3-\delta}$. *J. Solid State Electrochem.* **8**, 599–605 (2004).

84. K. Matsuzaki, N. Shikazono, N. Kasagi, Three-dimensional numerical analysis of mixed ionic and electronic conducting cathode reconstructed by focused ion beam scanning electron microscope. *J. Power Sources*. **196**, 3073–3082 (2011).

85. U. Anselmi-Tamburini, G. Chiodelli, M. Arimondi, F. Maglia, G. Spinolo, Z. . Munir, Electrical properties of Ni/YSZ cermets obtained through combustion synthesis. *Solid State Ionics*. **110**, 35–43 (1998).

86. N. F. Bessette, W. J. Wepfer, J. Winnick, A mathematical model of a solid oxide fuel cell. *J. Electrochem. Soc.* **142**, 3792–3800 (1995).

87. E. N. Fuller, P. D. Schettler, J. C. Giddings, New method for prediction of binary gas-phase diffusion coefficients. *Ind. Eng. Chem.* **58**, 18–27 (1966).

88. K. Yashiro, I. Nakano, M. Kuhn, S. Hashimoto, K. Sato, J. Mizusaki, Electrical conductivity and oxygen diffusivity of perovskite-type solid solution $La_{0.6}Sr_{0.4}Co_{1-y}Fe_yO_{3-\delta}$ (y=0.2, 0.4, 0.5, 0.6, 0.8). *ECS Trans.* **35**, 1899–1907 (2011).

89. T. Kawada, N. Sakai, H. Yokokawa, M. Dokiya, M. Mori, T. Iwata, Characteristics of slurry-coated nickel zirconia cermet anodes for solid oxide fuel cells. *J. Electrochem. Soc.* **137**, 3042–3047 (1990).

90. D. Kanno, N. Shikazono, N. Takagi, K. Matsuzaki, N. Kasagi, Evaluation of SOFC anode polarization simulation using three-dimensional microstructures reconstructed by FIB tomography. *Electrochim. Acta*. **56**, 4015–4021 (2011).

91. A. Esquirol, N. P. Brandon, J. A. Kilner, M. Mogensen, Electrochemical characterization of $La_{0.6}Sr_{0.4}Co_{0.2}Fe_{0.8}O_3$ cathodes for intermediate-temperature SOFCs. *J. Electrochem. Soc.* **151**, A1847–A1855 (2004).

92. K. Miyoshi, H. Iwai, M. Kishimoto, M. Saito, H. Yoshida, Chromium poisoning in $(La,Sr)MnO_3$ cathode: Three-dimensional simulation of a solid oxide fuel cell. *J. Power Sources*. **326**, 331–340 (2016).

93. K. Miyawaki, M. Kishimoto, H. Iwai, M. Saito, H. Yoshida, Comprehensive understanding of the active thickness in solid oxide fuel cell anodes using experimental, numerical and semi-analytical approach. *J. Power Sources*. **267**, 503–514 (2014).

94. Y. T. Kim, Z. Jiao, N. Shikazono, Evaluation of $La_{0.6}Sr_{0.4}Co_{0.2}Fe_{0.8}O_3$-$Gd_{0.1}Ce_{0.9}O_{1.95}$ composite cathode with three dimensional microstructure reconstruction. *J. Power Sources*. **342**, 787–795 (2017).

95. J. W. Veldsink, R. M. J. van Damme, G. F. Versteeg, W. P. M. van Swaaij, The use of the dusty-gas model for the description of mass transport with chemical reaction in porous media. *Chem. Eng. J. Biochem. Eng. J.* **57**, 115–125 (1995).

96. S. B. Adler, J. A. Lane, B. C. H. Steele, Electrode kinetics of porous mixed-conducting oxygen electrodes. *J. Electrochem. Soc.* **143**, 3554–3564 (1996).

97. R. Krishna, J. A. Wesselingh, The Maxwell-Stefan approach to mass transfer. *Chem. Eng. Sci.* **52**, 861–911 (1997).

98. R. Suwanwarangkul, E. Croiset, M. W. Fowler, P. L. Douglas, E. Entchev, M. A. Douglas, Performance comparison of Fick's, dusty-gas and Stefan–Maxwell models to predict the concentration overpotential of a SOFC anode. *J. Power Sources*. **122**, 9–18 (2003).

99. K. Tseronis, I. K. Kookos, C. Theodoropoulos, Modelling mass transport in solid oxide fuel cell

anodes: a case for a multidimensional dusty gas-based model. *Chem. Eng. Sci.* **63**, 5626–5638 (2008).

100. K. Chen, Z. Lü, N. Ai, X. Huang, Y. Zhang, X. Xin, R. Zhu, W. Su, Development of yttria-stabilized zirconia thin films via slurry spin coating for intermediate-to-low temperature solid oxide fuel cells. *J. Power Sources*. **160**, 436–438 (2006).

101. H. J. Kim, M. Kim, K. C. Neoh, G. D. Han, K. Bae, J. M. Shin, G.-T. Kim, J. H. Shim, Slurry spin coating of thin film yttria stabilized zirconia/gadolinia doped ceria bi-layer electrolytes for solid oxide fuel cells. *J. Power Sources*. **327**, 401–407 (2016).

102. J. Weese, A reliable and fast method for the solution of Fredholm integral equations of the first kind based on Tikhonov regularization. *Comput. Phys. Commun.* **69**, 99–111 (1992).

103. R. de L. Kronig, On the theory of dispersion of X-rays. *J. Opt. Soc. Am.* **12**, 547 (1926).

104. A. N. Tikhonov, Solution of incorrectly formulated problems and the regularization method. *Sov. Math. Dokl.* **4**, 1035–1038 (1963).

105. S. Dierickx, J. Joos, A. Weber, E. Ivers-Tiffée, Advanced impedance modelling of Ni/8YSZ cermet anodes. *Electrochim. Acta*. **265**, 736–750 (2018).

106. Y. Lin, S. B. Beale, Performance predictions in solid oxide fuel cells. *Appl. Math. Model.* **30**, 1485–1496 (2006).

107. B. Shri Prakash, S. Senthil Kumar, S. T. Aruna, Properties and development of Ni/YSZ as an anode material in solid oxide fuel cell: A review. *Renew. Sustain. Energy Rev.* **36**, 149–179 (2014).

108. A. Leonide, Y. Apel, E. Ivers-Tiffee, SOFC modeling and parameter identification by means of impedance spectroscopy. *ECS Trans.* **19**, 81–109 (2009).

109. H. Sumi, T. Yamaguchi, K. Hamamoto, T. Suzuki, Y. Fujishiro, High performance of $La_{0.6}Sr_{0.4}Co_{0.2}Fe_{0.8}O_3$–$Ce_{0.9}Gd_{0.1}O_{1.95}$ nanoparticulate cathode for intermediate temperature microtubular solid oxide fuel cells. *J. Power Sources*. **226**, 354–358 (2013).

110. B. A. Boukamp, H. J. Bouwmeester, Interpretation of the Gerischer impedance in solid state

ionics. *Solid State Ionics*. **157**, 29–33 (2003).

111. Y. Lu, C. Kreller, S. B. Adler, Measurement and modeling of the impedance characteristics of porous $La_{1-x}Sr_xCoO_{3-\delta}$ electrodes. *J. Electrochem. Soc.* **156**, B513–B525 (2009).

112. V. Brichzin, The geometry dependence of the polarization resistance of Sr-doped $LaMnO_3$ microelectrodes on yttria-stabilized zirconia. *Solid State Ionics*. **152**–**153**, 499–507 (2002).

113. C. S. Ogilvy, *Excursions in Geometry* (Dover Publications, 1990).

114. J. L. W. V Jensen, Sur les fonctions convexes et les inégalités entre les valeurs moyennes. *Acta Math.* **30**, 175–193 (1906).